Characterization and Modeling of Magnetoelectric Micro Sensors

Thi Ngoc Nguyen

université PARIS-SACLAY

NNT=2018SACLS203

Thèse de doctorat

UNIVERSITÉ PARIS SUD
Comprendre le monde, construire l'avenir

Caractérisation et modélisation d'un micro-capteur magnétoélectrique

Thèse de doctorat de l'Université Paris-Saclay
Préparée à l'Université Paris-Sud

École doctorale n°575: electrical, optical, bio: physics and engineering (EOBE)
Spécialité de doctorat: Électronique et Optoélectronique, Nano- et Microtechnologies

Thèse présentée et soutenue à Orsay, le 6 Juillet 2018, par

Mme Thi-Ngoc NGUYEN

Composition du Jury :

Mr Jean-Christophe LACROIX Professeur, Université Paris Diderot Laboratoire ITODYS – UMR 7086	Président
Mme Silvana MERCONE Maître de Conférences, Université Paris 13 Laboratoire LSPM – UPR 3407	Rapporteur
Mr Houssny BOUYANFIF Université de Picardie Jules Verne Laboratoire LPMC – EA 2081	Rapporteur
Mr Laurent DANIEL Professeur, CentraleSupelec, Laboratoire GeePs – UMR 8507	Examinateur
Mr Philippe LECOEUR Professeur, Université Paris-Sud Laboratoire C2N –Orsay – UMR 9001	Directeur de thèse
Mr Guillaume AGNUS Maître de Conférences, Université Paris-Sud Laboratoire C2N –Orsay – UMR 9001	Co-Directeur de thèse

ACKNOWLEDGEMENTS

I would like to express my gratitude to the following organizations and individuals who supported, assisted and encouraged me during this thesis.

I am foremost grateful for the financial support from project 911 of the Ministry of Education and Training (MOET) for training high-qualified lecturers at the University of Science and Technology of Hanoi (USTH).

I would like to thank my supervisor Prof. Philippe Lecoeur and my co-director Dr. Guillaume Agnus for giving me an opportunity to join the OXIDE group to work on an interesting and challenging project, as well as their encouragement and scientific guidance throughout my presented PhD program.

I would like to thank Houssny Bouyanfif and Silvana Mercone for being excellent reviewers, thoroughly evaluating my work and providing helpful comments and questions. I would also like to thank the members of the jury, Prof. Jean-Christophe Lacroix and Prof. Laurent Daniel for their helpful suggestions and constructive comments.

I also would like to express my deep gratitude to my colleagues who supported me in all scientific and technical matters. This thesis would not have been possible without their support. I would like to give my special thanks to Thomas Maroutian for all his great support concerning PLD, AFM, XRD. I would like to thank Sylvia Matzen for her support on device fabrication and helpful discussions. I would also like to thank Pascal Aubert for his expertise in simulation.

Before starting my PhD training at the University of Paris-Sud, I studied and worked as a temporary researcher at VNU-Key Laboratory for Micro-Nano Technology: Development and Application of Micro-Nanotechnology Fabrication of Materials and Devices. I would like to thank Prof. Duc NH and Assc. Prof. Giang DTH, who were my supervisors during the time at VNU as an MSc student, for their continuous support and encouragement, and for their continued guidance in finishing part of my work at VNU. My gratitude also goes to MSc. Le Khac Quynh for the numerous deposits of magnetostrictive thin films by sputtering.

I would like to thank all colleagues at C2N for the great atmosphere and for being a part of my life: Laurie Calvet, Valérie Pillard, Amina Aidoud, Etienne Thiebaut, Loïc Guillemot, Benjamin Leroy, Aurore Ecarnot, Abdelnour Benamar, Amal Hamdache, Guillaume Marcaud,

Van Son Nguyen, Martine Zahradnik, Florian Pallier, Giovanni Magno, Navy Yam, and Robert Mégy.

I would also like to thank all Vietnamese friends for their warm friendship and care during the years: Thuy, Trang, Ngoc's family, Hoai (Son), Loan, Hoai Ngo, Thinh, Duong Anh's family, Thien, Huyen, Ha, Phuong, Duong Ngo, Mai Chung, and Cam Hoang.

Last but not least, I would like to especially thank my family, my husband, my parents and my sister for their love and support in care of my son. With all my heart, thank you to my son, Minh-Duc, for coming into my life and being my happiness.

TABLE OF CONTENTS

Introduction

Detection of magnetic fields plays a central role in many areas as diverse as scientific instrumentation, biology, geoscience, everyday technologies to name some of the most important. The range of sensitivity is directly related to the area of application, and in the specific case of magnetic field sensing, it can range from Tesla for field measurement between the air gap of an electromagnet down to femtotesla for detection of biological signals. It thus covers up to fifteen orders of magnitude and for this reason, different physical systems have emerged over the decades to cover this broad scale.

All approaches are usually based on the intimate correlation between electrical and magnetic phenomena. The use of different properties has led to different technologies such as Hall effect sensors, for the most common, to SQUIDs for the most sensitive ones requiring cooling with liquid helium and allowing the detection of brain activity in the femtotesla range [1]. Between these two extremes, there are sensors whose reading is done by simple resistance measurement, in the case of sensors derived from spin electronics or by resonance measurement as is the case with magnetoelectric sensors. This last type of sensors based on the magnetoelectric effect (ME) does not require cooling and the signal measurement is done without current injection. They have progressed rapidly and can cover a wide range in sensitivity from millitesla to few tens of picotesla [2], [3]. Their operation is based on magnetoelectric coupling mediated by stress transfer between a magnetostrictive material and a piezoelectric material. A change in the magnitude of the magnetic field or its direction induces a mechanical deformation in the magnetostrictive layer that leads to a stress that is transferred into the piezoelectric material. The later, under the effect of the stress, develops a voltage by direct piezoelectric effect. This device is passive and does not require any external power supply. To date the developments of this type of sensor are mainly focused on the use of millimetric piezoelectric ceramics assembled with magnetostrictive layers deposited in thin films, which offers a high output signal and does not require significant means of fabrication [4]–[6]. In order to make this type of device competitive, it is important to be able to miniaturize them on the basis of microelectronics technologies that, in addition to reducing size, open up for integrable sensors

[6]–[8]. One of the prime issues is to grow on silicon substrate the full heterostructure leading to the mutiferroic stack. For this reason, the growth of the full stack in thin films form, integrated on silicon, has attracted attention in recent years due to the development of epitaxial thin-film deposition techniques [9][10]. For applications based on ME materials, particularly, the $Pb(Zr_xTi_{1-x})O_3$ (PZT) with a Zr/Ti ratio of 52/48 has received a more specific attention as its piezoelectric response relates to the existence of competition between rhombohedral and tetragonal phases leading to one of the highest piezoelectric response, around -170 pm/V and 374 pm/V for the piezoelectric coefficient d_{31} and d_{33}, respectively [11][12]. In term of quality, many reports have pointed out the interest for epitaxial films. Many reports have shown the interest of using epitaxial PZT films in comparison with polycrystalline one. For the magnetostrictive material, the TbFeCo as retained a particular attention as a suitable candidate for the magnetostrictive layer thanks to its high magnetostriction constant.

The main focus of this thesis work is to develop the growth of high response magnetoelectric stack on silicon and, using standard microfabrication techniques, to fabricate magnetoelectric cantilevers that will be a first building block for magnetic field sensing using resonant systems. Another major challenge that needs to be addressed when minimizing sensor configuration down to micro-scale is reduction in magnitude of the output signal. Therefore, the objective of this thesis is to explore the ability to use this kind of sensor as a resonant micro-sensor taking advantage of magneto-electric coupling for sensing the magnetic signal. The expected result is the shift of the resonant frequency with respect to a magnetic field change, instead of an output voltage change responding to an external magnetic field. By using micro-fabrication, the better surface quality and the disappearance of the bonding layer between two phases of materials existing in the bulk sensors are expected to enhance the coupling interactions between two phases of materials, thereby helping to overcome the size constraint.

The document is organized as follows. The first chapter introduces the piezoelectric materials and the magnetostrictive materials to explain the magnetoelectric effect. On this basis, current state of the art of magnetoelectric devices for magnetic field sensing is exposed and discussed. Experimental techniques are exposed in Chap. 2. Growth method of piezoelectric (PZT) and magnetostrictive thin films on Si substrates are described as well as the several structural characterization methods used to investigate the structures of the as-deposited samples. The detailed description of the principle of several typical measurements to

determine ferroelectric properties, magnetic properties, and magneto-electric properties is given second section of the chapter. Chap. 3 is devoted to the results on the growth of epitaxial $Pb(Zi_{0.52}Ti_{0.48})O_3$ on (001)-Si through oxide transition layers. In particular the control of the epitaxial orientation of PZT layers depending on the nature of the bottom electrodes is presented. Properties of grown films, including structural properties, polarization, and dielectric constant are given and main parameters extracted targeting the device fabrication. Growth conditions, magnetic and magnetostriction characteristics of magnetostrictive material TbFeCo are also presented. The last chapter is dedicated to the behavior of the PZT cantilevers aiming to study its resonant response for sensing magnetic field based on the ME effect. First part of the chapter focuses on the micro-fabrication processes and investigation of the developed device is discussed. Then, the static response of the device is used to extract some physical information about the films such as piezoelectric coefficient. The dynamic behavior of the cantilever is then studied. First, the measurement methods developed that allow characterizing the frequency response of the PZT micro-cantilever as a function of several parameters such as structural (width, length, contact material thickness…), then the measurement condition (pressure, DC bias…) are detailed. A rough calculation of the ability of such magnetostrictive materials integrated with PZT thin films for magnetic sensing applications will be shown. Finally, we present results on very first attempt of a resonator for sensing magnetic signal based on PZT/TbFeCo multiferroics thin films. TbFeCo is used as a micro-actuator, while the PZT thin film is used as a micro-sensor. A resonant frequency shift of the device reflects the magnitude of the external magnetic field is obtained and analyzed.

References

[1] J. Clarke and A. I. Braginski, *The SQUID Handbook*, vol. 1. 2005.

[2] M. Li, A. Matyushov, C. Dong, H. Chen, H. Lin, T. Nan, Z. Qian, M. Rinaldi, Y. Lin, and N. X. Sun, "Ultra-sensitive NEMS magnetoelectric sensor for picotesla DC magnetic field detection," *Appl. Phys. Lett.*, vol. 110, p. 143510, 2017.

[3] S. Dong, J. F. Li, and D. Viehland, "Ultrahigh magnetic field sensitivity in laminates of TERFENOL-D and Pb(Mg1/3Nb2/3)O3-PbTiO3 crystals," *Appl. Phys. Lett.*, vol. 83, no. 11, pp. 2265–2267, 2003.

[4] N. H. Duc, B. D. Tu, N. T. Ngoc, V. D. Lap, and D. T. H. Giang, "Metglas/PZT-magnetoelectric 2-D geomagnetic device for computing precise angular position," *IEEE Trans. Magn.*, vol. 49, no. 8, pp. 4839–4842, 2013.

[5] S. M. Gillette, A. L. Geiler, D. Gray, D. Viehland, C. Vittoria, and V. G. Harris, "Improved sensitivity and noise in magneto-electric magnetic field sensors by use of modulated AC magnetostriction," *IEEE Magn. Lett.*, vol. 2, p. 2500104, 2011.

[6] M. Li, Y. Wang, J. Gao, J. Li, and D. Viehland, "Enhanced magnetoelectric effect in self-stressed multi-push-pull mode Metglas/Pb(Zr,Ti)O3/Metglas laminates," *Appl. Phys. Lett.*, vol. 101, p. 022908, 2012.

[7] N. M. Aimon, D. Hun Kim, H. Kyoon Choi, and C. a. Ross, "Deposition of epitaxial BiFeO3/CoFe2O4 nanocomposites on (001) SrTiO3 by combinatorial pulsed laser deposition," *Appl. Phys. Lett.*, vol. 100, p. 092901, 2012.

[8] Y. Wang, J. Atulasimha, and R. Prasoon, "Nonlinear magnetoelectric behavior of Terfenol-D/PZT-5A laminate composites," *Smart Mater. Struct.*, vol. 19, p. 125005, 2010.

[9] M. Dekkers, H. Boschker, M. van Zalk, M. Nguyen, H. Nazeer, E. Houwman, and G. Rijnders, "The significance of the piezoelectric coefficient d 31,eff determined from cantilever structures," *J. Micromechanics Microengineering*, vol. 23, p. 025008, 2013.

[10] Q. Guo, G. Z. Cao, and I. Y. Shen, "Measurements of Piezoelectric Coefficient d 33 of Lead Zirconate Titanate Thin Films Using a Mini Force Hammer," *J. Vib. Acoust.*, vol. 135, p. 011003, 2013.

[11] M. D. Nguyen, M. Dekkers, E. P. Houwman, H. T. Vu, H. N. Vu, and G. Rijnders, "Pulsed laser deposition driving MEMS-based piezoelectric cantilevers," *Mater. Lett.*, vol. 164, pp. 413–416, 2016.

[12] M. D. Nguyen, "Characterization of epitaxial Pb(Zr,Ti)O3 thin films deposited by pulsed laser deposition on silicon cantilevers," *J. Micromech.Microeng*, vol. 20, p. 085022, 2010.

Chapter I– Micro-sensors based on magneto-electric effect

This chapter briefly discusses the context of the magneto-electric effect, focusing on the phenomena relevant to this work. In particular, piezoelectricity and magnetostriction are discussed through important parameters related to the choice of selected materials. The chapter then discusses state of the art magneto-electric sensors and concludes with the challenge of integration in the form of microsystems on silicon for sensing applications.

Outline:

I.1 Magnetic flux and field sensors

There are many approaches to detect magnetic signals, most of them are based on the intimate correlation between electrical and magnetic phenomena. Depending on whether the sensor detects the magnetic flux variation or the magnetic field, different types of technologies can be used. This work focuses on the development of field sensor based on magnetoelectric effect. To compare the different types of field sensors, one can look at the sensitivity range specific to each sensor as summarized in Figure I-1. Hall sensors are the most popular but in order to gain in sensitivity, magnetoresistors based on Anisotropic Magneto Resistance (AMR) [1], [2], Giant Magneto Resistance (GMR) [3], [4] and Tunnel Magneto Resistance (TMR) [5] have given more attention in the last three decades. In the meantime, recent advances in ferromagnetic thin films deposition techniques have allowed fabrication of magnetoelectric sensors with an advantage of being fully passive devices as a measurable voltage is directly created under the application of an external magnetic field [6].

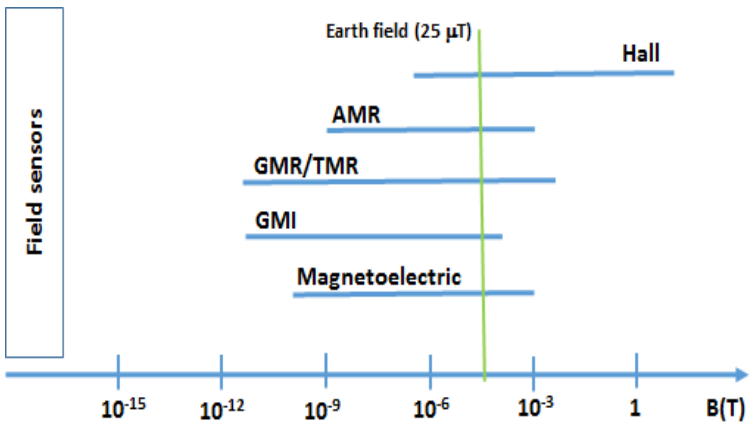

Figure I-1: Typical field range of various magnetic flux and field sensors (adapted from[7])

In addition to increased sensitivity, the limit of detection has to be considered depending on the targeted applications, the environment, and specific shielding required for low limit of detection [8].

I.2 Magneto-electric effect

Brief historical and current state overview

In recent decades, ferroelectric (FE) and ferromagnetic (FM) materials have been extensively studied and their shaping into thin films has opened up large number of applicative developments. While ferroelectricity results from the relative change in the position of the centroid of charges at the unit cell scale, magnetism is related to the order of the spin of electrons in incomplete ion envelopes, in other words, partly filled orbitals in transition metals or orbital f partially filled with rare earth metals. Due to high dielectric constant and the existence of two stable states of opposite polarization, ferroelectric materials are good candidates for high k capacitors and for memory applications. Similarly, applications using ferromagnetic materials such as sensors, read heads, memories are already available on the market. More recently the coupling of these two properties has been studied enlarging the applicative field of these two materials.

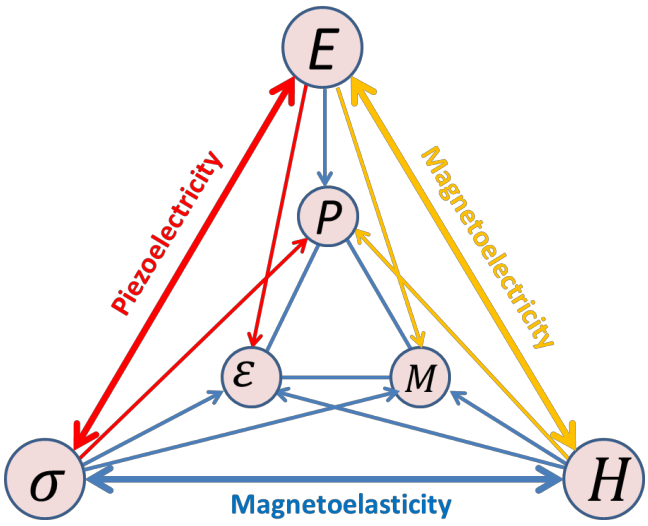

Figure I-2: Magnetoelectric effect described with the interplay between piezoelectric and ferromagnetic properties

This novel class of multifunctional materials called Magneto-electric (ME) materials, obtained by combining ferroelectric and ferromagnetic properties, has recently received a strong interest. [9], [10] Such materials exhibit ME effect in which an electric polarization ***P***

can be tuned by an external magnetic field $\boldsymbol{H}$ or, at the opposite, the magnitude of magnetization $\boldsymbol{M}$ in a material is induced upon applying an electric field $\boldsymbol{E}$ (see Figure I-2), both properties arising from the cross coupling between FE and ME ordering.

This ME effect is obtained in multi-ferroic materials, a novel class of multifunctional materials, which can be divided into several categories such as single phase showing intrinsic coupling effect, laminated composite, and micro-nano structured thin films exhibiting extrinsic effects. Back in 1888, W. Rontgen showed that a dielectric material moving through an electric field would be magnetized as the first example of a ME effect [11]. Six years later, P. Curie predicted theoretically the possibility of an intrinsic ME effect in a material, while the term "magnetoelectric" was coined by P. Debye in 1926. More than thirty years elapsed before the first experimental proof and, in 1960, G. N. Astrov published such observation in a single crystal of Cr_2O_3 [12]. Since, few more single-phase ME materials have been found. Most of single phase multiferroics, however, have Neel and/or Curie temperatures well below room temperature, and exhibit quite low values of magnetoelectric coupling constant limiting the range of practical application. As an example, the best single-phase materials Cr_2O_3 exhibits a ME voltage coefficient of about 20 mV/cm.Oe with a Néel temperature of 308K.

In recent years, bismuth ferrite $BiFeO_3$ (BFO) was identified as the single-phase multiferroic [13] with a large polarization at room-temperature. In 2006, Wang et al. reported a high value of ferroelectric polarization of $55\,\mu C/cm^2$on a multilayer stack of $BiFO_3/La_{0.7}Sr_{0.3}MnO_3/SrTiO_3/Si$ deposited by pulsed laser deposition. However, such structures tend to have high leakage current leading to a tendency for fatigue and possible thermal decomposition near the coercive field limiting the use of BFO for device applications.

Some of these obstacles of the single phase material have been overreached by forming multi-phase ME composites or laminates of ferromagnetic/piezoelectric that are featured by the higher ME coefficient and functioning at room temperature [10], [14], [15]. The value of ME coefficient up to 70V/cm.Oe at resonance was reported on Terfenol-D/PZT bimorph ME laminate by Zhai et al. [16]. Recently, the advances in thin-film growth techniques have opened a promising approach to the design of devices based on ME coupling. A few research activities in multiferroic magneto-electric thin films has emerged and flourished [17]–[20]. Most of them were motivated by promising applications in information storage technology and spintronic based on magnetic tunneling junctions (MTJs) structures. The mechanism of this approach is

to control magnetic anisotropy and magnetization by the application of an electric field. For this purpose, the in-plane piezo-strain is the key technique, which make the [011]-oriented PMN-PT ($d_{31} = -3000\, pC/N[100]$and $d_{32} = 1000\, pC/N[01\bar{1}][21]$) a popular choice for proof of concept demonstrations.

Basic relationship of extrinsic magnetoelectric effect

The extrinsic magnetoelectric effect is strain-mediated mechanism. Figure I-3 sketch the observed mechanisms in the case of direct effect or inverse one. The direct magnetoelectric effect corresponds to the change of electrical polarization under the application of an external magnetic field. The change of magnetization induces by magnetostriction a change of the mechanical state at the interface with the piezoelectric layer and hence by direct piezoelectric effect induces a change of the ferroelectric polarization leading to a voltage across the ferroelectric layer.

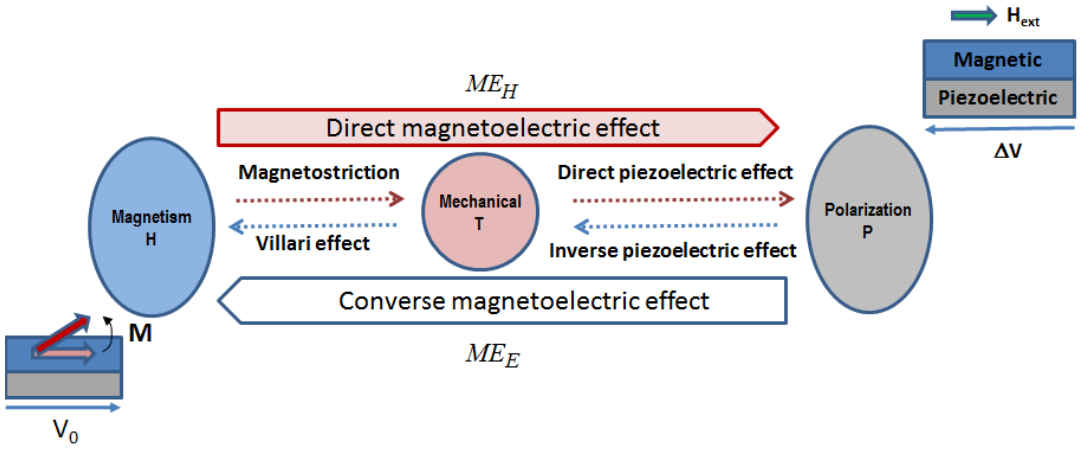

Figure I-3: Sketch of the involved mechanisms in the extrinsic magnetoelectric coupling.

At the opposite, the converse effect corresponds to a strain generation at the interface by applying a voltage to the piezoelectric layer inducing by Villari effect a change of the magnetization state in the ferromagnetic layer. Both ME effects can be linked with the following expression for the direct and the converse effects, respectively:

- for direct effect: $$ME_H = \frac{magnetic}{mechanical} \times \frac{mechanical}{electric}$$ **Eq (I-1)**
- for converse effect: $$ME_E = \frac{electric}{mechanical} \times \frac{mechanical}{magnetic}$$

From above expressions, the ME effect can be enhanced by:

(i) Optimizing each material, targeting the highest magnetostriction for the ferromagnetic layer and the highest piezoelectric response for the second layer.

(ii) Improving the coupling interaction between different layers. In this thesis, the compound $Pb(Zr_xTi_{1-x})O_3$ (PZT) with a Zr/Ti ratio of 52/48 has been chosen as the piezoelectric phase for its high electromechanical coupling factor due to the existence competition of both rhombohedral and tetragonal phases. The selected magnetostrictive layer is the TbFeCo compound.

(iii) Taking advantage of micro-fabrication, high thin film quality with sharp interface and the disappearance of a bonding layer between two phases of materials existing in the bulk sensors are expected to enhance the coupling interactions between two phases of materials, thereby helping to overcome the size constraint and improve the ME effect.

I.3 Piezoelectric material

I.3.1 Crystalline structure

The chosen piezoelectric material is Lead Zirconate Titanate (PZT). It is an intermetallic compound with the chemical formula: $Pb(Zr_xTi_{1-x})O_3$ $(0 \leq x \leq 1)$. This ternary compound is the most widely used ferroelectric obtained by mixing the tetragonal ferroelectric $PbTiO_3$ and the rhombohedral anti-ferroelectric $PbZrO_3$. The temperature phase diagram is given in Figure I-4 (left). All the compositions have an ABO_3 perovskite structure and are shown in Figure I-4 (right).

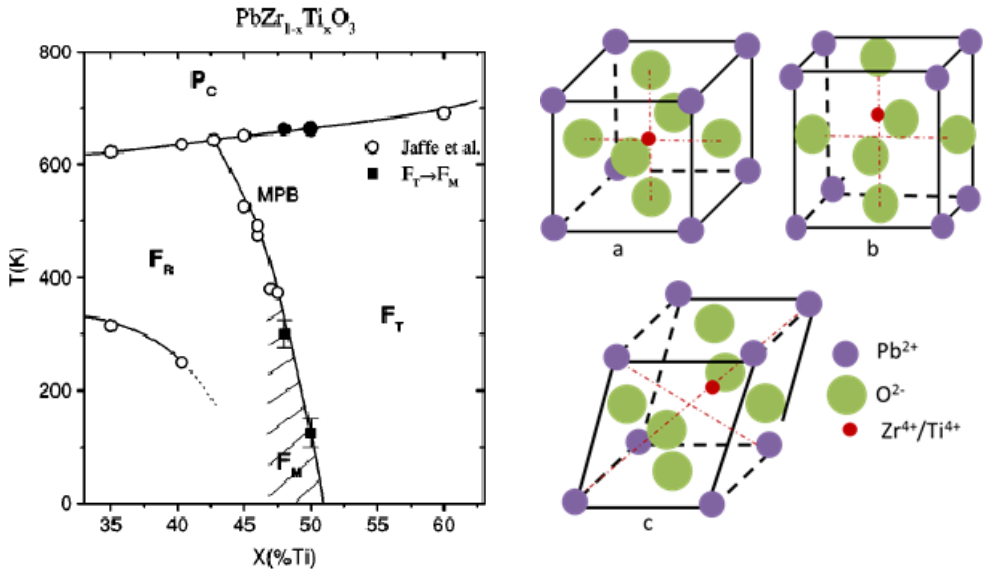

Figure I-4: (left) Phase diagram of the PZT. P_C: cubic paraelectric phase. F_R: rhombohedral phase ferroelectric. F_M: ferroelectric monoclinic phase. FT: quadratic ferroelectric phase. (right) (a) Ideal cubic perovskite structure. b) tetragonal structure and c) rhombohedral structure [22]

At high temperature, the PZT shows a cubic structure, because of this symmetry, this is a paraelectric material. The cation B (Zr or Ti) is having the degree of oxidation +4 and is located at the center of the cube. Oxygen atoms, with -2 degree of oxidation, are at the centers of faces and lead ions A, with degree of oxidation +2, are placed at the corners of the cube. As the temperature decreases, the PZT loses the center of the symmetry of the unit cell and becomes ferroelectric. According to Zr/Ti ratio, it takes rhombohedral structure R3m for Zr-rich compositions, and tetragonal structure P4mm for Ti-rich compositions as can be seen in Figure I-4 (left).

I.3.2 Ferroelectric properties

For device applications, the requirements are a high remnant polarization and a low coercive field to allow operation at low voltages. Ferroelectric materials are characterized by a non-zero spontaneous electrical polarization which can be tuned by the application of an external electric field. By convention, the polarization points downwards, towards the substrate for a thin layer, will be called positive polarization. If starting from a negative polarization state while gradually increasing the value of the external electric field, above a threshold value,

called a coercive field (E_c or V_c in tension), the polarization begins to align with the external field to reach a saturation value P_s as shown in Figure I-5. Then the positive polarization state is reached. When the external field is decreased, starting now from the state of positive polarization, the same mechanism occurs but for a negative coercive field. The existence of these two coercive fields is the signature of hysteresis. In addition, the polarization remains in its state when the electric field goes to zero, corresponding to the remnant polarization: P_r. More precise extraction of the remnant polarization can be obtained from the P-E curve as $P_r = [P_r^+ - P_r^-]/2$, where P_r^+ and P_r^- are the remnant polarizations of the positive and negative branches on the loop. Only an electrical field equal or greater than the coercive value allows returning the polarization.

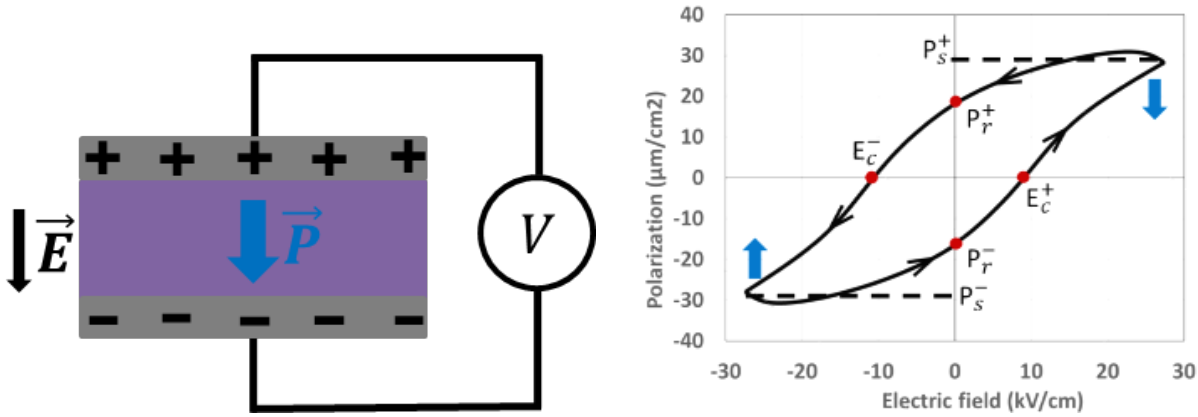

Figure I-5: A typical P-E hysteresis loop of a PZT film deposited on silicon. The blue arrows indicates the direction of the polarization.

Kinetics of the reversal process of the polarization in ferroelectric films: A few approaches have been proposed to understand polarization reversal mechanisms in ferroelectric films. In the case of single crystals, the approach based on domain wall motion kinetics has been widely accepted. It first involves the nucleation of the domains and their extension by the movement of the domain walls under the influence of the applied electric field. However, this is different for finite size ferroelectrics like in the case of thin films [17]. Another mechanism called the Nucleation-Limited Switching (NLS) has been proposed which describes the polarization reversal based on the statistics of nucleation in thin films as a function of time and voltage [18].

Dielectric properties:

The ferroelectric properties of PZT thin films can be tuned by controlling the film thickness, the crystallographic orientation or the composition by changing the Zr/Ti ratio [25], [26]. Reports show that the ferroelectric polarization decreases as well as the remnant polarization while increasing the Zr content in the compound. The c/a ratio can also be used to explain the relationship between ferroelectric properties and Zr/Ti ratio. For rich-Zr PZT, a decrease in c/a ratio (or residual stress) implies a smaller displacement of the central ion, which leads to a smaller remnant polarization. For the composition around x=0.48, the system is characterized by the coexistence of both tetragonal and rhombohedral phases leading to the so called Morphotropic Phase Boundary (MPB). In the vicinity of the MPB, the PZT show giant dielectric response and high electro-mechanical coupling constant at room temperature. Various studies [27]–[29] have shown that the high electromechanical response in this region is due continuous-phase transitions from tetragonal to rhombohedral through intermediate monoclinic phase.

I.3.3 Piezoelectricity

Piezoelectricity is the physical coupling between electrical and mechanical behaviors. This effect was discovered by Jacques and Pierre Curie in 1880 [30] in a number of crystals, such as tourmaline, quartz, topaz, cane sugar and Rochelle salt that exhibited surface charges when they were mechanically stressed. This phenomenon is also called the direct piezoelectric effect. The converse piezoelectric effect is discovered shortly after in 1881 by Lippmann [31], in which the electric field can deform the piezoelectric materials. In crystals, electromechanical coupling, characterized for piezoelectric properties, show the interplay between electrical quantities such as electric field or polarization and mechanical quantities such as strain or stress and are described by following equations expressing the converse and the direct piezoelectric effects:

$$\varepsilon_i = S_{ij}^{E}\sigma_j + d_{mi}E_m \qquad \textbf{Eq I-2}$$

$$D_m = d_{mi}\sigma_i + \xi_{ik}^{\sigma}E_k \qquad \textbf{Eq I-3}$$

With the quantities defined as:

$\varepsilon = \frac{\Delta l}{l}$: is the strain vector

$\sigma = \frac{F}{S}$: correspond to the Stress vector [N/m^2]

$E = \frac{V}{t}$: applied electric field [V/m]

d : matrix of piezoelectric strain constants [m/V]

g = $\frac{E}{\sigma}$: matrix of piezoelectric constants [C/m^2]

S: matrix of compliance coefficients [m/N^2]

D = $\frac{Q}{S}$: electric vector displacement [C/m^2]

ξ: electrical permittivity [C/m]

Due to a mechanical reaction in any direction when the material is subjected to an electric field in one specific direction, equations governing piezoelectricity are expressed by tensors. The indexes $i, j = 1, 2, 3, \dots, 6$ and $m, k = 1, 2, 3$ refer to different directions within the material coordinate system as shown in Figure I-6. By convention, axis 3 is assigned to the direction of the polarization of PZT. Axes 1 and 2 lies in the plane perpendicular to axis 3.

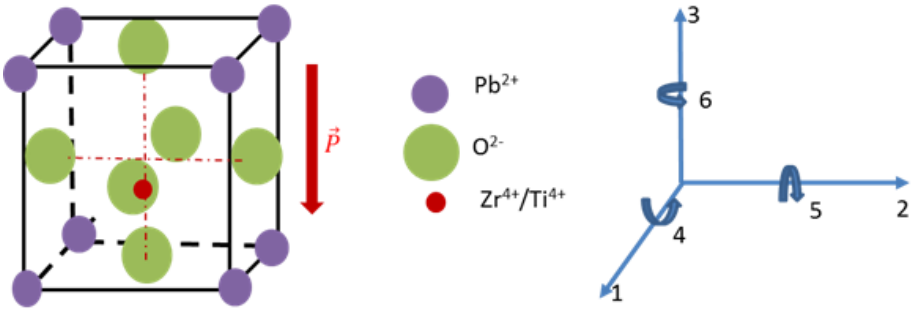

Figure I-6: The material and tensors coordinate system.

Two typical modes of piezoelectric MEMS structures have been used depending on the relative direction of the electric field E and thus the applied stress $\sigma_{xx(1)}$. As shown in Figure I-7, the induced electric field can be either parallel either perpendicular to the direction of applied stress: those modes are called d_{33} or d_{31}, respectively. Seon-Bae Kim et al., [32] made

a comparaison of MEMS PZT cantilevers based on d_{33} or d_{31} modes about the ability of the converted output power from vibration. The results show that higher output power in the d_{33} mode device than in the d_{31} mode device.

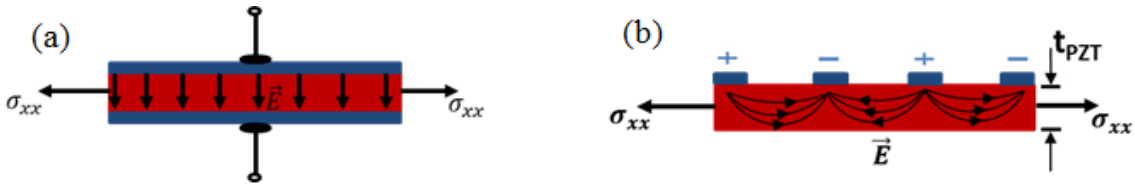

Figure I-7: Two typical modes of piezoelectric MEMS structures in cross section can be defined depending on the relative direction of the electric field *E* and the stress σ_{xx}: d_{31} mode (Figure a) and d_{33} mode (Figure b) [Adapted from 21]

This is explained due to the total electrode area patterned in PZT thin films smaller in the d_{33} mode device than the d_{31} mode device, which lead to the higher polarization value in PZT films of the d_{33} mode device. Usually, the design of the d_{33} mode gives lower leakage current because the electrodes are several parts, therefor this method is preferred for leakage materials. For practical issues with fabrication, however, a d_{31} mode device is often preferred due to its simple fabrication procedure.

I.4 Magnetostrictive effect and magnetostrictive materials

I.4.1 Magnetostrictive effect

Magnetostriction describes the change in dimensions of a ferromagnetic material when submitted to an external magnetic field. It was first discovered in 1842 by the English scientist J. P. Joule in a sample of iron. As illustrated in Figure I-8, a ferromagnetic material exhibits a change in magnetic susceptibility when submitted to mechanical stress, called the “Villari effect”. The reverse phenomenon is “Joule effect” and is illustrated in Figure I-8-b. It refers to the change in magnetic material size due to a change of its magnetization state. This is also known as the linear Joule magnetostriction and assumes that the volume of the material remains constant. Another type is the volume spontaneous magnetostriction associated with the change of the magnetic state by a temperature variation. Among them, the Joule magnetostriction

phenomenon has been much considered for applications such as sonars, active vibration control, acoustic devices, and position control.

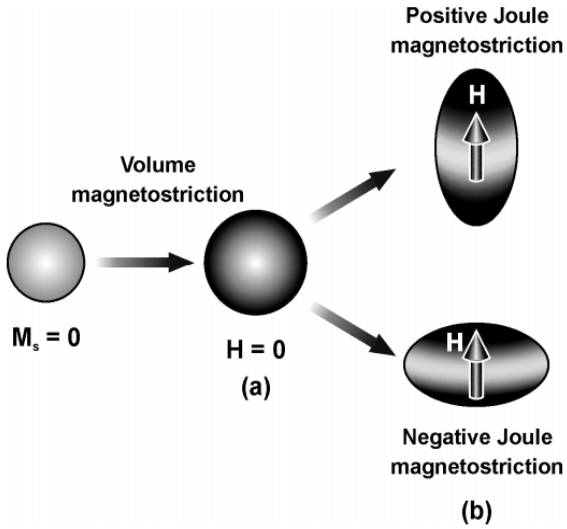

Figure I-8: Schematic of two principal effects:

volumic change (a) and Joule (b) magnetostriction of a spherical sample.

Joule effect is intrinsically related to the orientation of the magnetic moment under the effect of an external field and can be explained by the electrostatic interaction model between the electrons and nucleus. Under the influence of the external field, the distribution of the electron cloud (or orbital magnetic moments) will vary depending on how strongly it interacts with the spin magnetic moments. In the case of atoms with a spherical electron distribution, the electrostatic interaction is isotropic and thus the distance between the atoms remains the same while the orbital magnetic torque is changed under the applied external field. In this case, almost no magnetostrictive effect is observed. For atoms with the non-spherical electron distribution, the electrostatic interaction is anisotropic. Then, without external magnetic field, the electrostatic interaction between the electron orbitals with the crystal lattice or atomic environment or the Crystalline Electric-Field (CEF) interaction tend to orient the orbital moments and the spin moments along a well-defined direction through the spin-orbit coupling λLS. Two different cases can be observed:

- When the spin-orbit coupling is relatively weak (~0.015 eV per atom), the spin moments with the stronger exchange interactions (~ 0.1 eV) can easily be rotated under the applied field, but the orbital moments are almost fixed to the CEF

(Figure I-9 a), which contribute weekly to the magnetostriction. This case is for the 3d transition metals as Fe, Ni, Co.

- When the spin-orbit interactions is strong, the total moment J (i.e. both spin S and orbital L moments) can rotate in the applied magnetic fields. As a result, magnetic anisotropy and magnetostriction are large. This is in particular the case of the lanthanides and their alloys. As illustrated in Figure I-9, the magnetostriction is negative when the electron contribution is prolate shape ((Figure I-9 b), while the magnetostriction is positive when the electron density is oblate (Figure I-9 c).

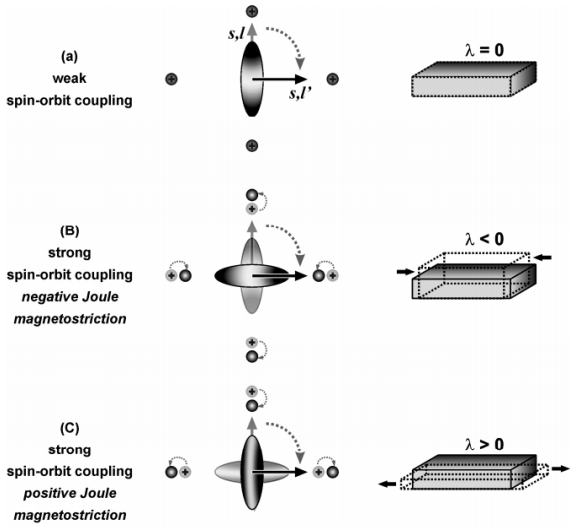

Figure I-9: Illustration of the effect of magnetostriction in the case of atoms with the non-spherical electron distribution [33]

In order to characterize the magnetostriction property, the definition of the magnetostriction coefficient is used and denoted by the dimensionless coefficient λ, which shows the relative length variation of the magnetized material $\lambda(H) = \frac{\Delta l(\mu_0 H)}{l} = \frac{l(\mu_0 H) - l_0}{l_0}$ corresponding to a relative deformation in one direction under an applied magnetic field. Here, l_0 is the initial length of the sample without an external magnetic field and $l(\mu_0 H)$ is the length of the sample under the external magnetic field. Additionally, the concept of magnetostrictive susceptibility (characteristic for the degree of magnetostriction of a material in response to an applied magnetic field) is defined as:

$$\chi_{\cdot}\lambda = \frac{\partial \lambda}{\partial H} \qquad \textbf{Eq I-4}$$

I.4.2 The intermetallic magnetostrictive materials

In order to fulfill requirements for practical applications, magnetostrictive materials need to exhibit in particular, large low-field magnetostrictive susceptibilities, low coercive fields and Curie temperature above room temperature. Magnetostrictive materials which have been considered in this thesis are the rare earth-transition metallic (R-T) compounds. Actually, the rare earth (or lanthanide) atoms exhibit an incomplete filling of the electronic shell localized strongly in the interior of the atom, leading to huge magnetic moment of 9 to 10 μ_B due to contribution of both orbital and spin magnetic moments maintained parallel to each other by strong spin-orbit coupling (J = L - S for light R elements Pr, Nd, Sm; J = L + S for heavy R elements Tb, Dy,...). However, the localized characters of the wave functions lead to low ordering temperatures of the lanthanide elements far below room temperature due to the absence of direct magnetic interaction between neighbors. In these materials, the exchange interaction between 4f electrons is indirect, mediated by 5d, 6s electrons. In contrast, the 3d-electrons responsible for magnetism in transition metals occupies the outer shell whereas in metals they participate in the band structure, resulting in strong coupling magnetic interactions and high Curie temperatures. As a consequence, in order to take advantages of both aspects, the combination of lanthanide and transition metal atoms can generate both properties: a high magnetization and high Curie temperature. This forms an important class of materials that provide new opportunities for applications in magnetoelectric – based devices.

The search for magnetostrictive materials having Curie temperature above room temperature started actively in 1970s. The main conventional track was to combine magnetostrictive rare earth elements, like Tb and Dy, with the ferromagnetic transition metals having high Curie temperature, means Ni, Co and Fe. Bulk synthesis as well as thin films deposition techniques was used. The highest ordering temperatures are found in the Laves phase RFe_2 compounds. $TbFe_2$ and $SmFe_2$ exhibit huge room temperature magnetostriction due to the high rare earth concentration and high Curie temperature. In the case of $TbFe_2$, a magnetostriction coefficient of 1750×10^{-6} with a Curie temperature of 424 °C was reported. [34] Non-crystalline Tb_xFe_{1-x} (x~1/3) alloys also possess comparatively high Curie temperatures and large room temperature magnetostriction.

To consider the integration of magnetostrictive layers into devices for applications, another major requirement is that the materials exhibit large low-field magnetostrictive susceptibility.

It needs to be typically larger than 2×10^{-2} T^{-1} and in the meantime the coercive field of the material is expected to be lower than 100 mT. Based on materials like amorphous Terfenol ($TbFe_2$) and Terfenol-D ($TbDyFe_2$) alloys, different strategies have been developed. If polycrystalline bulk Terfenol-D exhibits a room temperature magnetostriction of $\lambda_s \approx 1500\times10^{-6}$ and $T_C = 650$ K, it exhibits in thin films the large coercive field that is detrimental for device applications. Taking advantage of the stronger Tb-Co exchange interaction, the amorphous a-$TbCo_2$ alloys (named a-TercoNéel) was found to exhibit higher ordering temperature and higher magnetostriction. By replacing iron by cobalt, it has overcome the disadvantage of the high coercive field in the amorphous Terfenol alloys. Duc et al. have succeeded by substituting Co for Fe in the a-Tb-$(Fe, Co)_2$. [35] The studies showed that a high record magnetostriction coefficient $\lambda_{\gamma,2} = 1040\times10^{-6}$ at high field which is fully developed at low fields achieved at an optimum substitution concentration in a-$Tb(Fe_{0.55}Co_{0.45})_{1.5}$.

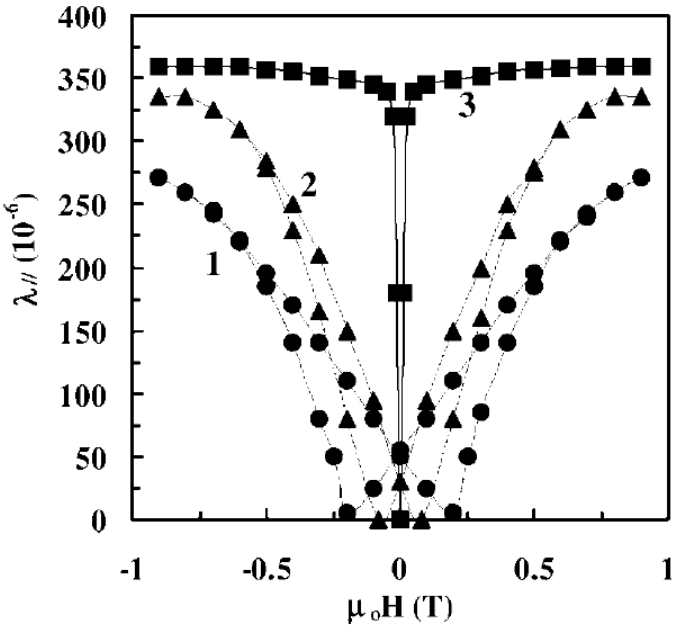

Figure I-10: Parallel magnetostrictive hysteresis loops in the external fields for a-$Tb(Fe_{0.55}Co_{0.45})_{1.5}$ film for different annealing temperatures. (1) as deposited and (2) annealed at 250 °C and (3) 350 °C [35]

Figure I-10 presents the experimental results of this material for three different situations: as grown at room temperature, annealed at 250°C and 350°C. As can be seen, the higher the annealing temperature, the higher the magnetostrictive susceptibility.

All the provided work on intermetallic magnetostrictive materials have seen emerging suitable composition of new materials allowing low magnetic field response of magnetostriction in thin films form opening the route for device applications.

I.5 Magnetoelectric sensors

Some first efforts on particulate composites did not achieve expected results with the composite, due to a ME response that did not exceed the value of 100 $mV.cm^{-1}.Oe^{-1}$ [36]–[38]. Several main reasons were identified such as: chemical reactions between the constituents and/or their starting materials during the sintering process at high temperature, which leads to a formation of unexpected phases that reduce composite properties; the limitation of the mechanical coupling between the particles of the different constituents due to mechanical defects. Drawbacks of particulate composites were overcome by using epoxy method to combine two phases of materials. Giang et al. [39] reported a huge ME voltage coefficient at up to 132.1$V.cm^{-1}.Oe^{-1}$ on the ME magnetic-field sensor with the dimension of 15 mm × 1 mm. An out-of-plane polarized piezoelectric 200-µm-thick PZT plate was bonded with the 18-µm-thick Ni-based magnetostrictive laminates (Metglas) as shown in Figure I-11.

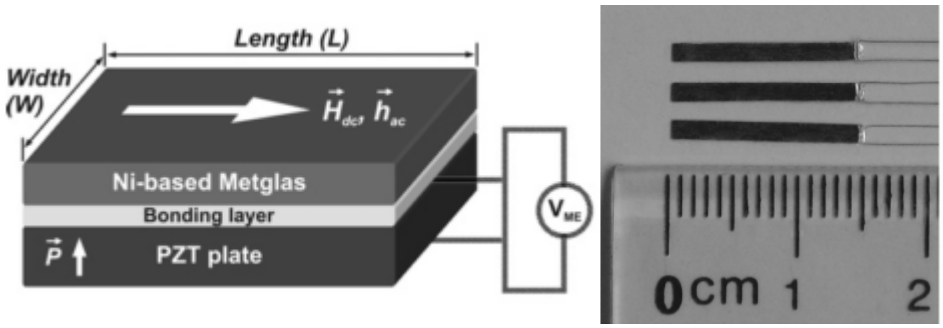

Figure I-11: (left) Schematic of the bilayer Ni-based Metglas/PZT composite configuration. Vector H_{dc}, h_{ac} and P shows the applied magnetic fields and the electrical polarization direction, respectively (right) Sensor construction: Ni-based Metglas/PZT 15 mm × 1 mm laminates [39]

To date, many types of research [40], [41] have been done to optimize the ME coupling in laminated composites based on three main approaches:

(i) optimize the basic material parameter of the constituent phases such as dielectric constant, the piezoelectric and magnetostriction coefficients [42], [43];

(ii) optimize the design of ME laminate sensors [44], [45];

(iii) the operation mode [45]–[47]. In 2006, Dong et al. reported the value of the ME coefficient of 22 V.cm-1.Oe-1 for laminated composites at low frequency for long-type three-layer laminates of Metglas and PZT fiber layers operated in longitudinal-longitudinal (or L-L) push-pull mode [48]. The ME coefficient increases significantly up to 400 $V.cm^{-1}.Oe^{-1}$ near the electromechanical resonance 30 kHz of this L-L mode.

Most applications based on the ME effect, however, focus on bulk or laminated materials that make it difficult to integrate for micro applications due to big size and high-power consumption. Thanks to advances in thin film growth techniques, studies on this ME coupling still have the potential to optimize the material, configuration to obtain a smaller size of sensors with sensitivity that meets the application requirements. The main challenge that needs to be faced is the reduction of signal when decreasing the size. Better surface quality and the disappearance of the bonding layer between two phases of materials existing in the laminate-based ME sensors are expected to enhance the coupling interactions between two phases of materials, thereby helping to overcome the size constraint. S Marauska et al. [49], reported experimental ME coefficient of 80 V/cm.Oe on the micro ME cantilever beam of SiO_2/Ti/Pt/AlN/Cr/FeCoSiB with a thickness of $4\,\mu m$ and lateral dimensions of 0.2 mm$\times$ $1.12\,mm$. Despite of low value of the ME coefficient in compare to state-of-the-art centimeter-sized ME sensors, this demonstrates the ability to develop MEMS-based ME sensors.

I.6 Silicon integrated layers for magnetoelectric devices

For multifunctional oxides like PZT, optimal physical properties are obtained when the material is crystalized. When integrated as active layer in devices, the main challenge is then to obtain heteroepitaxial growth of epitaxial oxides on silicon. The integration on a silicon substrate is an important key where silicon defines the standard of CMOS technology with a large number of available processing options and tools at the standard of micro-technology. However, the direct epitaxy of oxide on silicon faces the major problem of the diffusion of the oxygen in the silicon during the high temperature growth deposition step. To overcome this issue, many types of buffer layers have been investigated to promote the growth of epitaxial perovskites like PZT onto silicon such as MgO [50] or Y_2O_3-doped ZrO_2 [39] being some of

the most common. This buffers are not perovskites materials but in 1998, Mckee et al. [55] reported the epitaxial growth of $SrTiO_3$ (STO) directly on (001) Si using Molecular Beam Epitaxy (MBE) at low pressure typically around 10^{-8} Torr. Many researchers, since then, have succeeded in the growth of STO on Si and multifunction oxides on STO/Si template [56]–[58]. Operation at an extreme high vacuum along with having to use the second method for depositing other materials, however, lead to the desire to find another method that is compatible with technology developments. Among these buffer-layers such as alumina (Al_2O_3)[59] or magnesia (MgO) [50], a popular choice is Yttria-stabilized zirconia (YSZ) which has been improved its ability for replacing a single perovskite STO layer grown by MBE [60][61]. In this thesis, according to its phase diagram, YSZ ceramic of 8 mol% Y_2O_3-doped ZrO_2 was chosen. At high temperature, as shown in the phase diagram in Figure I-12, YSZ exhibits a cubic phase of the theoretical lattice parameter of 5.14 Å, sufficiently close to the silicon lattice (5.43 Å) ensuring a cubic-on-cubic epitaxial with a mismatch of 5.3 %. Besides that, YSZ shows high chemical stability and a large relative dielectric constant of about 30 at room temperature ensuring a correct isolation between active layers deposited on top with the silicon substrate [62].

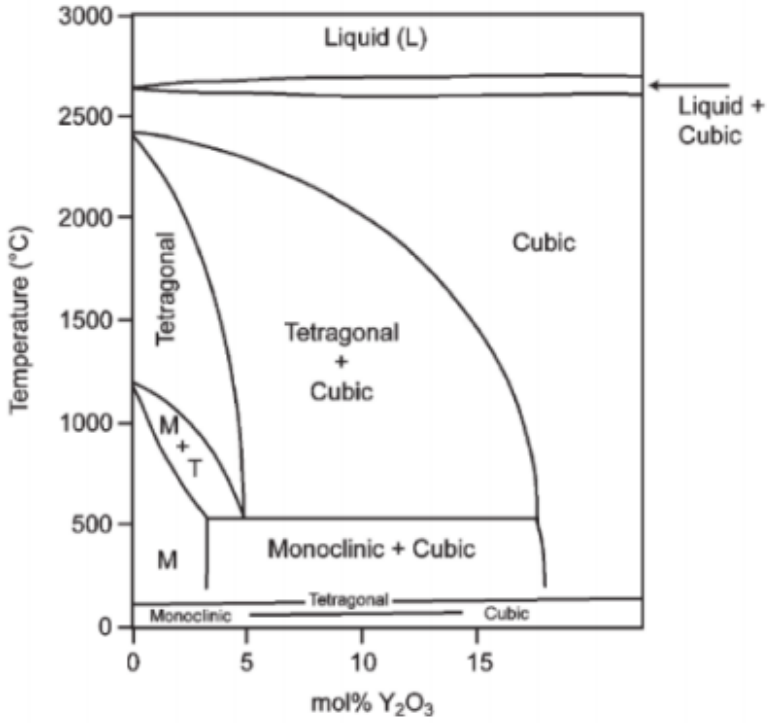

Figure I-12: Diagram phase of YSZ as a function of temperature [63]

At high vacuum pressures of around 10^{-6} Torr, YSZ exhibits an important growth advantage that it activates with the amorphous native SiO_2 at the surface of Si with formation of ZrO_2 and desorption of SiO as the following reactions [64]:

$$\boldsymbol{Zr + 2SiO_2 \rightarrow Zr - silicate \rightarrow ZrO_2 + SiO}$$

$$\boldsymbol{Zr + 2SiO_2 \rightarrow Zr - silicate \rightarrow Zr + SiO_2 \rightarrow ZrO_2 + SiO}$$

The epitaxial relationship between YSZ and silicon substrate is (001)YSZ || (001)Si or cubic-on-cubic alignment [65], [66]. The epitaxial relationship, however, between the perovskite compounds and YSZ is (011) of perovskite || (001) of YSZ [67]. In the case of direct growth on YSZ the lattice mismatch between perovskites and YSZ is too large (typically around 5%). To accommodate, a thin layer of cubic CeO_2 material is directly grown on YSZ prior to the deposition of the perovskite of interest. Cerium oxide also grows epitaxially with cube-on-cube alignment on YSZ thin film. For these reasons, double YSZ/CeO_2 buffer layers on Si will be used as templates for depositing all following perovskite-oxide layers with a lattice mismatch of one or two percent.

Material	**Structure**	**a** (nm)	**b** (nm)	**c** (nm)	**Thermal expansion** ($x10^{-6}$ K^{-1})	**Ref.**
Si	Cubic	0.543	0.543	0.543	3.8	[66]
YSZ $(ZrO_2)_{92}(Y_2O_3)_8$	Cubic	0.514	0.514	0.514	10	[68]
CeO_2	Cubic	0.541	0.541	0.541	11.289	[69]
$SrTiO_3$	Cubic	0.3926	0.3926	0.3926	9.4 – 11.1	[70]
$La_{0.66}Sr_{0.33}MnO_3$	Orthorhombic	0.5488	0.5524	0.787	13.4	[71][72]
$SrRuO_3$	Orthorhombic	0.557	0.5530	0.7856	10.3	[73][74]
$P(Zr_{0.52}Ti_{0.48})O_3$	Tetragonal	0.405	0.405	0.411	6	[75]

Table I-1: Lattice parameters and thermal expansion of materials integrated in this work.

The integration of piezoelectric materials for device applications in this work requires a bottom electrode, a layer that plays an important role, not only in contribution an electrical output, but also affect the quality of active layers of the device. To facilitate the growth of PZT, epitaxial $La_{0.66}Sr_{0.33}MnO_3$ and $SrRuO_3$ which show a good lattice match with PZT, with the pseudo-cubic perovskite and quasi-cubic perovskite structure, respectively, can been chosen [76]–[79]. Goh et al., reported that $La_{0.66}Sr_{0.33}MnO_3$ deposited directly on YSZ/Si grown in a mixture of randomly oriented polycrystalline grains[80]. Besides that, according to Groenen et al [81], the epitaxial $La_{0.66}Sr_{0.33}MnO_3$ shows a strong temperature dependent crystallinity and a polycrystalline form was observed at high temperature (800°C) when deposited directly on CeO_2 layer. To prevent such effect, a solution can be to add another interfacial layer such as STO or SRO between LSMO and CeO_2.

References

[1] K. E. Kuijk, W J Van Gestel, and F W Gorter, “The barber pole, a linear magneto-reslstlve head,” *IEEE Trans Magn, MAG-11*, pp. 1215–1217, 1975.

[2] Y. Makmo, “New breed of magneto-resistance element solves magnetic sensing prob-lems,” *J Electron Eng*, vol. 105, pp. 34–38, 1975.

[3] A. Jander, C. Smith, and R. Schneider, “Magnetoresistive sensors for nondestructive evaluation,” in *the 10th SPIE International Symposium, Nondestructive Evaluation for Health Monitoring and Diagnostics*, 2005.

[4] A. Bernieri, G. Betta, L. Ferrigno, and M. Laracca, “Improving performance of gmr sensors,” *IEEE Sens. J.*, vol. 13, no. 11, pp. 4513–4521, 2013.

[5] J. C. Slonczewski, “Conductance and exchange coupling of two ferromagnets separated by a tunneling barrier,” *Phys. Rev. B*, vol. 39, no. 10, pp. 6995–7002, 1989.

[6] J. M. Hu, T. Nan, N. X. Sun, and L. Q. Chen, “Multiferroic magnetoelectric nanostructures for novel device applications,” *MRS Bull.*, vol. 40, no. 9, pp. 728–735, 2015.

[7] M. P. Lecoeur, Editors: JMD. Coey, and S. Prakin, “Magnetic sensors, in Handbook on Magnetism and Magnetic Materials,” *to be Publ.*

[8] X. Zhuang, M. L. C. Sing, C. Dolabdjian, Y. Wang, P. Finkel, J. Li, and D. Viehland, “Mechanical noise limit of a strain-coupled magneto(elasto)electric sensor operating under a magnetic or an electric field modulation,” *IEEE Sens. J.*, vol. 15, no. 3, pp. 1575–1587, 2015.

[9] D. Pantel, S. Goetze, D. Hesse, and M. Alexe, “Reversible electrical switching of spin polarization in multiferroic tunnel junctions,” *Nat. Mater.*, vol. 11, pp. 289–293, 2012.

[10] N. H. Duc, B. D. Tu, N. T. Ngoc, V. D. Lap, and D. T. H. Giang, “Metglas/PZT-magnetoelectric 2-D geomagnetic device for computing precise angular position,” *IEEE Trans. Magn.*, vol. 49, no. 8, pp. 4839–4842, 2013.

[11] W.C Röntgen, “Ueber die durch Bewegung eines im homogenen electrischen Felde befindlichen Dielectricums hervorgerufene electrodynamische Kraft,” *Ann. Phys*, vol. 35, pp. 264–270, 1888.

[12] D. N. Astrov, “Magnetoelectric effect in Chromium Oxide,” *Sov. Phys. JETP*, vol. 13, no. 4, pp. 729–733, 1961.

[13] N. Ortega, A. Kumar, J. F. Scott, R. S. Katiyar, P. Rico, and S. Juan, “Multifunctional Magnetoelectric Materials for Device Applications,” *Cornell Univ. Libr.*, pp. 1–31, 2014.

[14] J. Ryu, S. Priya, K. Uchino, and H. E. Kim, “Magnetoelectric effect in composites of magnetostrictive and piezoelectric materials,” *J. Electroceramics*, vol. 8, no. 2, pp. 107–119, 2002.

[15] J. Zhai, Z. Xing, S. Dong, J. Li, and D. Viehland, “Magnetoelectric laminate composites: An overview,” *J. Am. Ceram. Soc.*, vol. 91, no. 2, pp. 351–358, 2008.

[16] Z. Junyi, Z. Xing, D. Shuxiang, L. Jiefang, and D. Viehland, “Thermal noise cancellation

in symmetric magnetoelectric bimorph laminates," *Appl. Phys. Lett.*, vol. 93, p. 072906, 2008.

[17] H. Zheng, J. Kreisel, Y. H. Chu, R. Ramesh, and L. Salamanca-Riba, "Heteroepitaxially enhanced magnetic anisotropy in BaTiO3- CoFe2O4 nanostructures," *Appl. Phys. Lett.*, vol. 90, p. 113113, 2007.

[18] J. Li, I. Levin, J. Slutsker, V. Provenzano, P. K. Schenck, R. Ramesh, J. Ouyang, and A. L. Roytburd, "Self-assembled multiferroic nanostructures in the Co Fe 2 O 4 -PbTi O 3 system," *Appl. Phys. Lett.*, vol. 87, p. 072909, 2005.

[19] N. M. Aimon, D. Hun Kim, H. Kyoon Choi, and C. a. Ross, "Deposition of epitaxial BiFeO3/CoFe2O4 nanocomposites on (001) SrTiO3 by combinatorial pulsed laser deposition," *Appl. Phys. Lett.*, vol. 100, p. 092901, 2012.

[20] Z. Zhao, M. Jamali, N. D'Souza, D. Zhang, S. Bandyopadhyay, J. Atulasimha, and J.-P. Wang, "Giant Voltage Manipulation of MgO-based Magnetic Tunnel Junctions via Localized Anisotropic Strain: Pathway to Ultra-Energy-Efficient Memory Technology," *Appl. Phys. Lett.*, vol. 109, p. 092403, 2016.

[21] T. Jin, L. Hao, J. Cao, M. Liu, H. Dang, Y. Wang, D. Wu, J. Bai, and F. Wei, "Electric field control of anisotropy and magnetization switching in CoFe and CoNi thin films for magnetoelectric memory devices," *Appl. Phys. Express*, vol. 7, p. 043002, 2014.

[22] B. Noheda, J. Gonzalo, L. Cross, and R. Guo, "Tetragonal-to-monoclinic phase transition in a ferroelectric perovskite: The structure of PbZr0.52 Ti0.48 O3," *Phys. Rev. B*, vol. 61, no. 13, pp. 8687–8695, 2000.

[23] I. Stolichnov, A. Tagantsev, E. Colla, and N. Setter, "Kinetics of polarization reversal in ferroelectric films: Role of domain nucleation and domain wall motion," *Ceram. Int.*, vol. 30, no. 7, pp. 1095–1099, 2004.

[24] H. Orihara, S. Hashimoto, and Y. Ishibashi, "A Theory of D-E Hysteresis Loop Based on the Avrami Model," *Journal of the Physical Society of Japan*, vol. 63, no. 3. pp. 1031–1035, 1994.

[25] H. Nazeer, M. D. Nguyen, Ö. S. Sukas, G. Rijnders, L. Abelmann, and M. C. Elwenspoek, "Compositional Dependence of the Young ' s Modulus Pulsed Laser Deposited PZT Thin Films," vol. 24, no. 1, pp. 166–173, 2015.

[26] H. Nazeer, M. D. Nguyen, G. Rijnders, L. Abelmann, and Ö. S. Sukas, "Microelectronic Engineering Residual stress and Young's modulus of pulsed laser deposited PZT thin fi lms : Effect of thin fi lm composition and crystal direction of Si cantilevers," *MEE*, vol. 161, pp. 56–62, 2016.

[27] R. Guo, L. E. Cross, S.-E. Park, B. Noheda, D. E. Cox, and G. Shirane, "Origin of the high piezoelectric response in PbZr1-xTixO3," *Phys. Rev. Lett.*, vol. 84, no. 23, pp. 5423–5426, 2000.

[28] B. Noheda, D. E. Cox, G. Shirane, R. Guo, B. Jones, and L. E. Cross, "Stability of the monoclinic phase in the ferroelectric perovskite PbZr1-xTixO3," *Phys. Rev. B*, vol. 63, p. 014103, 2001.

[29] B. Noheda, J. Gonzalo, L. Cross, and R. Guo, "Tetragonal-to-monoclinic phase transition in a ferroelectric perovskite: The structure of PbZr0.52 Ti0.48 O3," *Phys. Rev.*

B, vol. 61, no. 13, pp. 8687–8695, 2000.

[30] P. Curie, Jacques; Curie, "Development, via compression, of electric polarization in hemihedral crystals with inclined faces," *Bull. la Société minérologique Fr.*, vol. 3, pp. 90–93, 1880.

[31] G. Lippmann, "Principle of the conservation of electricity," *Ann. Chim. Phys.*, vol. 24, pp. 145–177, 1881.

[32] S.-B. Kim, H. Park, S.-H. Kim, H. C. Wikle, J.-H. Park, and D.-J. Kim, "Comparison of MEMS PZT Cantilevers Based on d31 and d33 Modes for Vibration Energy Harvesting," *J. Microelectromechanical Syst.*, vol. 22, no. 1, pp. 26–33, 2013.

[33] D. T. Huong Giang, "Elaboration and study of giant magnetostrictice single layer and multilayer fims based on TbFeCo compound," Uviversite de Rouen and Vietnam national university, Hanoi, 2005.

[34] A. E. Clark, H. S. Belson, and R. E. Strakna, "Elastic properties of rare-earth-iron compounds," *J. Appl. Phys.*, vol. 44, no. 6, pp. 2913–2914, 1973.

[35] N. H. Duc, T. Danh, H. N. Thanh, J. Teillet, and A. Lienard, "Structural , magnetic , Mössbauer and magnetostrictive studies of amorphous Tb(Fe0.55Co0.45)1.5 films," *J. Phys. Condens. Matter 12*, vol. 12, pp. 8283–8293, 2000.

[36] J. vanden BOOMGAARD and R. A. J. BORN, "A sintered magnetoelectric composite material BaTiO3-Ni(Co,Mn)Fe204," *J. Mater. Sci.*, vol. 13, pp. 1538–1548, 1978.

[37] G. Srinivasan, E. T. Rasmussen, A. A. Bush, K. E. Kamentsev, V. F. Meshcheryakov, and Y. K. Fetisov, "Structural and magnetoelectric properties of MFe2O 4-PZT (M = Ni, Co) and Lax(Ca, Sr)1-xMnO 3-PZT multilayer composites," *Appl. Phys. A Mater. Sci. Process.*, vol. 78, no. 5, pp. 721–728, 2004.

[38] N. Nersessian, S. W. Or, and G. P. Carman, "Magnetoelectric behavior of terfenol-D composite and lead zirconate titanate ceramic laminates," *IEEE Trans. Magn.*, vol. 40, no. 4, pp. 2646–2648, 2004.

[39] D. T. H. Giang, P. A. Duc, N. T. Ngoc, and N. H. Duc, "Geomagnetic sensors based on Metglas/PZT laminates," *Sensors Actuators, A Phys.*, vol. 179, pp. 78–82, 2012.

[40] Y. Wang, J. Li, and D. Viehland, "Magnetoelectrics for magnetic sensor applications: Status, challenges and perspectives," *Materials Today*, 2014.

[41] M. Fiebig, "Revival of the magnetoelectric effect," *J. Phys. D. Appl. Phys.*, vol. 38, no. 8, pp. R123–R152, 2005.

[42] M. Li, D. Berry, J. Das, D. Gray, J. Li, and D. Viehland, "Enhanced sensitivity and reduced noise floor in magnetoelectric laminate sensors by an improved lamination process," *J. Am. Ceram. Soc.*, vol. 94, no. 11, pp. 3738–3741, 2011.

[43] J. Gao, J. Das, Z. Xing, J. Li, and D. Viehland, "Comparison of noise floor and sensitivity for different magnetoelectric laminates," *J. Appl. Phys.*, vol. 108, p. 084509, 2010.

[44] M. I. Bichurin, V. M. Petrov, S. V. Averkin, and E. Liverts, "Present status of theoretical modeling the magnetoelectric effect in magnetostrictive-piezoelectric nanostructures. Part I: Low frequency and electromechanical resonance ranges," *J. Appl. Phys.*, vol. 107,

no. 5, p. 053904, 2010.

[45] Y. Wang, D. Hasanyan, M. Li, J. Gao, J. Li, and D. Viehland, "Equivalent magnetic noise in multi-push-pull configuration magnetoelectric composites: Model and experiment," *IEEE Trans. Ultrason. Ferroelectr. Freq. Control*, vol. 60, no. 6, pp. 1227–1233, 2013.

[46] D. Hasanyan, J. Gao, Y. Wang, R. Viswan, M. Li, Y. Shen, J. Li, and D. Viehland, "Theoretical and experimental investigation of magnetoelectric effect for bending-tension coupled modes in magnetostrictive-piezoelectric layered composites," *J. Appl. Phys.*, vol. 112, p. 013908, 2012.

[47] J. Gao, Y. Shen, Y. Wang, P. Finkel, J. Li, and D. Viehland, "Magnetoelectric Bending-Mode Structure Based on Metglas / Pb (Zr , Ti) O 3 Fiber Laminates," *EEE Trans. Ultrason. Ferroelectr. Freq. Control*, vol. 58, no. 8, pp. 1545–1549, 2011.

[48] S. Dong, J. Zhai, J. Li, and D. Viehland, "Near-ideal magnetoelectricity in high-permeability magnetostrictive/ piezofiber laminates with a (2-1) connectivity," *Appl. Phys. Lett.*, vol. 89, no. 25, pp. 2–5, 2006.

[49] S. Marauska, R. Jahns, H. Greve, E. Quandt, R. Knöchel, and B. Wagner, "MEMS magnetic field sensor based on magnetoelectric composites," *J. Micromechanics Microengineering*, vol. 22, p. 065024, 2012.

[50] D. K. Fork, F. A. Ponce, J. C. Tramontana, and T. H. Geballe, "Epitaxial MgO on Si(001) for Y-Ba-Cu-O thin-film growth by pulsed laser deposition," *Appl. Phys. Lett.*, vol. 58, no. 20, pp. 2294–2296, 1991.

[51] S. H. Baek and C. B. Eom, "Epitaxial integration of perovskite-based multifunctional oxides on silicon," *Acta Mater.*, vol. 61, no. 8, pp. 2734–2750, 2013.

[52] N. A. Basit, H. K. Kim, and J. Blachere, "Growth of highly oriented Pb(Zr,Ti)O3 films on MgO-buffered oxidized Si substrates and its application to ferroelectric nonvolatile memory field-effect transistors," *Appl. Phys. Lett.*, vol. 73, no. 26, pp. 3941–3943, 1998.

[53] Y. K. Wang, T. Y. Tseng, and P. Lin, "Enhanced ferroelectric properties of Pb(Zr0.53Ti0.47)O3 thin films on SrRuO3/Ru/SiO2/Si substrates," *Appl. Phys. Lett.*, vol. 80, no. 20, pp. 3790–3792, 2002.

[54] B. T. Liu, K. Maki, Y. So, V. Nagarajan, R. Ramesh, J. Lettieri, J. H. Haeni, D. G. Schlom, W. Tian, X. Q. Pan, F. J. Walker, and R. A. McKee, "Epitaxial La-doped SrTiO3 on silicon: A conductive template for epitaxial ferroelectrics on silicon," *Appl. Phys. Lett.*, vol. 80, no. 25, pp. 4801–4803, 2002.

[55] R. A. McKee, F. J. Walker, and M. F. Chisholm, "Crystalline oxides on silicon: The first five monolayers," *Phys. Rev. Lett.*, vol. 81, no. 14, pp. 3014–3017, 1998.

[56] A. M. Kolpak, F. J. Walker, J. W. Reiner, Y. Segal, D. Su, M. S. Sawicki, C. C. Broadbridge, Z. Zhang, Y. Zhu, C. H. Ahn, and S. Ismail-Beigi, "Interface-induced polarization and inhibition of ferroelectricity in epitaxial SrTiO3/Si," *Phys. Rev. Lett.*, vol. 105, no. 21, pp. 1–4, 2010.

[57] O. H.Jörg, "Crystalline oxides on silicon," *Springer Ser. Adv. Microelectron.*, vol. 43, pp. 395–423, 2013.

[58] M. P. Warusawithana, C. Cen, C. R. Sleasman, J. C. Woicik, Y. Li, L. F. Kourkoutis, J. A. Klug, H. Li, P. Ryan, L.-P. Wang, M. Bedzyk, D. A. Muller, L.-Q. Chen, J. Levy, and D. G. Schlom, "A Ferroelectric Oxide Made Directly on Silicon," *Science (80-.).*, vol. 324, pp. 367–370, 2009.

[59] M. Ishida, I. Katakabe, T. Nakamura, and N. Ohtake, "Epitaxial Al2O3 films on Si by low-pressure chemical vapor deposition," *Appl. Phys. Lett.*, vol. 52, no. 16, pp. 1326–1328, 1988.

[60] D. K. Fork, D. B. Fenner, R. W. Barton, J. M. Phillips, G. A. N. Connell, J. B. Boyce, and T. H. Geballe, "High critical currents in strained epitaxial YBa2Cu3O7 - delta on Si," *Appl. Phys. Lett.*, vol. 57, no. 11, pp. 1161–1163, 1990.

[61] A. Chen, Z. Bi, H. Hazariwala, X. Zhang, Q. Su, L. Chen, Q. Jia, J. L. Macmanus-Driscoll, and H. Wang, "Microstructure, magnetic, and low-field magnetotransport properties of self-assembled (La0.7Sr0.3MnO3)0.5:(CeO2)0.5 vertically aligned nanocomposite thin films.," *Nanotechnology*, vol. 22, p. 315712, 2011.

[62] G. A. Samara, "Low-temperature dielectric properties of candidate substrates for high-temperature superconductors: LaAlO3 and ZrO2: 9.5 mol % Y2O3," *J. Appl. Phys.*, vol. 68, no. 8, pp. 4214–4219, 1990.

[63] H. . Scott, "Phase relationships in the zirconia-yttria system.," *J. Mater. Sci.*, vol. 10, no. 9, pp. 1527–1535, 1975.

[64] S. J. Wang and C. K. Ong, "Epitaxial Y-stabilized ZrO2 films on silicon: Dynamic growth process and interface structure," *Appl. Phys. Lett.*, vol. 80, no. 14, pp. 2541–2543, 2002.

[65] P. D. Brown, "Yttria stabilized zirconia buffered silicon : substrates for YBCO microwave applications," *Florida Int. Univ.*, 1998.

[66] M. Laurence, J. Vill, G. Rolland, and F. Laugier, "Double CeO2/YSZ buffer layer for the epitaxial growth of YBa2Cu307_ films on Si (001)substrates," *Phys. C*, vol. 269, pp. 124–130, 1996.

[67] C. A. Copetti, H. Soltner, J. Schubert, W. Zander, O. Hollricher, C. Buchal, H. Schulz, N. Tellmann, and N. Klein, "High quality epitaxy of YBa2Cu3O7-x on silicon-on-sapphire with the multiple buffer layer YSZ/CeO2," *Appl. Phys. Lett.*, vol. 63, no. 10, pp. 1429–1431, 1993.

[68] M. B. Pomfret, C. Stoltz, B. Varughese, and R. A. Walker, "Structural and compositional characterization of yttria-stabilized zirconia: Evidence of surface-stabilized, low-valence metal species," *Anal. Chem.*, vol. 77, no. 6, pp. 1791–1795, 2005.

[69] A. collection of papers presented at the 39th international conference on A. ceramics and Composites., "Developments in strategic ceramic materials," p. 172, 2015.

[70] P. Paufler, B. Bergk, M. Reibold, A. Belger, N. Pätzke, and D. C. Meyer, "Why is SrTiO3 much stronger at nanometer than at centimeter scale?," *Solid State Sci.*, vol. 8, pp. 782–792, 2006.

[71] Q. J. Huang, Y. Cheng, X. J. Liu, X. D. Xu, and S. Y. Zhang, "Study of the elastic constants in a La0.6Sr0.4MnO3 film by means of laser-generated ultrasonic wave method," *Ultrasonics*, vol. 44, pp. 1223–1227, 2006.

[72] F. Yang, S. Kim, and Y. Takamura, “Strain effect on the electrical conductivity of epitaxial La0.67Sr0.33MnO3 thin films,” *Scr. Mater.*, vol. 65, pp. 29–32, 2011.

[73] C. L. Chen, Y. Cao, Z. J. Huang, Q. D. Jiang, Z. Zhang, Y. Y. Sun, W. N. Kang, L. M. Dezaneti, W. K. Chu, and C. W. Chu, “Epitaxial SrRuO3thin films on (001) SrTiO3,” *Appl. Phys. Lett.*, vol. 71, no. 8, pp. 1047–1049, 1997.

[74] S. Yamanaka, T. Maekawa, H. Muta, T. Matsuda, S. I. Kobayashi, and K. Kurosaki, “Thermophysical properties of SrHfO3and SrRuO3,” *J. Solid State Chem.*, vol. 177, pp. 3484–3489, 2004.

[75] S. N. Kallaev, G. G. Gadzhiev, I. K. Kamilov, Z. M. Omarov, S. a. Sadykov, and L. a. Reznichenko, “Thermal properties of PZT-based ferroelectric ceramics,” *Phys. Solid State*, vol. 48, no. 6, pp. 1169–1170, 2006.

[76] C. Chirila, A. G. Boni, I. Pasuk, R. Negrea, L. Trupina, G. Le Rhun, S. Yin, B. Vilquin, I. Pintilie, and L. Pintilie, “Comparison between the ferroelectric/electric properties of the PbZr0.52Ti0.48O3 films grown on Si (100) and on STO (100) substrates,” *J. Mater. Sci.*, vol. 50, pp. 3883–3894, 2015.

[77] J. Fontcuberta, M. Bibes, B. Martı, V. Trtik, C. Ferrater, F. Sánchez, and M. Varela, “Tunable epitaxial growth of magnetoresistive La2/3Sr1/3 MnO 3 thin films,” *J. Appl. Phys.*, vol. 85, no. 8, pp. 4800–4802, 1999.

[78] H. Colder, B. Domengès, C. Jorel, P. Marie, M. Boisserie, S. Guillon, L. Nicu, A. Galdi, L. Méchin, H. Colder, and B. Domenge, “Structural characterisation of BaTiO3 thin films deposited on SrRuO3/YSZ buffered silicon substrates and silicon microcantilevers,” *J. Appl. Phys.*, vol. 115, p. 053506, 2014.

[79] P. Perna, L. M´echin, M. P. Chauvat, P. Ruterana, C. Simon, and U. S. di Uccio, “High Curie temperature for La0.7Sr0.3 MnO3 thin films deposited on CeO2/YSZ-based buffered silicon substrates,” *J. Phys. Condens. Matter*, vol. 21, p. 30605, 2009.

[80] W. C. Goh, K. Yao, and C. K. Ong, “Epitaxial La0.7Sr0.3MnO3 thin films with two in-plane orientations on silicon substrates with yttria-stabilized zirconia and YBa2Cu3O7-delta as buffer layers,” *J. Appl. Phys.*, vol. 97, p. 073905, 2005.

[81] R. Groenen, Z. Liao, N. Gauquelin, R. Hoekstra, B. Spanjer, M. Van Gorsel, S. Borkent, M. Nguyen, L. Vargas-llona, E. Rodijk, C. Damen, and J. Verbeeck, “Epitaxial growth of complex oxides on silicon by enhanced surface diffusion in large area pulsed laser deposition.,” pp. 1–4, 2016.

Chapter II– Experimental methods

This chapter is dedicated to the description of all the experimental techniques that have been used among this work. In the first part are described the growth techniques that allow to integrate high quality epitaxial thin of PZT on silicon by Pulsed Laser Deposition (PLD) as well as magnetostrictive thin films based on TbFeCo alloy using sputtering method. The second section of this chapter describes the characterization tools that allow to extract for the as-deposited samples films the structural properties by X-ray diffraction (XRD) and the surface morphology by Atomic Force Microscopy (AFM). The general description of these techniques is given as well as the way of choosing the key parameters to extract the typical characteristics of each film. The main techniques are shortly introduced such as typical process flow for the realization of micro-systems. Last section focuses on the way to extract the functional properties of the material by means of electrical or mechanical characterizations, respectively for both piezoelectric and magnetostrictive materials used in this work. A detailed description of each technique is given such as their pros and cons, based on the literature.

Content:

II.1 Thin film growth

II.1.1 Growth of PZT thin films - Pulsed Laser Deposition (PLD) method

II.1.1.a Overall principles

Most recent reports on PZT films integrated in MEMS are based on Sol-Gel or sputtering techniques, both providing high ability for wafer scale integration but often leading to reduced piezoelectric properties [1], [2]. This work aims at taking advantage of high-quality materials to increase the sensitivity of the targeted devices. Additionally, as it is expected to take advantage of coupling between piezoelectric and magnetostrictive layers, sharp interfaces and epitaxial relationship are required to ensure a correct mechanical transfer between the layers. The versatility of the deposition technique is also important for a rapid optimization of the heterostructures. This is the reason why Pulsed Laser Deposition (PLD) technique is used in this work as growth method for oxides films. As shown in chapter 1, this technique allows to produce high quality epitaxial thin films of perovskite. This relates to ability of PLD method to "easily" transfer the stoichiometry of the ablated target as the ablation phenomena is independent from the target composition [3]–[5]. This point is of particular weight in the case of PZT material where piezoelectric properties and piezoelectric coefficients are directly linked to the control of the stoichiometry [6]. Overall principle consists in ablating a target, made of the material to deposit, using a short pulse (typically 25 ns) of high power (typically 10^8 W/cm^2) of UV light (248 nm) produced by an excimer laser. If stoichiometry of the target is usually chosen as the same as the expected material of the desired thin film, in the case of PZT the volatility of Pb at high temperature under oxidizing atmosphere requires an excess of around 10% of Pb in the target for a correct stoichiometry of the film due to the volatility of lead oxide. Growth is performed under pure oxidizing atmosphere (typically 150 mTorr) to allow integration of oxygen in the growing crystalline structure.

Schematically, the physical mechanisms steps of PLD can be divided as follow:

1. Laser-target integration: light is focused on the target and most of its energy is absorbed if the photon energy is larger than the gap from the target.
2. Evaporation of the target material: the high temperature induced by light absorption induces explosive evaporation of the material and a plasma is produced.

3. Adiabatic expansion of the plasma: the plasma expands adiabatically and species are slowed down by the background gas in the chamber. Species energy is usually below 1 eV when they reach the sample surface [7].
4. Material growth: evaporated species reach the sample surface, condense, diffuse and nucleate to form a thin film. As produced particle fluxes in PLD are quite large with respect to MBE technics [8], nucleation density is quite high and 2D growth can easily be favored thus allowing the growth of smooth films. The oxidizing atmosphere allows to maintain the oxygen stoichiometry in the film.

II.1.1.b Growth mechanisms and PLD important parameters

The active properties of perovskite thin films are highly influenced by their structural properties and micro-structures. It is thus important to have a good understanding of the mechanisms taking place during growth to optimize the functional properties of the deposited film. PLD growth, as with other deposition techniques, can be divided in different atomic steps of adsorption, diffusion, island nucleation and coalescence [9]. The important parameters that need to be taken into account are related to intrinsic parameters such as the material to be deposited and substrate nature and extrinsic parameters related to the growth conditions.

Intrinsic parameters: to minimize the system energy, the growth of low surface energy is favored [10]–[12], that is in the case of perovskite where often the (100) and (110) planes with respect to the (111) planes are of low surface energy [13]. The interface energy between different materials of the heterostructure is also a parameter to take into account. This energy term is often high in the case of perovskite materials where the presence of charged planes can induce high electrostatic interaction. Additionally, the lattice mismatch of the film with the substrate, the presence of atomic steps or defects that will serve as nucleation sites, are of crucial importance for the final results in term of structural properties of the films.

Extrinsic parameters: Those parameters are related to the growth conditions and can be tuned to optimize the thin film properties. Laser energy and frequency determine the flux of species on the surface and thus highly influence the nucleation step. Oxidizing gas pressure has a strong effect on the energy of the incident atoms but also play a role in the thermodynamic of the thin film formation. Substrate temperature affects the diffusion of the species and the adsorption/desorption ratio and can induce the formation of a high energy orientation that

cannot be obtained at lower temperature. Post deposition annealing step performed in-situ after deposition allow integrating optimal content of oxygen in the film.

II.1.1.c PLD system at C2N

The PLD system used in this thesis is illustrated in Figure II-1. A KrF excimer UV laser Coherent COMPexPro with a wavelength $\lambda = 248\ nm$ and maximum energy of 400 mJ was used. The particular wavelength has been chosen for an appropriate target penetration depth. A laser beam passes through an attenuator to adjust the laser energy and a mask to tune the size of the laser beam and get a homogenous energy on the entire beam surface. The direction of the laser beam can be adjusted by the mirror system. Then the laser beam is focused under 45° angle on the rotating target surface by a lens with 350 mm focal length. The laser spot dimensions range between 0.83×1.6 mm^2 to 0.1× 2 mm^2 depending on the image of the mask t. The range of the laser frequency is between 1Hz and 100 Hz; usually 2-5 Hz of the frequency is used for the PZT growth that allows a good compromise between growth speed and good quality film. This growth rate was optimized for each material in this PLD system and is related to the previously mentioned nucleation phenomena during growth that will be further discussed in chapter 3. An energy density of $2{-}4\ J/cm^2$ is thus deposited on the target surface that is above the ablation threshold.

A target holder that can bear 12 targets in the vacuum chamber allows to deposit several layers, thin films or buffer layers. During the deposition, targets are rotating to avoid local modification of the target during growth. Prior to deposition, the targets are usually cleaned using laser ablation under oxidizing pressure of O_2 (typically 120 mTorr). During the thin film growth, the pressure inside the main chamber is controlled in the range of 10^{-1} Torr to 10^{-6} Torr by adjusting the gas flow (oxygen or nitrogen) using the gas flux regulators. Growth substrates are fixed on a dedicated heater allowing deposition temperatures up to 900°C. The samples are mounted on the holder using silver paste to ensure a good thermal contact. The sample-target distance is fixed at 5 cm thus providing the homogeneity of the deposition area on the sample at a typical value of 5x5 mm. The laser beam is a bit out of the target center to make a circle on the target.

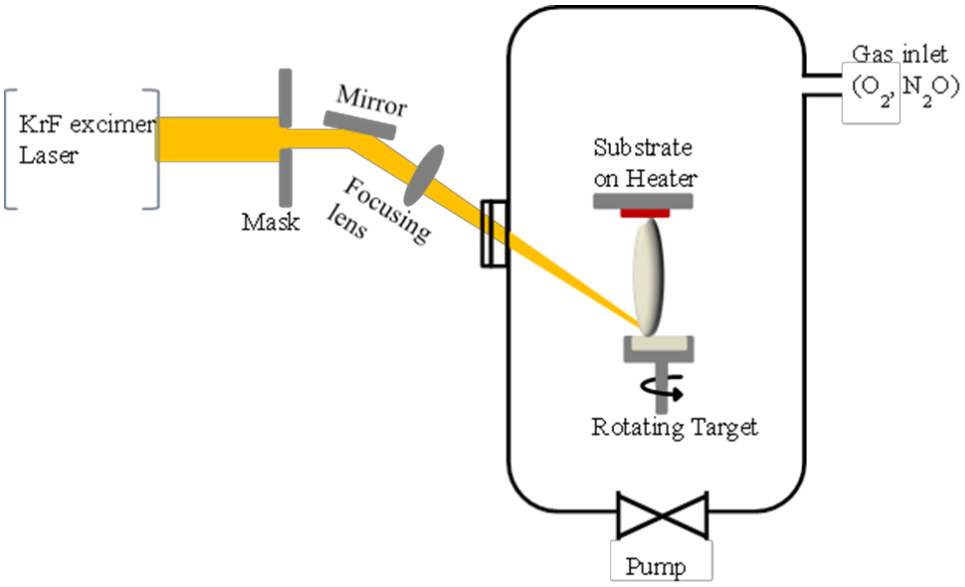

Figure II-1: Sketch of the pulsed laser deposition (PLD) set up as used in this thesis

Each stage in PLD process plays a crucial role in determining the properties of the grown thin film such as the crystalline quality with uniform orientation and surface roughness. The optimization of the different films that are used to integrate PZT on silicon, their growth conditions and associated properties will be further discussed in chapter 3.

II.1.2 Growth of magnetostrictive thin films – sputtering method

Overall principles

Sputtering is a widely-used method of physical vapor deposition involving low pressure gaseous plasma generated by a voltage bias between the target to be sputtered and a reference, usually the sample holder in capacitive coupled systems. A gas of heavy neutral atoms (often Ar) and/or reactive atoms (often O or N) is used to create the plasma that is composed of excited atoms, ions electrons… The negative bias forced (or automatically generated) at the cathode where the target relies attracts the positive Ar ions that transfer their kinetic energy to the target atoms that are sputtered. Those atoms cross the plasma and condense on the samples placed in front. The operating principle of cathode sputtering method is shown in Figure II-2.

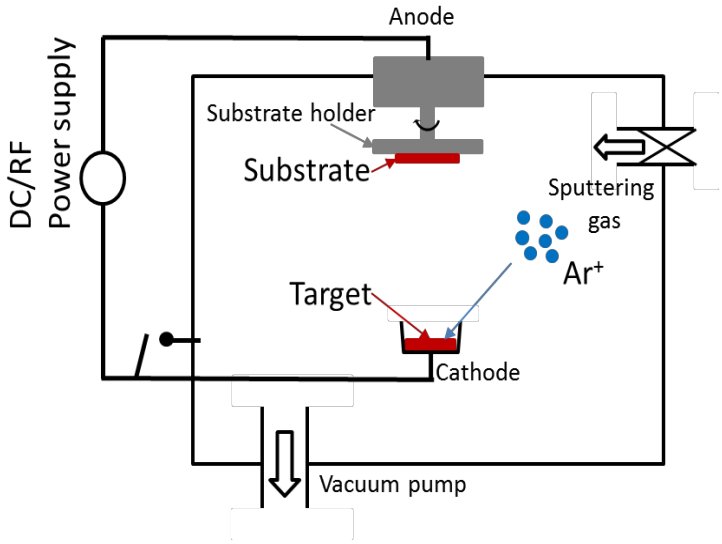

Figure II-2: Diagram of operating principle of cathode sputtering method

There are two types of sputtering conditions: direct current (DC) and radio frequency (RF). The use of DC bias is easier to implement but when the target is insulating, accumulation of ions charges takes place that slow down, or even completely stop the attraction of Ar ion that modify the sputtering rate. In this case, RF excitation can thus be used.

In order to increase the deposition rate, magnetron configuration can be used where magnets are placed nearby the target to densify the plasma by increasing the amount of collisions of charged species in the plasma and thus increasing the number of sputtering ions. In some configuration and in order to improve the crystalline quality, sample holder can be heated to allow the deposited species to diffuse on the surface such as off axis configuration that slow down the deposition rate. Sputtering method offers a good control of films thickness by fixing the operating conditions and adjusting the deposition time. However, the deposition of alloys can be more complex to manage as the sputtering process depend on the atom weight. It can be performed using a target of the desired material, as only the target surface is sputtered, the composition of the obtained thin film remains similar to the one of the target. Other approaches consist in the use of multiple targets sputtered at the same time or a single rotating target with separated area made of the different compounds of the aimed alloy. Using those approaches, it is thus possible to obtain thin film composition with the desired stoichiometry.

In order to maximize the sensitivity of the aimed sensor, the stress transferred by the magnetic film to the piezoelectric cantilever that will lead to a shift of resonant frequency need

to be maximized as well. As a consequence, the choice fell on the use a magnetic film with the highest possible magnetostriction coefficient, this coefficient being representative of the percentage of change of volume at a fixed value of magnetic field with respect to zero magnetic field volume. As discussed in Chapter 1, TbFeCo alloys exhibit magnetostriction coefficient values 2 to 3 orders of magnitude higher that pure material such as Cobalt. All magnetostrictive thin-films of TbFeCo have been deposited on PZT thin-films in Vietnam at VNU-Key *Laboratory* for *Micro-Nano Technology*: Development and Application of Micro-Nanotechnology Fabrication of Materials and Devices. TbFeCo deposition has been optimized on a dedicated sputtering tool using RF polarized magnetron cathodes with an applied power of 75 W. The distance between the sample and the target is fixed at 5 cm. The base pressure before deposition is typically 3.10^{-7} Torr and under Ar flux of 40 SCCM, the total pressure reaches 2.2 mTorr in the chamber. The thickness of the thin films is adjusted by the sputtering time with a typical deposition rate of TbFeCo around $1\ \text{Å}/s$.

Previous studies on TbFeCo thin films [14]–[16] have shown that as-deposited films exhibit a perpendicular magnetic anisotropy with a high value of magnetostriction ($\lambda_{//}$) of 1140×10^{-6} at a high applied magnetic field $\mu_0.H = 0.6\,T$ and a small value of magnetostrictive susceptibility ($\chi_{\lambda_{//}}$) of 0.23×10^{-2} T^{-1}. For this material, the magnetic and magnetostrictive softness has been significantly improved by heat treatment. This process also causes the remarkable decrease of parallel magnetostriction. The TbFeCo films annealed at 350 °C during 1 hour in a vacuum of 10^{-5} Torr show high saturation value of in-plane magnetostriction 370.10^{-6} and high magnetostrictive susceptibility $1{,}8.10^{-2}$ T^{-1}. In order to avoid possibility loss of ferroelectric and piezoelectric properties of PZT at high temperature (near the Curie temperature) and the diffusion of metal from TbFeCo to PZT that would induce leakage current. Another approach was used to enhance the in-plane magnetic anisotropy of the TbFeCo thin-films. During the sputtering process, a bias magnetic field H_{bias} around 400 Oe induced by 2 permanent magnets (see Figure II-3) was applied parallel to the substrate surface.

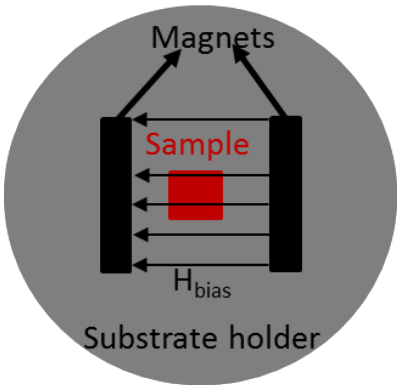

Figure II-3: Experimental setup for the sputtering process of TbFeCo using magnets to enhance the in-plane magnetic anisotropy

In order to ease the investigation of magnetostrictive properties of TbFeCo thin films using the magnetostrictive measurement system that will be presented more in detail in the next section, TbFeCo thin films will be deposited on both $100\ \mu m$ – thick glass substrates and PZT thin-films integrated on Si at the same sputtering conditions.

II.2 Surface and structural analysis

II.2.1 X-ray diffraction

All the as-deposited PZT samples are analyzed by X-Ray Diffraction (XRD) to extract their crystallographic structure and orientation. Additional information can be obtained such as the epitaxial relationship between different layers of the stack. X-ray diffraction occurs when a light source of the appropriate wavelength hits a crystal, with a crystallographic arrangement where atoms act as a light source due to elastic scattering and interact with each other. Either the interaction is constructive, and a signal is observed on the detector that allow to extract an atomic distance, either interaction is destructive, and no signal is measured. This diffraction configuration obey the Bragg law that link the light wavelength with the source and detector angle with respect to the sample [17] as illustrated in Figure II-4.

$$2d.\sin(\theta) = n.\lambda \qquad \textbf{Eq. II-1}$$

Measurement of the diffraction conditions allow to extract the lattice parameters in thin films. This approach consists in moving the source and the detector with respect to the sample in order to find the diffraction conditions at fixed light wavelength.

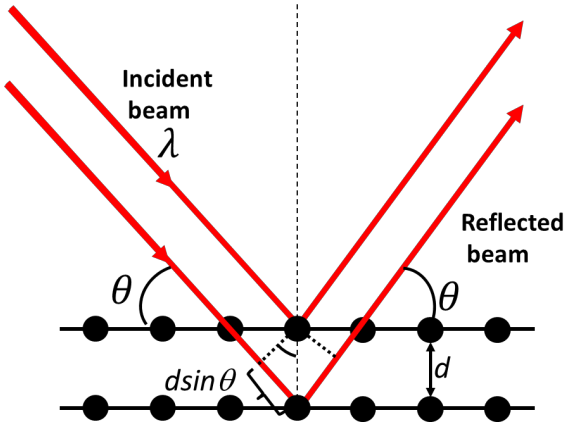

Figure II-4: Schematic representation of Bragg's conditions in description of the Bragg parameters

In this work, a Philipps X'Pert Pro diffractometer is used to make diffracting the planes. This diffractometer has a fixed source, a sample holder which is free to move in the space according to the angle and direction shown in Figure II-5. The source consists in a copper anti-cathode excited by electron bombardment that emits hard X-ray. The incident beam is first made parallel thanks to a reflective parabolic mirror and the $K_{\alpha 1}$ ray is selected using 4 Ge (220) crystals allowing to have a source at a single wavelength $\lambda = 0{,}154051$ nm. A 1/4 ° slit is finally placed on the incident beam to limit the angle dispersion.

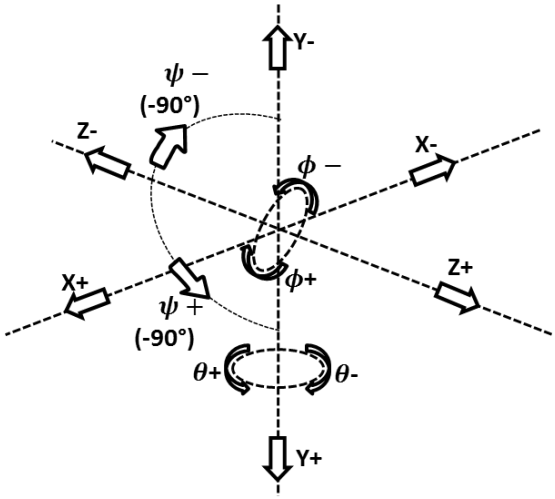

Figure II-5: Angles definitions for diffraction

Out of plane diffraction ($2\theta - \omega$ scan): This consists in obtaining XRD diagrams of planes parallel to the surface of the substrate, typically Si (001) in this work. During this measurement,

the source is fixed, the angle ω between the sample and the incident beam varies and the angle 2θ varies twice as fast as the ω angle does. The position of diffraction peaks along with peak intensities from $\theta - 2\theta$ scan diffraction allows to identify the distance of the atomic planes perpendicular to the substrate surface according to the Bragg law.

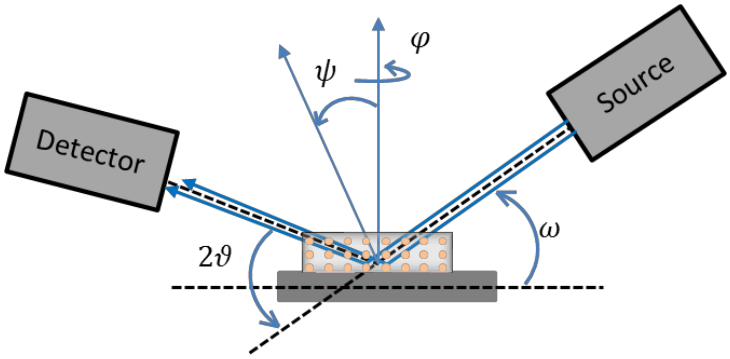

Figure II-6: Sketch of an X-ray diffactometer with a fixed source. Sample and detector can rotate.

Figure II-7 shows a $\theta - 2\theta$ scan diffraction of a CeO_2-YSZ double-buffer layer deposited on Si substrate by PLD. The (002) peak positions (2θ) of CeO_2, YSZ and the (004) peak position of Si substrate are determined and marked. From these peaks positions, the out-of-plane lattice parameters of the deposited materials are obtained from: $d_{hkl} = \lambda/\sin(2\theta)$.

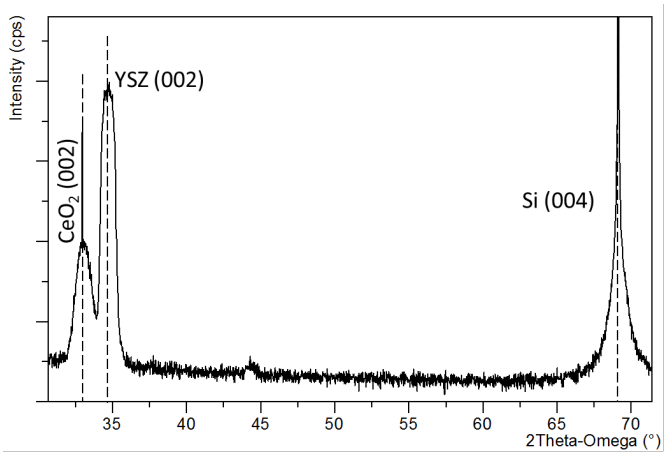

Figure II-7: the $\theta - 2\theta$ scan diffraction of an CeO_2-YSZ double-buffer layer deposited on Si substrate by PLD

Rocking curves (ω – scan) were measured to determine the crystalline quality of a thin film or the degree of mosaicity around the normal to the surface. The used criterion is the Full Width at Half Maximum (FWHM) of the chosen diffraction peak by changing the ω value at a fixed position of the detector (2θ value). In this diffraction conditions, the ability of the crystal to grow around the ideal values and a perfect film/crystal will have a sharp peak where a film exhibiting more defects like mosaicity, dislocations or curvature will be broadened. A typical rocking curve around the (002) peak of YSZ deposited on Si substrate by PLD is shown in Figure II-8.

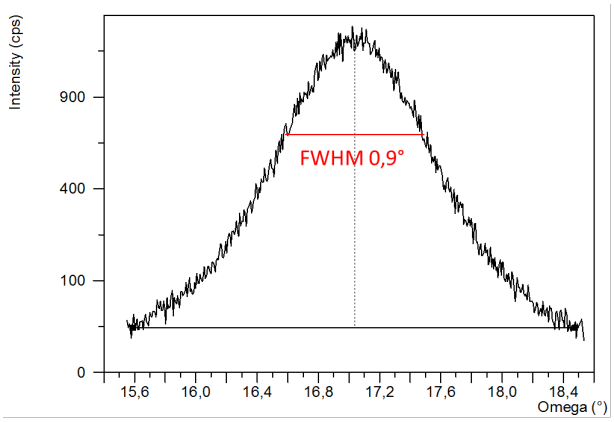

Figure II-8: Typical rocking curve around the (002) peak of YSZ deposited on Si substrate by PLD

Phi – scan ($\varphi - scan$) is in order to determine in-plane epitaxial relationships between the film and the substrate, and/or between layers in the case of multiple films. In this case, a diffraction peak is chosen that is characteristic of each layer/substrate and the sample is rotated around the ϕ axis. An example is given in Figure II-9 in the case of the growth of CeO_2/YSZ/Si.

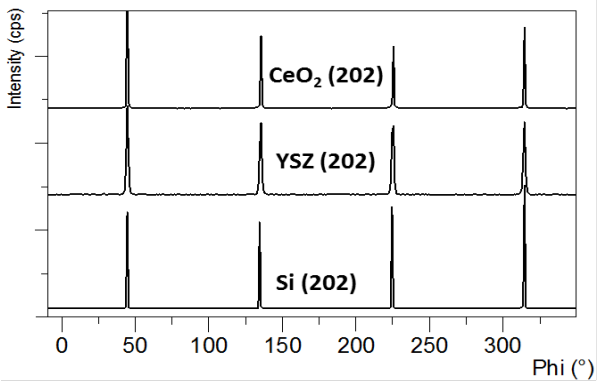

Figure II-9: The ϕ- scans profiles of CeO_2 (202), YSZ (202) and Si (202) reflections

II.2.2 X-ray reflectometry

X-ray reflectometry is a useful method to determine thin film thickness and roughness of the different layers in heterostructures. The principle is based on interference mechanism between X-ray beam reflected at the different interfaces of the stack that exhibit different density. For each layer, there are two interfaces: the lower interface and the upper interface. When the incident beam arrives at an angle less than the critical angle below which there is total reflection, it is completely reflected. As soon as the angle of incidence exceeds the critical angle, some X-ray beam penetrates the layer and, if the thickness is sufficiently thin, arrives at the lower interface on which it is reflected partially or completely. From then on, the beam reflections at two interfaces will interfere that causes oscillations called Kiessig fringes, and its total reflection intensity as a function of the incident angle with respect to the thin film surface captured by the detector. This technique is effective if the thickness of the layers relatively low (50-90 nm) and the roughness is not too high (below one or two nanometers).

Kiessig equation: $d = \frac{\lambda}{2}\sqrt{\frac{m_2^2 - m_1^2}{\theta_2^2 - \theta_1^2}}$ Eq. II-2

Philipps X'Pert Pro diffractometer is used for those measurements. Sample is first aligned so that the substrate is perpendicular to the incident plane. Then a $2\theta - \omega$ scan is performed such as in the case of out of plane diffraction as shown in Figure II-10 for a CeO_2/YSZ bilayer on a silicon substrate. In blue is shown the experimental data and the red curve is the simulated one using the X'Pert Reflectivity software. The period of these Kiessig fringes and the loss of beam intensity provide information of the layer thickness and roughness respectively. One can observe 2 periods from the Kiessig fringes that correspond to the CeO_2, the thinnest film that matches with the largest period, and the YSZ, the thicker film and thus the smallest period.

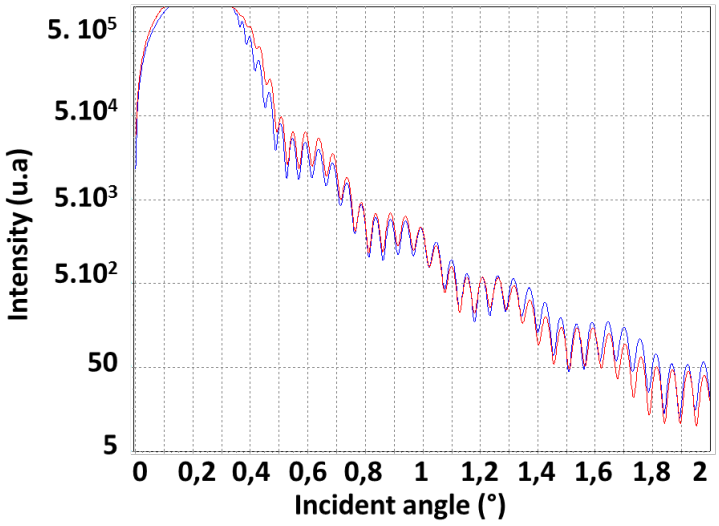

Figure II-10: XRR diagrams of a CeO_2/YSZ bilayer on Si.

II.2.3 Morphological analysis

Atomic Force Microscopy (AFM) is used to analyze the topography of deposited thin films. The AFM consists in a cantilever with a sharp tip at its end which is used to scan over the area of interest on the sample. The displacement of the cantilever due to the interaction between the tip and the surface is recorded by a laser beam that is reflected on the back of the cantilever and directed onto a four-segment photodetector. The difference among signals of each segment gives the lateral/vertical deflections, providing information on the sample topography. AFM can be operated in contact mode, tapping mode or non-contact mode. In the contact mode, the tip applies a force on the sample to analyze that lead to bend the cantilever. The deflection of the cantilever is held constant during the scan to keep constant the force between the tip and the sample by moving either the sample holder, either the tip holder, with an accurate piezoelectric mechanical system. This approach allows fast scanning and good resolution ability but is limited to hard material without mobile parts. The non-contact mode is a regime of AFM in where the tip is placed close to the sample but separated of a short distance (some nms or 10's nm) and the force that applies on the tip is of large range (Van Der Waals, magnetic, electrostatic…). The tip is flying at fixed height and the bending of the cantilever is measured by the four-segment photodetector. This approach is of particular interest for soft materials analysis or advanced AFM variant. An intermediate approach named tapping mode consist in

an intermittent contact between the tip and the surface. The cantilever is excited by an external force, oscillating at the frequency close to its own resonance frequency. Interactions between the sample and the tip affect the cantilever amplitude, frequency, and phase of oscillation that are measured using the four-segment photodetector. In a conventional topographic image, the amplitude of the cantilever oscillation is maintained at a fixed value during the scan. Tapping mode offers a good compromise between topographic resolution and avoiding surface damage but can also provide additional information in the case of perovskite such as the surface termination. The vertical resolution in this equipment is typically in the range of 1/10 nm mostly depending on the experimental setup and the lateral resolution is linked to the tip sharpness and can reach sub-nm scale. Figure II-11 shows the simple working principle of AFM.

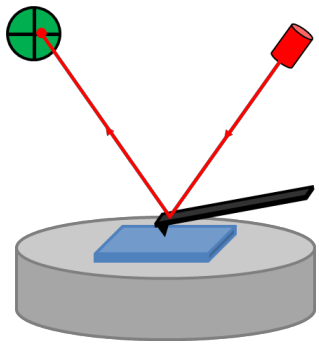

Figure II-11: Basic principle of atomic force microscopy

All samples were measured with an Innova AFM from Bruker Company in contact mode that allows fast scanning and good resolution without altering the sample thanks to the high Young modulus of perovskite oxide materials. In order to avoid contamination of the sample surface, the AFM measurement was performed right after removing from the PLD chamber. Silicon nitride tips were used for contact mode and WsxM software was used for image analysis. In particular, the RMS roughness was used as a good indicator from the film roughness which is calculated as the RMS width of the height histogram of a typical image.

II.3 Electrical characterization techniques for PZT materials

In addition to structural characteristics, ferroelectric properties of as-deposited PZT thin films play a significant role and can be determined by various measurements such as Polarization-Electric filed measurement (P-E loop), leakage current measurement, and capacitance-voltage measurement (C-V). Those techniques were used to characterize the PZT films and make a link between structural and functional properties of the materials.

II.3.1 The polarization hysteresis loop

All parameters such as remnant polarization ($\pm P_r$) or coercive fields (or bias) ($\pm E_C$ or $\pm V_C$) that characterize the ferroelectricity of materials can be obtained from the polarization hysteresis loop (P-E loop). This measurement has been performed on the ferroelectric tester TF Analyzer 1000 (AixACT Germany). Ferroelectric hysteresis loops can be obtained using two different types of techniques: (i) the Dynamic Hysteresis Mode (DHM) and (ii) the Positive Up Negative Down (PUND) method.

In the DHM method, an alternative signal of triangular shape voltage consisting of 4 bipolar signals of frequency $\nu_0$is applied with a delay time 1s (Figure II-12). The first (third) bipolar voltage pulse pre-polarizes the sample in the negative (positive) state. The second (fourth) bipolar voltage pulse measures the hysteresis in the state of negative (positive) polarization. In order to get the complete hysteresis cycle, the second half of pulse 2 and the second half of pulse 4 were taken.

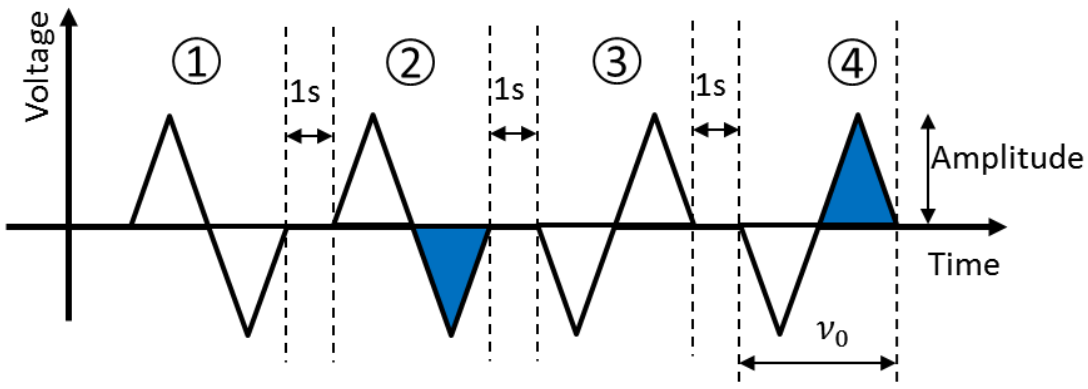

Figure II-12: Voltage pulse applied for DHM

The polarization measurement is an indirect measurement that is converted from the current flowing through the sample under the effect of the applied voltage. The charge Q between two faces of PZT thin film can be obtained from the current integration over time measured during a cycle by the following function:

$$Q = \int I_{(t)} dt \qquad \textbf{Eq. II-3}$$

From this result, the polarization can be deduced by P = Q/A, wherein A is the area of the electrodes.

The measured current was produced by two current contributions: the leakage current $I_{leakage}$ caused by the electrons flowing through the sample and the displacive current I_{DE} [18]:

$$\boldsymbol{I_{measured} = I_{leakage} + I_{DE}} \qquad \textbf{Eq. II-4}$$

I_{DE} it consists in two components: the current I_{FE} is the result of the ferroelectric domain switching and the dielectric current I_{ε} corresponds to the charging current of the capacitor. In particular, the displacive current can be written as follow as a function of the electrical displacement $\overrightarrow{D}$:

$$\boldsymbol{I_{DE} = \frac{\partial}{\partial t}\vec{D} = \frac{\partial}{\partial t}\left(\vec{P} + \varepsilon.\varepsilon_0.\vec{E}\right) = I_{FE} + I_{\varepsilon}} \qquad \textbf{Eq. II-5}$$

In the DHM technique, the measured current contains all of the contributions. It can thus be complicated to use in the case of samples exhibiting too high level of leakage that will tend to hide the polarization switching current.

In the PUND method (Figure II-13), the first pulse is negative and prepolarizes the sample to the negative state. After t_2 period, the second positive pulse (pulse P) sent during $2t_1$ period polarizes the sample and therefore the corresponding current contains the FE and non FE-contribution. While the current during the third (U) only contains the non-FE contributions. By subtraction, the FE contribution can be obtained. The same principle for the fourth (N) and fifth (D) pulses for the negative state. So that the current loop I_{PUND} is obtained from I_P (V)-I_U (V) for the positive voltage and I_N(V)-I_D(V) for the negative voltage.

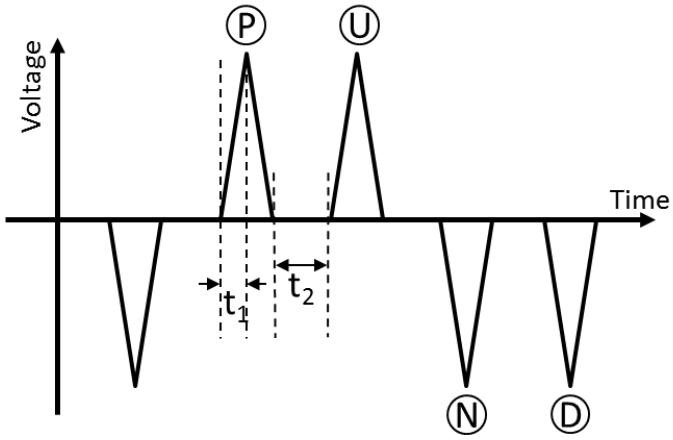

Figure II-13: Voltage pulse profile applied for PUND.

The difference between two methods can be ignored for ferroelectric samples with low losses and high polarization value. However, in the case of samples exhibiting high leakage current level, the PUND method is to be favored as illustrated in Figure II-14.

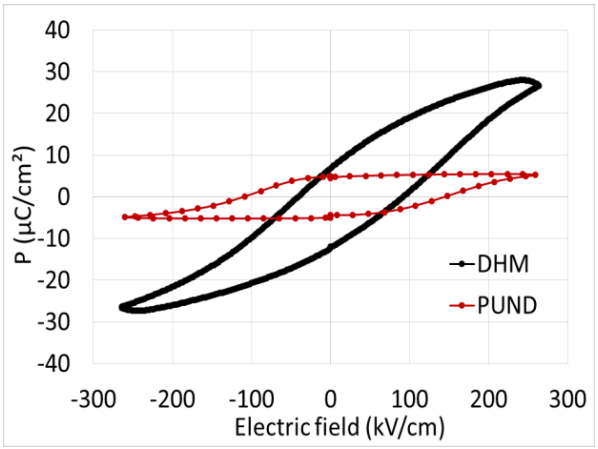

Figure II-14: A typical ferroelectric loops on a PZT thin film obtained using the DHM and PUND methods

II.3.2 Capacitance measurements

The two previous techniques give information about ferroelectric characteristics such as the value of remnant polarization and coercive fields. The modulation of the dielectric constant as a function of the electric field (or bias) also exhibits a particular feature in the case of ferroelectric materials. The capacitance C and the charges Q are electrically linked as follow:

$$C = \frac{\partial \mathrm{Q}}{\partial \mathrm{V}} \text{ with } Q = \mathrm{D} * \mathrm{A} \qquad \textbf{Eq. II-6}$$

A is the area of the capacitor electrode. On the other hand, electrical displacement is defined in Eq. II-5 and by using this definition and knowing that $V = \mathrm{E} * \mathrm{t}$, the relationship becomes:

$$C = \frac{\mathrm{A}}{\mathrm{t}} \frac{\partial \mathrm{D}}{\partial \mathrm{E}} = \frac{\mathrm{A}}{\mathrm{t}} . (\varepsilon . \varepsilon_0 + \frac{\partial \mathrm{P}}{\partial \mathrm{E}}) \qquad \textbf{Eq. II-7}$$

In the case of conventional paraelectric capacitors, the polarization does not depend on the electric field and the capacitance becomes only a function of the geometry of the design and the permittivity of the dielectric material between the electrodes according to the following equation:

$$C = \frac{\varepsilon . \varepsilon_0 . A}{t} \qquad \textbf{Eq. II-8}$$

Here, C is the capacitance in farads [F], ε is the relative dielectric constant of the material between two plates, ε_0 is the dielectric constant in vacuum [$\approx 8.854 \times 10^{-12} F.m^{-1}$], A is the area of overlap of two plates [m^2] and t is the distance between the plates [m]. In the case of ferroelectric capacitor, an additional feature is observed corresponding to the polarization of the dielectric material and that is representative of the ferroelectric properties of the material, in particular the switching polarization.

The capacitance measurement was done by two-point mode using a Keithley 2400 instrument and Hioki 3532-50 LCR HiTester capacitor. A sinusoidal alternating excitation signal of small amplitude (30mV in our case) with frequency f_0 that can be tuned up to 1 MHz (100 kHz was used this work) is sent to the sample. This excitation signal is changed in amplitude and phase as it passes through the sample and the capacitance meter then recovers the signal at the output of the sample and, by comparison with the input signal, deduces the impedance Z and the phase θ of the material between electrodes. From this impedance and phase information, the equipment calculates values of capacity and resistance in the framework of a parallel RC circuit. Figure II-14 displays the P(E) loop recorded at 1kHz and the associated C(V) obtained using the first derivative of the signal. The character noisy of the C(V) measurement relates to numerical method used without any numerical filtering.

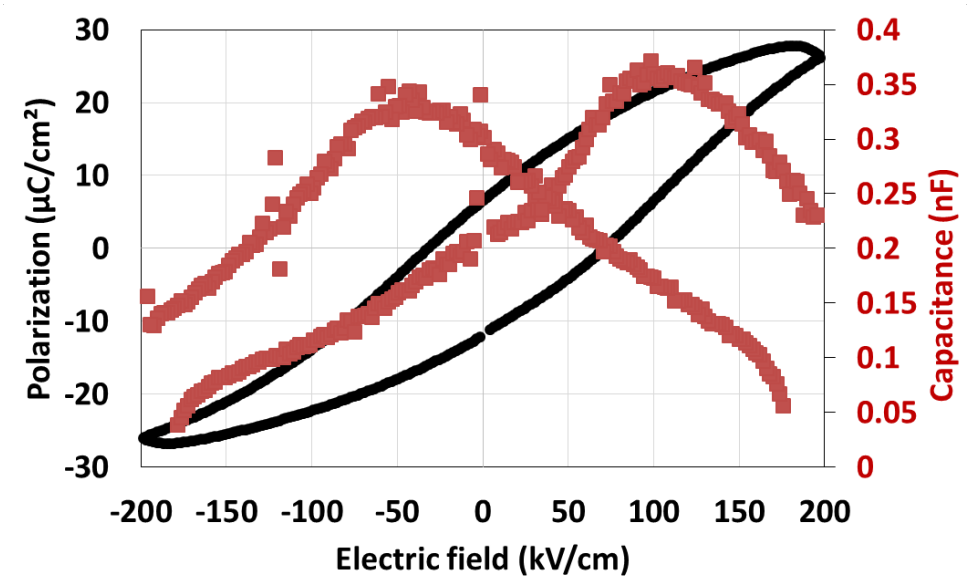

Figure II-15: the typical P(E) measurement (back) of the PZT thin film under the frequency of 1kHz and the C(E) obtained by derivation of the P(E)

II.3.3 Leakage current measurements

Leakage current is also an important parameter which shows the limitation of such materials for device application, in particular for thin films. The leakage current is the main reason for losing energy and influences on the polarization process. Actually, the conducting mechanism in such insulating materials exhibiting structural and stoichiometric defaults are complex and were the subjects of several studies [19]–[21], in particular in our work [22]. Mechanism such as conducting domain walls between ferroelectric domains have been identified in addition to the more conventional mechanisms governed by the interfaces (Schottky, Fowler-Nordeim mechanism,…) [19]–[21], [23] or the volume (Pool-Frenkel, hopping,…) [24]–[26]. The study of the leakage current is a wide subject that requires lot of time and caution. For these reasons, little work was done in this thesis on explaining the origin of this current but instead this information was systematically used as a characteristic of the grown films. The leakage current was obtained by applying by sweeping a DC voltage and measuring the corresponding current using Keithley 2400 Source-Measure Unit (SMU).

II.4 Characterization techniques for magnetostrictive materials

The magnetostrictive thin films grown by sputtering need to be characterized to extract their functional properties that are their magnetization and their magnetostrictive properties. These measurements will allow to evaluate the characteristics of the expected sensor.

II.4.1 Magnetization measurement – Vibrating – sample Magnetometer (VSM)

The magnetometer used in this study is based on the measurement of the magnetic flux induced by a magnetic moment generated by the magnetized sample placed purposely next to a (or several) sensing coil. This bias can be measured directly using a voltmeter or with more accuracy using SQUID [27], [28]. Another approach to improve the sensitivity consist in moving the sample periodically and to measure the derivative of the magnetic flux using a lock-in amplifier to have a better accuracy: such equipment is called a Vibrating Sample Magnetometer (VSM) [29], [30] and is schematically described in Figure II-16.

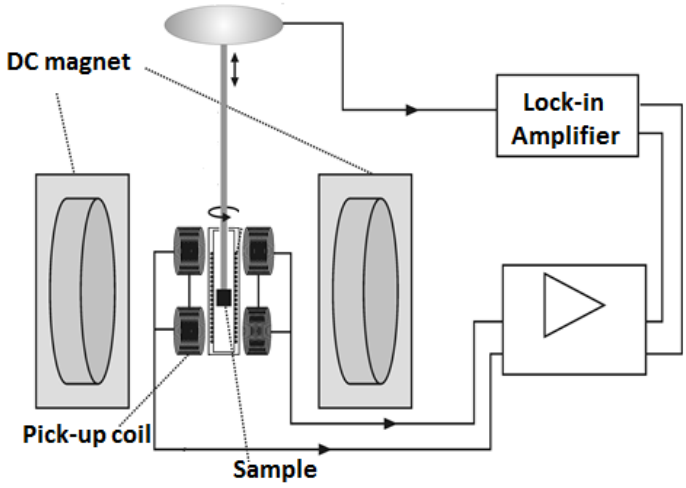

Figure II-16: Diagram of VSM

In the experimental setup, the sample is placed within a uniform magnetic field ***H*** and at the center of a symmetrical two pick-coil system; a magnetic moment ***M*** will be induced in the sample using an external magnetic field. The sample is then moved according a sinusoidal excitation, which lead to a change of the magnetic flux flowing through the coils. This process induces a voltage in the sensing coils that is proportional to the magnetic moment of the sample:

$$V \; \alpha \; 4\pi . N . S_m . M \qquad \text{Eq. II-9}$$

M is the magnetic moment of the samples; N and S_m are the number of turns and the cross-section. The Lakeshore 7404 VSM supplied by the Lakeshore Lab at VNU was used to investigate the magnetic properties of the magnetic materials TbFeCo. The measurements took place at room temperature with the magnetic field in the range of $\pm$ 1 T. Measurements both parallel and perpendicular to the sample surface were carried out to reveal the magnetic anisotropy properties of the samples.

II.4.2 Magnetostriction measurement system for thin film

The magnetostriction factor is determined through a change of the bending of a cantilever using an optical deflection method. This system setup was built and designed at the Laboratory for micro-nano technology in Hanoi [14]. Figure II-17 illustrates the measuring principle of the system that consist in the following main parts:

1. Diode laser emitting a parallel red laser beam with focus of 1.5 mm diameter.
2. 45° full-reflection prism to adjust the laser direction.
3. Sample holder.
4. Reflection mirror oriented 45° with the vertical direction.
5. Photodiode array detector.
6. Electromagnet generating a magnetic field in range of $\pm$ 1 T.

The laser beam strikes the prism under an incident angle condition of full reflection. The beam is reflected on the prism in direction of the sample surface where it is once again reflected in the surface and turns back to the second mirror and goes into the photodiode array detector.

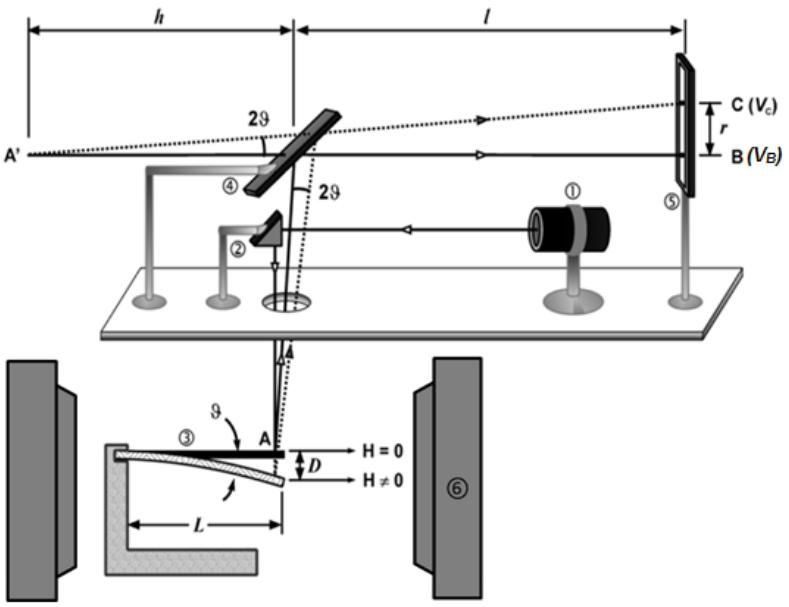

Figure II-17: Schematic of measuring principle of the magnetostriction measurement system for thin films [14]

The position B and C on the detector corresponds to the beam position with or without the magnetic field. The difference in the output voltage related to the deflection r in the detector is expressed as follow:

$$\boldsymbol{r = k(V_C - V_B)} \qquad \text{Eq. II-10}$$

k is the conversion factor which describes the difference in the output voltage per distance unit (V/mm). From the deflective distance r, the deflective angle ϑ is extracted using the relationship:

$$\boldsymbol{tan(2\vartheta) = \frac{r}{h + l}} \qquad \text{Eq. II-11}$$

h and l are the distance from the upper mirror to the sample and to the detector, respectively. In our case, $h + l = 188.5\ cm$. Due to a very small value of the deflective angle ϑ, $\tan(2\vartheta)$ is approximated to 2ϑ. Therefore, the magneto-elastic coefficient is expressed by:

$$b = \frac{E_S}{3(1+\upsilon_S)} \cdot \frac{\vartheta}{L} \frac{t_S^2}{t_f} = \frac{E_S}{6(1+\upsilon_S)} \cdot \frac{r}{L(h+l)} \cdot \frac{t_S^2}{t_f} \quad \text{Eq. II-12}$$

Here, L is the sample length, t is the thickness, E is Young's modulus. f and s denote for film and substrate, respectively. The magnetostriction coefficient is deduced from the magneto-elastic coefficient:

$$\lambda = \frac{b(1+\nu_f)}{E_f} = \frac{1}{6} \cdot \frac{E_S(1+\upsilon_f)}{E_f(1+\upsilon_S)} \cdot \frac{r}{L(h+l)} \cdot \frac{t_S^2}{t_f} = r\frac{A}{Lt_f} \quad \text{Eq. II-13}$$

With A is a constant that only depends on the mechanical and geometrical parameters of the film and substrate. In order to evaluate the magnetostriction coefficient of TbFeCo, a thin film of TbFeCo was deposited on a glass substrate and used for this analysis. Young modulus and Poisson coefficient have been taken from the literature ($E_S = 72GPa$, $\upsilon_S = 0.21$ [42], $E_f = 80GPa$, $\upsilon_f = 0.31$) and considering the substrate thickness $t_S = 0.01\ mm$, the value of $A = 8.62 \times 10^{-7} mm$.

II.5 Interferometric profiler

Interferometric profiler was used to determine the deformation of the cantilever under an external DC electric field or the static behavior of the cantilever. Under an external DC electric field, the PZT cantilever generates the strain that leads to a bending moment. The deflection of the cantilever was used to evaluate the d_{31} coefficient of the PZT thin film integrated into a device. Interferometric profilometer is an interference microscope which working principle is shown in Figure II-18a. The light (monochromatic or white) beam is split into two paths, half of the beam passes through the focal plane of a microscope objective to the sample to be analyzed, while the other half is reflected from a reference mirror. When the 2 beams recombined after reflection, constructive or destructive interferences occur that change as a function of the height profile of the sample. This phenomenon results in the dark and bright bands known as interference fringes. A 3D map of the sample is constructed by scanning the sample in height to obtain interference fringes on all the sample. Even if the lateral resolution is limited by the resolution of the optical microscope and thus the wavelength of the used light, the vertical resolution can reach 1 nm when slow scanning is performed.

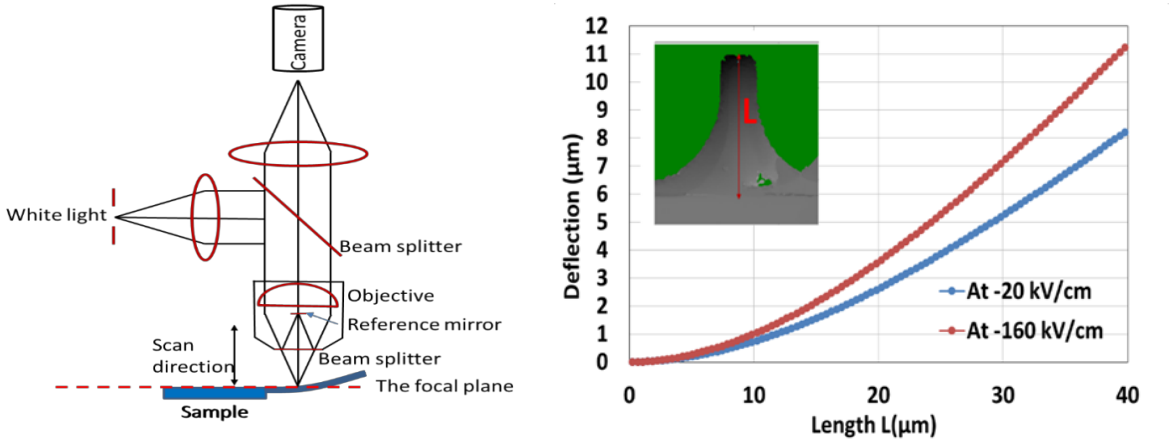

(a) (b)

Figure II-18: Optical profiler to determine the initial bending shape and static deformation of cantilever under an external DC electric field (a) and Profile of the cantilever (b)

A typical 3D map of a free-standing PZT cantilever is shown in Figure II-18b. Without applying a bias voltage, the initial bending of the cantilever due to the initial stress is determined, and this measurement was carried on right after micro-fabrication process. Then, the device is polarized and the evolution of the bending is measured. Fitting the profile of the cantilever is a way to extract the d_{31} coefficient, as will be discussed in Chapter 4.

II.6 Resonance measurement

In static operation, a continuous external stress applied to the cantilever by applying a bias that leads to change its deflection that is detected by profilometer method. This approach allows to extract information about the film and the processed device. This is relevant to extract preliminary information about the device characteristics but the final objective of this work is to use the device under dynamic operation. It is thus aimed to take advantage of the high quality PZT cantilever as a resonant micro-sensor for sensing magnetic field based on magnetoelectric effect. The application of magnetic field to a high ME coefficient material will transfer stress to the PZT cantilever and induce a shift in resonant frequency. The first step was thus to measure the frequency dependence of the impedance of the cantilever of the PZT cantilever itself to evaluate the expected performances.

When an AC driving voltage is applied to the electrodes, the PZT cantilever will extend or contract in the plane, thus creating an alternating stress. This vibrating mode is called d_{31} mode. The resonance phenomenon occurs when the frequency of applied field equals to one of the natural resonant frequencies of the cantilever. At this frequency, the loss of energy is higher inducing an increasing of the device impedance and a phase shifting. These characterizations were performed by a commercial impedance analyzer Hioki IM3570 but also by a homemade setup based on lock'in measurement. Those characterization setups will be detailed in Chapter IV but a fast overview on the home-built system is given, as described in Figure II-19. An alternative excitation bias (controlled by a Keithley 3390) is sent to a load resistor in series with the device under test and the alternative terminal voltage is measured at the same frequency using a lock-in amplifier RS844. A LabVIEW program was developed to control the input signal applied to the sample and to record data concluding output voltage and phase from the lock-in amplifier.

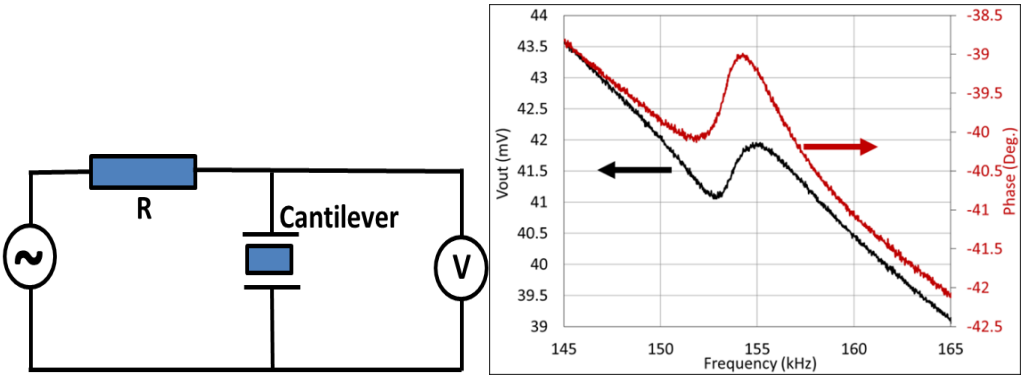

Figure II-19: Experimental setup and a typical measurement of the output voltage and phase angle from the SRO-based PZT cantilever

The frequency is swept and the impedance is measured. A peak in impedance and a change in phase is representative of a resonant frequency, as shown in Figure II-19. Determination of this parameter allows evaluating of the applicability of PZT thin film for micro application such as a resonator, energy harvesters. It also allowed us to evaluate some physical characteristics of the material, by comparison with calculated results.

II.7 The magneto-electric measurement

The magneto-electric measurement is the final characteristic to evaluate the ability of device for the magnetic sensing application. The experimental setup is presented in Figure II-20a. The device is placed between two poles of an electromagnet up to 1 Tesla. A static stress (σ_{DC}) induced from the magnetostrictive materials (TbFeCo) under DC external magnetic field H_{DC} is transferred to the PZT layer. A change in DC magnetic field leads to a change in the stress the magnetic film transferred to the PZT layer. An exciting AC bias superimposed with a DC voltage at frequency around the resonant frequency of the device is applied to electrodes of the device by using the impedance analyzer Hioki IM3570. The DC bias, in this case, is to control the polling direction of the PZT layer while the AC bias causes the alternating stress.

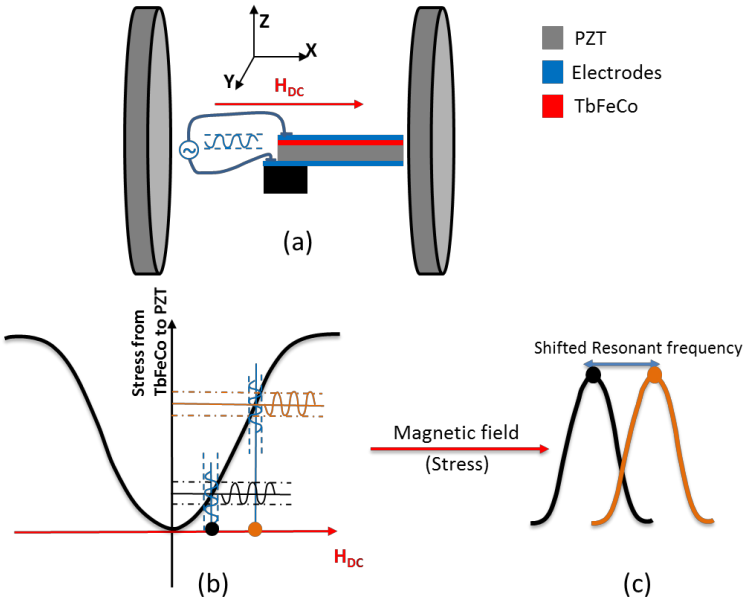

Figure II-20: The experimental setup for the magneto-electric measurement

The total output signal from the device V_d is the sum of the alternative voltage V_{ac} and the DC voltage V_{DC}: $V_d = V_{ac} + V_{DC}$. V_{ac} comes from the exciting AC bias while V_{DC} comes from the static stress due to the direct piezoelectric effect. A shift of resonant frequency is expected, which can be also recorded by an impedance analyzer Hioki IM3570. For magnetic sensing applications, this frequency shift Δ_{sh} is a signature of the magnetic change which can be calculated from the equation $\Delta_{sh} = k.H_{DC}$. Here k is the conversion factor that characterizes the sensor. The higher the k factor is, the higher is the frequency shift with the magnetic field.

In the traditional measurement of the ME effect [31], [32] a DC external magnetic field is applied that also causes the deformation in the magnetostrictive material. This deformation, in this case, is observed as a bending distortion that generates a constant stress (σ_{DC}). The presence of this stress, due to the mechanical coupling between them, will make on the opposite faces of the piezoelectric layer a constant charge Q_{DC}. The piezoelectric layer acts as a capacitor with an ineligible amount of charge, which is rapidly degraded after a time constant (τ) due to the discharge phenomenon when connected to the device. In order to maintain this amount of charge, in experimental measurements, an alternating magnetic field hac (h_{ac}) is used to generate oscillating stresses (σ_{ac}) on the piezoelectric phase. The presence of this stress produces a variable voltage (q_{ac}) on the piezoelectric plate and the measurement can be made by measuring the alternating output voltage on the piezoelectric layer. In comparison to the traditional method, no need of solenoid coil in measurement method of the shift of the resonant frequency makes it simpler for micro design.

References

[1] Z. Zhu, J.-F. Li, F. Lai, Y. Zhen, Y. Lin, C. Nan, L. Li, and J. Li, "Phase structure of epitaxial Pb(Zr,Ti)O3 thin films on Nb-doped SrTiO3 substrates," *Appl. Phys. Lett.*, vol. 91, p. 222910, 2007.

[2] D. Ambika, V. Kumar, H. Imai, and I. Kanno, "Sol-gel deposition and piezoelectric properties of {110}-oriented Pb(Zr0.52Ti0.48)O3 thin films," *Appl. Phys. Lett.*, vol. 96, p. 031909, 2010.

[3] M. D. Nguyen, "Characterization of epitaxial Pb(Zr,Ti)O3 thin films deposited by pulsed laser deposition on silicon cantilevers," *J. Micromech.Microeng*, vol. 20, p. 085022, 2010.

[4] T. Ohnishi, T. Yamamoto, S. Meguro, H. Koinuma, and M. Lippmaa, "Pulsed laser ablation and deposition of complex oxides," *J. Phys. Conf. Ser.*, vol. 59, pp. 514–519, 2007.

[5] C. Chirila, A. G. Boni, I. Pasuk, R. Negrea, L. Trupina, G. Le Rhun, S. Yin, B. Vilquin, I. Pintilie, and L. Pintilie, "Comparison between the ferroelectric/electric properties of the PbZr0.52Ti0.48O3 films grown on Si (100) and on STO (100) substrates," *J. Mater. Sci.*, vol. 50, pp. 3883–3894, 2015.

[6] M. Schreiter, R. Gabl, D. Pitzer, R. Primig, and W. Wersing, "Electro-acoustic hysteresis behaviour of PZT thin film bulk acoustic resonators," *J. Eur. Ceram. Soc.*, vol. 24, pp. 1589–1592, 2004.

[7] D. B. Chrisey and G. K. Hubler, Eds., *Pulsed Laser Deposition of Thin Films*. John Wiley & Sons Inc., 1994.

[8] Esteve D., "Développement d'une technique de caractérisation optique appliquée au suivi in situ de la croissance d 'oxydes fonctionnels par ablation laser pulsé," Université Paris Sud 11.

[9] R. Eason, Ed., *Pulsed Laser Deposition Of Thin Films: Applications Led-Growth Of Functional Materials*, WILEY-INTE. Optoelectronics Research Centre University of Southampton, UK, 2007.

[10] S. Schmidt, Y. W. Ok, D. O. Klenov, J. Lu, S. P. Keane, and S. Stemmer, "Microstructure of epitaxial SrTiO3/Pt/Ti/sapphire heterostructures," *J. Mater. Res.*, vol. 20, no. 9, pp. 2261–2265, 2005.

[11] G. Panomsuwan, O. Takai, and N. Saito, "Orientation control of textured SrTiO3 thin films on platinized α-Al2O3 (0 0 0 1) by an ion beam sputter deposition method," *J. Phys. D. Appl. Phys.*, vol. 45, p. 494003, 2012.

[12] D. O. Klenov, T. R. Taylor, and S. Stemmer, "SrTiO3 films on platinized (0001) Al2O3: Characterization of texture and nonstoichiometry accommodation," *J. Mater. Res.*, vol. 19, no. 5, pp. 1477–1486, 2004.

[13] S. Chakraverty, A. Ohtomo, M. Okude, K. Ueno, and M. Kawasaki, "Epitaxial structure of (001)- and (111)-oriented perovskite ferrate films grown by pulsed-laser deposition," *Cryst. Growth Des.*, vol. 10, pp. 1725–1729, 2010.

[14] D. T. Huong Giang, "Elaboration and study of giant magnetostrictice single layer and

multilayer fims based on TbFeCo compound," Uviversite de Rouen and Vietnam national university, Hanoi, 2005.

[15] N. H. Duc, "Development of giant low-field magnetostriction in a-TerfecoHan-based single layer, multilayer and sandwich films," *J. Magn. Magn. Mater.*, vol. 242–245, pp. 1411–1417, 2002.

[16] N. H. Duc, K. Mackay, J. Betz, and D. Givord, "Giant magnetostriction in amorphous (Tb1−xDyx)(Fe0.45Co0.55)y films," *J. Appl. Phys.*, vol. 79, no. 2, pp. 973–977, 1996.

[17] W. H. Bragg and W. L. Bragg, "The Reflection of X-rays by Crystals," *Proc. R. Soc. Lond. A*, vol. 88, pp. 428–438, 1913.

[18] I. Fina, L. Fábrega, E. Langenberg, X. Mart, F. Sánchez, M. Varela, and J. Fontcuberta, "Nonferroelectric contributions to the hysteresis cycles in manganite thin films: A comparative study of measurement techniques," *J. Appl. Phys.*, vol. 109, p. 074105, 2011.

[19] L. Pintilie, I. Vrejoiu, D. Hesse, G. LeRhun, and M. Alexe, "Ferroelectric polarization-leakage current relation in high quality epitaxial Pb (Zr,Ti) O3 films," *Phys. Rev. B*, vol. 75, p. 104103, 2007.

[20] P. Zubko, D. J. Jung, and J. F. Scott, "Electrical characterization of PbZr0.4Ti0.6O3 capacitors," *J. Appl. Phys.*, vol. 100, p. 114113, 2006.

[21] M. Dawber, K. M. Rabe, and J. F. Scott, "Physics of thin- lm ferroelectric oxides," *Rev. Mod. Phys.*, vol. 77, pp. 1083–1130, 2005.

[22] C. Jégou, "Integration d'un film mince de Pb (Zr , Ti) O dans une structure capacitive pour applications RF," Université Paris Sud 11, 2014.

[23] M. Lallart, Ed., *Ferroelectrics - Applications*. Janeza Trdine 9, 51000 Rijeka, Croatia, 2011.

[24] M. T. Chentir, E. Bouyssou, L. Ventura, and C. Anceau, "Leakage current evolution versus dielectric thickness in lead zirconate titanate thin film capacitors," *J. Appl. Phys.*, vol. 105, p. 061605, 2009.

[25] J. F. Scott, C. A. Araujo, B. M. Melnick, L. D. McMillan, and R. Zuleeg, "Quantitative measurement of space-charge effects in lead zirconate-titanate memories," *J. Appl. Phys.*, vol. 70, no. 1, pp. 382–388, 1991.

[26] B. Nagaraj, S. Aggarwal, T. K. Song, T. Sawhney, and R. Ramesh, "Leakage current mechanisms in lead-based thin-film ferroelectric capacitors," *Phys. Rev. B*, vol. 59, no. 24, pp. 16022–16027, 1999.

[27] N. M. Aimon, D. Hun Kim, H. Kyoon Choi, and C. a. Ross, "Deposition of epitaxial BiFeO3/CoFe2O4 nanocomposites on (001) SrTiO3 by combinatorial pulsed laser deposition," *Appl. Phys. Lett.*, vol. 100, p. 092901, 2012.

[28] J. Li, I. Levin, J. Slutsker, V. Provenzano, P. K. Schenck, R. Ramesh, J. Ouyang, and A. L. Roytburd, "Self-assembled multiferroic nanostructures in the Co Fe 2 O 4 -PbTi O 3 system," *Appl. Phys. Lett.*, vol. 87, p. 072909, 2005.

[29] J. Zhang, P. Li, Y. Wen, W. He, A. Yang, and C. Lu, "Shear-mode self-biased magnetostrictive/piezoelectric laminate multiferroic heterostructures for magnetic field

detecting and energy harvesting," *Sensors Actuators, A Phys.*, vol. 214, pp. 149–155, 2014.

[30] M. Liu, O. Obi, J. Lou, Y. Chen, Z. Cai, S. Stoute, M. Espanol, M. Lew, X. Situ, K. S. Ziemer, V. G. Harris, and N. X. Sun, "Giant electric field tuning of magnetic properties in multiferroic ferrite/ferroelectric heterostructures," *Adv. Funct. Mater.*, vol. 19, no. 11, pp. 1826–1831, 2009.

[31] M. Q. Le, F. Belhora, A. Cornogolub, P. J. Cottinet, L. Lebrun, and A. Hajjaji, "Enhanced magnetoelectric effect for flexible current sensor applications," *J. Appl. Phys.*, vol. 115, p. 194103, 2014.

[32] S. Marauska, R. Jahns, H. Greve, E. Quandt, R. Knöchel, and B. Wagner, "MEMS magnetic field sensor based on magnetoelectric composites," *J. Micromechanics Microengineering*, vol. 22, p. 065024, 2012.

Chapter III– Piezoelectric and magnetostrictive thin films on silicon

In a ME micro-sensor, the piezoelectric thin film plays the important role of converting the strain from the magnetic layer into an electrical signal. Therefore, the integration of epitaxial $Pb(Zr_{0.52}Ti_{0.48})O_3$ (PZT) thin films with high quality on silicon substrates has been considered as the first main step for making micro-devices. This chapter presents the PZT thin films obtained in this work on Si(001), after growth by PLD with the use of oxide buffer layers. The resulting properties of the films, including structural, ferroelectric, and dielectric characterizations, are determined as a function of crystalline orientation, for (001)- and (110)-oriented PZT thin films. Finally, the growth and magnetic properties of TbFeCo films are presented to close this chapter.

Outline:

III.1 Introduction

The perovskite oxide integration on silicon has been studied extensively in the last couple decades and achieved positive results [1][2]. The growth strategy is based on the use of multiple oxide buffer layers, first to obtain an epitaxial growth on silicon with its native amorphous oxide, second to adapt the unit cell to allow for perovskite oxide epitaxy. YSZ can grow directly through the reduction of the native ultrathin silicon oxide on the Si substrate surface [3][4], and acts as the seed layer for epitaxial growth of following layers. CeO_2 is then used to realize the cube-on-cube alignment on YSZ thin film that ease the deposition of perovskite-oxide layers [1][2]. When a high-quality perovskite-buffered silicon substrate is obtained, epitaxial growth of other perovskite oxides is facilitated. The full growth process is presented in Figure III-1.

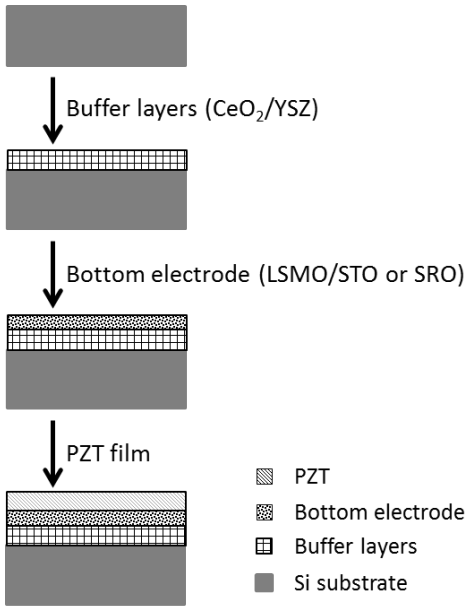

Figure III-1: Fabrication process of epitaxial PZT thin films on silicon by PLD

Ferroelectric properties are generally better for epitaxial PZT films than for polycrystalline ones [5]. The polarization is maximum in the direction perpendicular to the substrate surface for (001)-oriented PZT films, while the polarization is smaller for (110)-oriented PZT films as it is rotated 45° with respect to the substrate surface. In this framework, the epitaxial orientation of PZT layers will be controlled by using different conductive perovskite layers $SrRuO_3$ (SRO) or $La_{0.7}Sr_{0.3}MnO_3$ (LSMO) as bottom electrode. Two kinds of electrodes have been used to

control the epitaxial orientation of PZT thin films, namely $La_{0.7}Sr_{0.3}MnO_3$(LSMO)/$SrTiO_3$ (LSMO-based PZT thin films) and $SrRuO_3$ (SRO) (SRO-based PZT thin films).

To avoid the contamination of the Si surface with Pb from the PZT target, the critical step of YSZ growth at low pressure (10^{-6} Torr) has to be performed prior to any use of the PZT target. Therefore, the PZT deposition process on Si substrate is split into two steps:

(i) The first step is the growth of CeO_2/YSZ. This process consists of steps in the following order: heating up to the deposition temperature (730 °C), cleaning of YSZ and CeO_2 targets, depositing the films, annealing the sample under 75 Torr of oxygen, and cooling down to room temperature to prepare for the next step.

(ii) The second step is the growth of the other materials (PZT/ SRO or PZT/LSMO/STO). This process consists of steps in the following order: Heating up to the deposition temperature (640°C), cleaning of relevant targets including PZT, depositing the films, annealing the sample under 300 Torr of oxygen, and cooling down to room temperature.

The effect of growth conditions on thin-film structure and ferroelectric properties of PZT will be presented more in details in the following sections.

III.2 Growth of double-buffer layer CeO_2/YSZ on silicon substrates

Due to the limited size of the ablation plasma or plume, the deposition is uniform only over a limited area on the substrate, in the order of 1 cm^2 at best. This is why all Si substrates used in the thesis were cut down to 5×5 mm^2. The (001)-oriented Si substrates are cleaned in acetone and ethanol by an ultrasonic cleaner without removing the native silicon oxide SiO_2, and then glued with silver paint onto the heater surface to get a good thermal contact.

In order to avoid a further growth of SiO_2, the Si substrate is heated up to the YSZ deposition temperature (730°C) at a pressure of 10^{-4} Torr. The target-substrate distance is fixed at 5 cm by the PLD setup. The laser energy per pulse is systematically measured by a calorimeter before each deposition, and the laser fluence adjusted, taking into account the transmission losses over the optical path. The area of the laser spot on the target is 1.2 mm^2 for YSZ and 1.8 mm^2 for CeO_2.

Deposition of YSZ takes place at the temperature of 730°C and is a two-steps process [3][4]. The first step is done at low pressure around $3x10^{-6}$ Torr without oxygen introduced into the growth chamber to consume the native SiO_2 layer as explained in chapter 1. After 400 laser pulses, oxygen is introduced up to a pressure of $2.2x10^{-4}$ Torr for the second step and YSZ epitaxial growth on Si carries on. The 10 nm-thick CeO_2 layer is grown right after at the same pressure of $2.2x10^{-4}$ Torr and the same temperature of 730 °C. L. Méchin et al. [1] reported that 10 nm thickness for CeO_2 exhibited the best results in terms of crystalline quality: below this value, the film is not homogeneous and above it the CeO_2 layer roughness increases and affects the properties of the following layers. CeO_2 grows cube-on-cube on YSZ with a larger lattice parameter (0.541 nm), and allows for the lowering of the lattice mismatch with perovskite oxide layers, the latter having their unit cell rotated by 45° with respect to CeO_2 one [1][6]. Finally, an annealing is done under 75 Torr oxygen at 730 °C for 1 h. **Table III-1** summarizes the PLD parameters for YSZ and CeO_2 thin film growth.

	Pressure (Torr)	Temperature (°C)	Freq. (Hz)	Fluence (J/cm^2)	Deposition rate (nm/pulse)
YSZ	3×10^{-6} (No O_2)	730	4	2.7	
YSZ	2.2×10^{-4}	730	4	2.7	0.020
CeO_2	2.2×10^{-4}	730	2	2.7	0.040

Table III-1: PLD parameters for YSZ and CeO_2 growth

Crystallographic properties and surface quality of the as-deposited films were routinely investigated by XRD and AFM. From 2theta-Omega scan (Figure III-2), the epitaxial relationship (001)CeO_2 ‖ (001)YSZ ‖ (001)Si is confirmed. The out-of-plane lattice parameters were determined as 5.16 Å and 5.43 Å for YSZ and CeO_2, respectively. A comparison with the bulk lattice parameters of 5.14 Å in YSZ and 5.41 Å in CeO_2 is in agreement with the fact that

both films are fully relaxed on silicon, as demonstrated in a previous study [6]. The (002) YSZ rocking curve shows 0.76° Full Width at Half-Maximum (FWHM). The CeO_2 films have a smooth surface with a root mean square roughness (R_{rms}) of 0.2 nm over a $2 \times 2\ \mu m^2$ area as revealed by AFM.

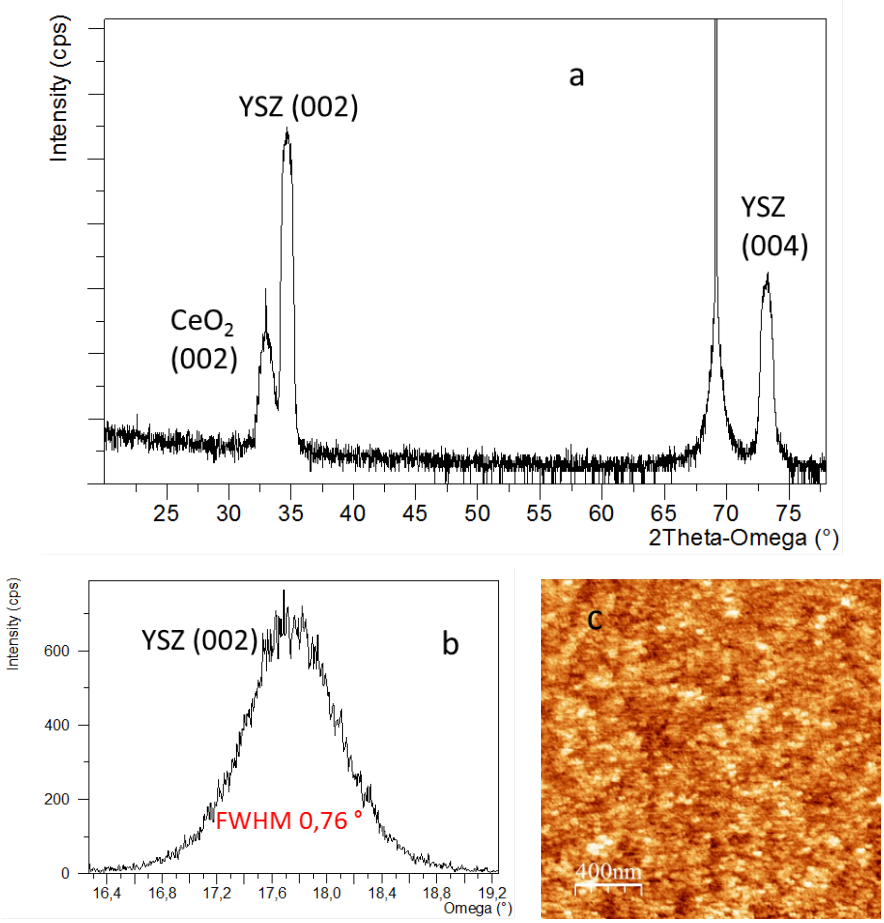

Figure III-2: (a) 2Theta-Omega scan of CeO_2/YSZ double layer on Si substrate. CeO_2 (002), YSZ (002) and YSZ (004) peaks are indicated. (b) The (002) YSZ rocking curve. (c) Typical AFM image of the surface of a CeO_2 layer on YSZ/Si, roughness R_{rms} = 0.2 nm.

The thicknesses of the YSZ and CeO_2 films can readily be determined by XRR as shown in Figure III-3. From the thickness values extracted by this technique, the deposition rates by PLD for YSZ and CeO_2 under the conditions as shown in Figure III-3 are 0.02 nm/pulse and 0.04 nm/pulse, respectively.

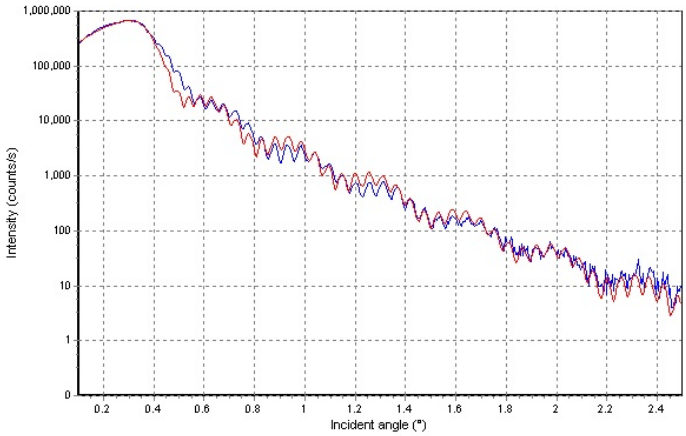

Figure III-3: XRR curve from a CeO_2/YSZ double layer on Si substrate. Fitted thickness/roughness (rms) are: 66.2 nm/0.5 nm YSZ and 12.2 nm/0.5 nm CeO_2, with a 1 nm/0.8 nm SiO_2 layer at the YSZ/Silicon interface [6].

The in-plane epitaxial relationships between the Si substrate and the buffer layers were revealed by the ϕ- scans of CeO2 (202), YSZ (202) and Si (202) reflections as shown in Figure III-4. The result shows the coincidence of the (202) peaks of CeO_2 and YSZ with those of the silicon, which demonstrates the epitaxial relationship: [100] CeO_2 ‖ [100] YSZ ‖ [100] Si.

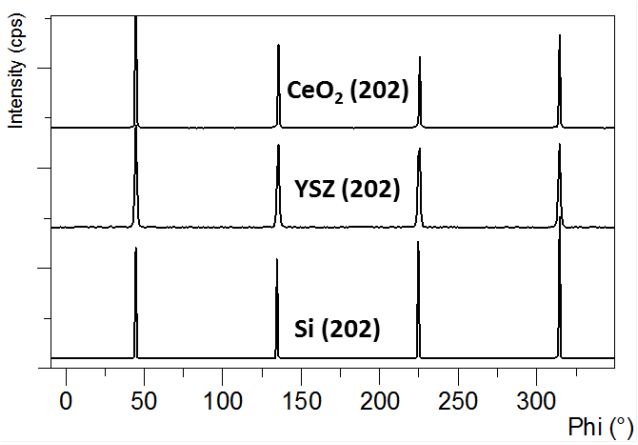

Figure III-4: The ϕ- scans of CeO_2 (202), YSZ (202) and Si (202) reflections.

Being the first buffer layer to be deposited on Si, YSZ plays a critical role as seed layer for the growth of other layers. Several thicknesses between 45 nm and 115 nm were tested to find the optimal one in terms of crystallographic quality (see Figure III-5). When the thickness of YSZ is 45 nm, values of FWHM and R_{rms} are 1.09 ° and 0.2 nm (from AFM image, not shown),

respectively. A slightly lower FWHM (0.76 °) is obtained for the thicker films, both 80 nm and 115 nm, while keeping the same low roughness. A thickness of 80 nm was thus chosen in this work, as a not too thick YSZ layer is preferred for micro-fabrication.

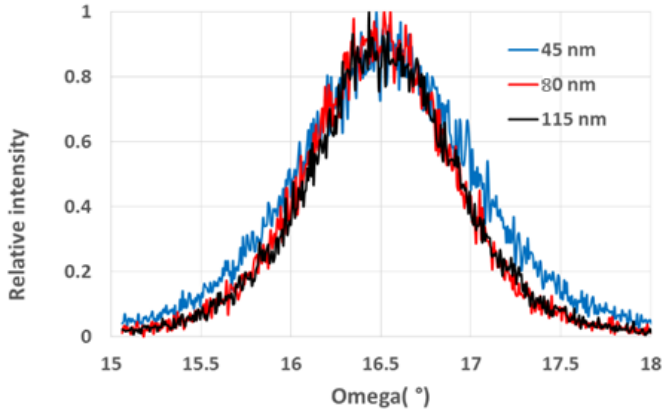

Figure III-5: Rocking curves of YSZ (002) peak for three different film thicknesses.

From here on, CeO_2 (10 nm)/YSZ (80 nm)/Si will be used as the pseudo-substrate for the subsequent growth of perovskite oxide layers.

III.3 Control of the orientation of epitaxial PZT with bottom electrode

As the piezoelectric properties of a PZT thin film depend on its crystallographic orientation, the control of the latter has significant implications for device operation. It is therefore a desirable tool in the framework of this work.

As an example, in the case of voltage-controlled MRAM devices based on the converse piezoelectric effect, the application of voltage to the piezoelectric material generates a bi-axial strain which is transferred to the adjoining magnetic structure [7][8][9]. The in-plane anisotropy then plays a critical role regarding the generated strain: for (001)-oriented PZT (polarization along z-axis), the magnitude and sign of the bi-axial strain along the in-plane crystallographic directions [100] and [010] are the same $\varepsilon_{xx} = \varepsilon_{yy} = d_{31}E_z$, with E_z the applied out-of-plane electric field and d_{31} the transverse piezoelectric constant (d_{33} along [001]). On the other hand, for (110)-oriented PZT, the same applied electric field generates two different strains along the two in-plane crystallographic directions [001] and [-110]: $\varepsilon_{xx} =$

$\frac{(d_{31}+d_{33})E_Z}{2\sqrt{2}}$ and $\varepsilon_{yy} = d_{31}E_Z/\sqrt{2}$. The strain transfer towards the magnetic material is thus markedly different depending on PZT orientation.

III.3.1 LSMO-based PZT thin films

III.3.1.a The effect of substrate temperature on the growth of PZT

Starting from the parameters optimized for PLD-grown PZT on STO substrates [10], in particular regarding gas pressure and laser fluence, the substrate temperature has been tuned for all perovskite oxides growth (STO, LSMO, PZT) on CeO_2/YSZ-buffered Si. First a double layer 10 nm-thick STO/ 40 nm-thick LSMO is deposited, followed by the growth of 150 nm-thick PZT. The oxygen pressure is 0.12 Torr for STO and LSMO, while 0.12 Torr of nitrogen protoxide (N_2O) is employed for PZT. The deposition temperature was varied from 580 to 640°C, and the resulting XRD data is presented in Figure III-6.

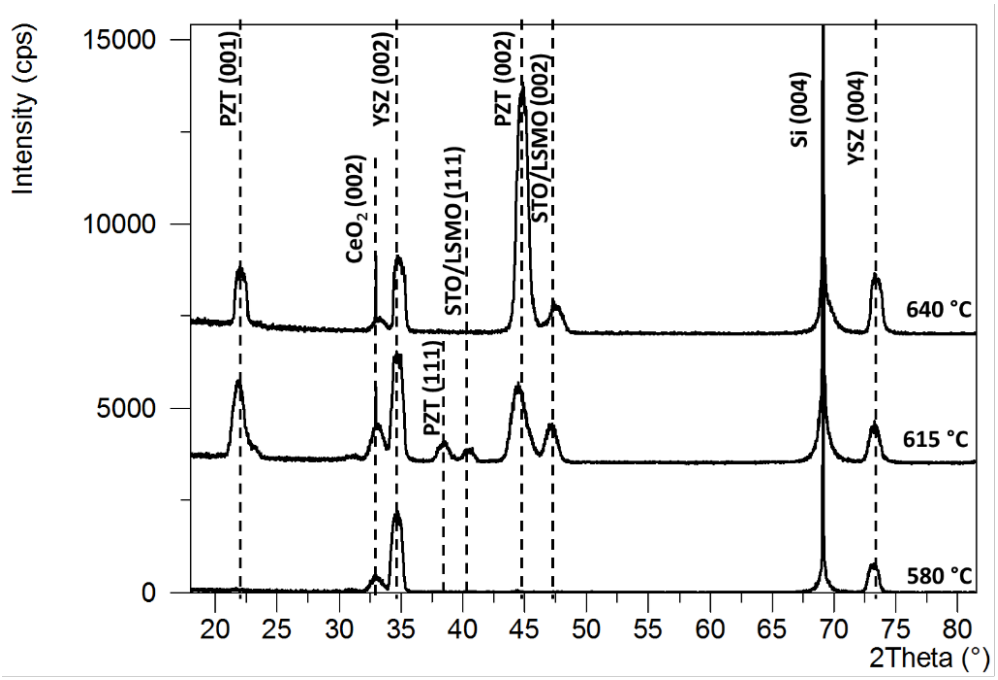

Figure III-6: XRD diagrams of PZT films grown on LSMO (40 nm)/STO (10 nm) buffered CeO_2 (10 nm)/YSZ (80 nm)/Si at three different growth temperatures.

At 580°C no perovskite oxide layer is detected, indicative of the fact that higher temperatures are needed on CeO_2/YSZ buffer than on STO single crystal, due to the absence of a perovskite seed layer in the former. Perovskite phase nucleation is observed above 600°C,

with the best film in terms of XRD peak intensity obtained at 640°C. Even using N_2O gas which allows for higher temperatures than O_2 due to more oxidizing of N_2O than O_2, going above this temperature is detrimental for the Pb content of PZT,

After deposition, an annealing under 300 Torr of oxygen is performed for 1 h in the PLD chamber. This annealing allows for incorporation of oxygen into the oxide layers. The optimized deposition parameters for STO, LSMO, and PZT are summarized in **Table III-2**.

	Pressure (Torr)	Temperature (°C)	Freq. (Hz)	Energy Density (J/cm^2)	Deposition rate (nm/pulse)
STO	1.2×10^{-1}	640	4	2.7	0.024
LSMO	1.2×10^{-1}	640	2	2.3	0.027
PZT	1.2×10^{-1} (N_2O)	640	4	2.7	0.025

Table III-2: PLD parameters for STO, LSMO and PZT growth

III.3.1.b The effect of STO buffer layer on epitaxial orientation of PZT

Figure III-7 shows the XRD diagrams of the PZT thin films on LSMO/STO buffered CeO_2/YSZ/Si substrates with two thicknesses of STO, 10 and 50 nm. A thicker STO film is detrimental for the (001)-orientation, as the 50 nm-thick STO film is mostly (111)-oriented and so is the PZT film, together with a small (001)-oriented component. A single (111) orientation could not be obtained for PZT in the framework of this work as no high quality, single-orientation STO layer could be grown above 10 nm thickness. Nevertheless, a 10 nm-thick (001)-oriented STO film allows for the growth of nice (001)-oriented PZT films.

The (001)-oriented STO is preferred to the other orientation due to only 2.5% difference in the in-plane mismatch between CeO_2 and STO if STO is rotated 45° to each other, which seems

to be true for the thin thickness of STO. When increasing the thickness of STO, the mismatch probably increase that leads to polycrystalline structure. Another reason can be because of low diffraction density of (111) orientation for perovskite (such as STO, PZT), that makes it difficult to see at 10nm-thick STO. Moreover, a quite large peak of phi-scan the STO on CeO_2 exhibits a columnar growth (see Figure II-9) can lead to some different orientation at the boundary, in this case the (111) orientation.

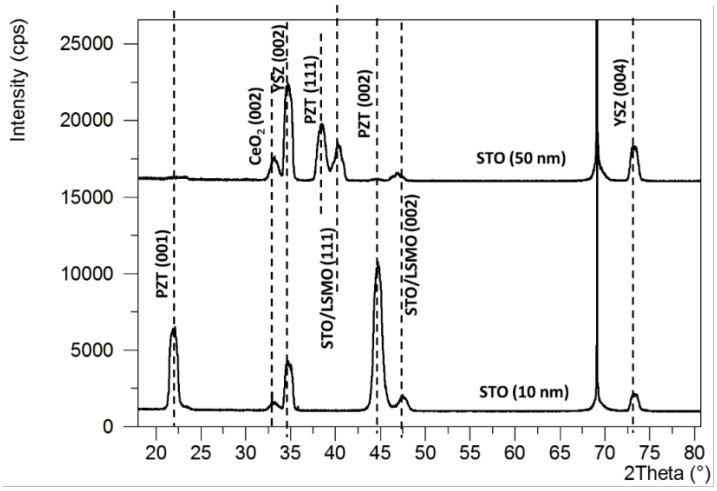

Figure III-7:XRD diagram of PZT films grown on LSMO/STO buffered CeO_2/YSZ/Si with two different thicknesses of STO

III.3.1.c The effect of PZT thickness on the structural properties

In order to investigate the effect of the PZT thickness on the structural properties, samples with various PZT thicknesses have been prepared under the same deposition conditions, while the thickness of LSMO and STO are fixed at 40 nm and 10 nm, respectively.

There is no change of c parameter of PZT with the thickness. A change of relative proportion of (001) is due to going from (001) at 150 nm of PZT to (110) at 200 nm of PZT, but it is difficult to be quantitative because of the different x-ray intensity among orientations.

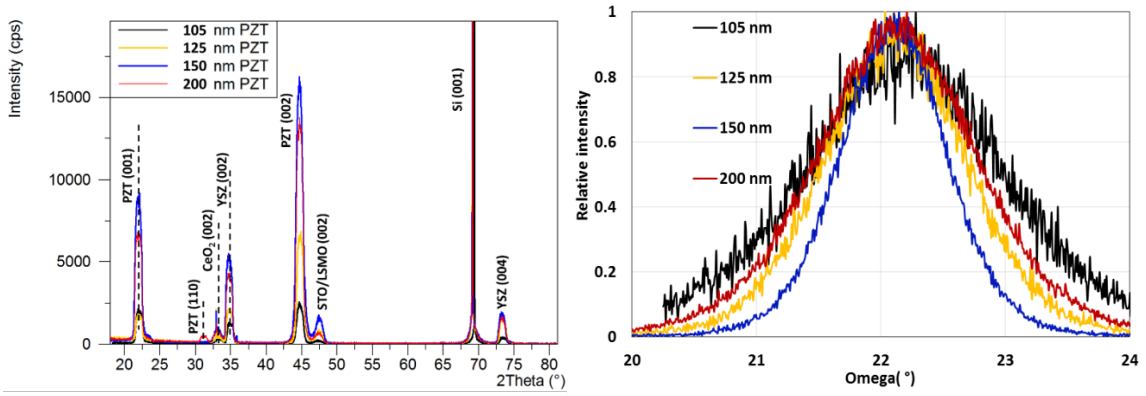

Figure III-8: (Left) XRD diagrams of PZT thin films grown on LSMO (40 nm)/STO (10 nm) buffered CeO_2 (10 nm)/YSZ (80 nm)/Si with different thicknesses. (Right) Rocking curves of the PZT(002) diffraction peak for these films.

Figure III-8 shows the XRD patterns and rocking curves of these films. The XRD results indicate that a single (001) orientation of PZT can only be maintained up to 150 nm thickness. For the 200 nm-thick film, a (110)-oriented component appears, with a corresponding drop of the (001) signal.

III.3.1.d Optimized (001)-oriented PZT

After the various optimizations, all perovskite layers are deposited at 640°C: first a 10 nm-thick STO layer followed by the 40 nm-thick LSMO conductive electrode and a 150 nm-thick, (001)-oriented PZT film. AFM image of the resulting PZT surface topography is displayed in Figure III-9, exhibiting a moderate roughness R_{rms} = 2.2 nm with few dots and distributed holes at the sub-100 nm scale. From the previous studies [6], the morphology checked using TEM cross section shows a columnar growth, with (001)-oriented PZT grains of ~100 nm lateral size, which was also observed in this study

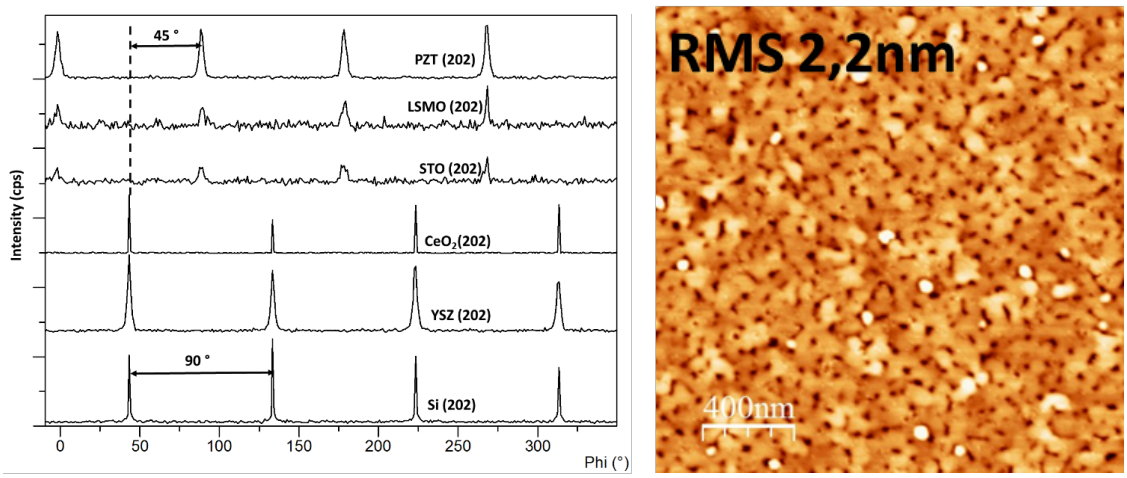

Figure III-9: (Left) Φ-scan profiles of YSZ (202), CeO_2 (202), STO (202), LSMO (202), and PZT (202). (Right) Typical AFM image of (001)-oriented PZT surface

The in-plane epitaxial relationship between the Si substrate and the oxide layers was established by Φ-scans (see Figure III-9) of YSZ (202), CeO_2 (202), STO (202), LSMO (202), and PZT (202). The rotation angle of the (202) peak of YSZ and CeO_2 coincides with that of silicon. This indicates that the cube-on-cube orientation relationship with substrate was obtained for both YSZ and CeO_2. Meanwhile, the scans show the expected 45° shift of the STO (202), LSMO (202) and PZT (202) reflections with respect to the Si (202) reflections with a fourfold rotational symmetry.

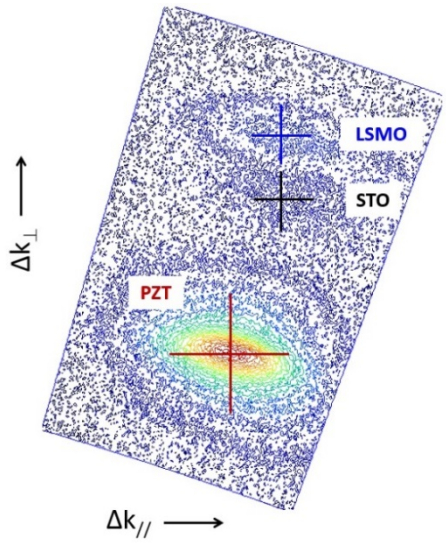

Figure III-10: Reciprocal space map around STO(103) Bragg peak of a 150 nm-thick (001)PZT thin film on LSMO/STO/CeO_2/YSZ/Si

Figure III-10 shows the X-Ray reciprocal space map (RSM) around the (103) reflection of a 150 nm-thick PZT thin film deposited on LSMO/STO/CeO_2/YSZ/Si. Diffraction spots from the (103) planes of PZT, LSMO and STO are visible, while the non-perovskite oxides are left out. The Si(113) peak was measured separately to serve as reference and correct the sample misalignment. The lattice parameters extracted from the RSM in Figure III-10 are summarized in **Table III-3**.

Layer	Thickness (nm)	Lattice parameter (nm)	
		Out-of-Plane	In-plane
STO	10	0.390	0.393
LSMO	40	0.383	0.393
PZT	150	0.406	0.402

Table III-3: Lattice parameters of STO, LSMO and PZT layers

As evidenced in a previous study, the STO films on CeO2/YSZ have an expanded in-plane lattice constant (0.393 nm)compared to the bulk parameter (0.3905 nm), indicative of a relaxed but defective layer, probably oxygen-depleted [6]. The LSMO layer is fully strained on the STO layer, while the PZT layer is relaxed with a reduced tetragonality (c/a = 1.01) compared to the one measured for films grown on single crystalline STO substrates [11].

III.3.2 SRO-based PZT thin films

On a CeO_2/YSZ-buffered Si substrate, in order to promote the (110) orientation for PZT a 40 nm-thick SRO layer is deposited instead of the LSMO/STO double layer presented in the previous part.

III.3.2.a Optimized (110)-oriented PZT

With the growth parameters reported in **Table III-4**, SRO films on CeO_2/YSZ-buffered Si are (110)-oriented but with a slightly reduced crystalline quality compared to the (001)-oriented LSMO/STO double layer, as will be shown below.

	Pressure (Torr)	Temperature (°C)	Freq. (Hz)	Energy Density (J/cm²)	Deposition rate (nm/pulse)
SRO	1.2×10^{-1}	640	4	2.7	0.020
PZT	1.2×10^{-1}	640	4	2.7	0.025

Table III-4: PLD parameters for SRO and PZT growth

Figure III-11 shows the $\theta - 2\theta$ XRD diagrams of the as-deposited SRO-based PZT thin films with thicknesses between 100 nm and 200 nm. Note that the 150 nm-thick film has been measured with a new X-Ray tube and therefore greatly enhanced intensity. It is not possible to normalize the intensity of the substrate due to alignment sensitivity of Si. This does not change the observation of polycrystalline grains at higher thickness.

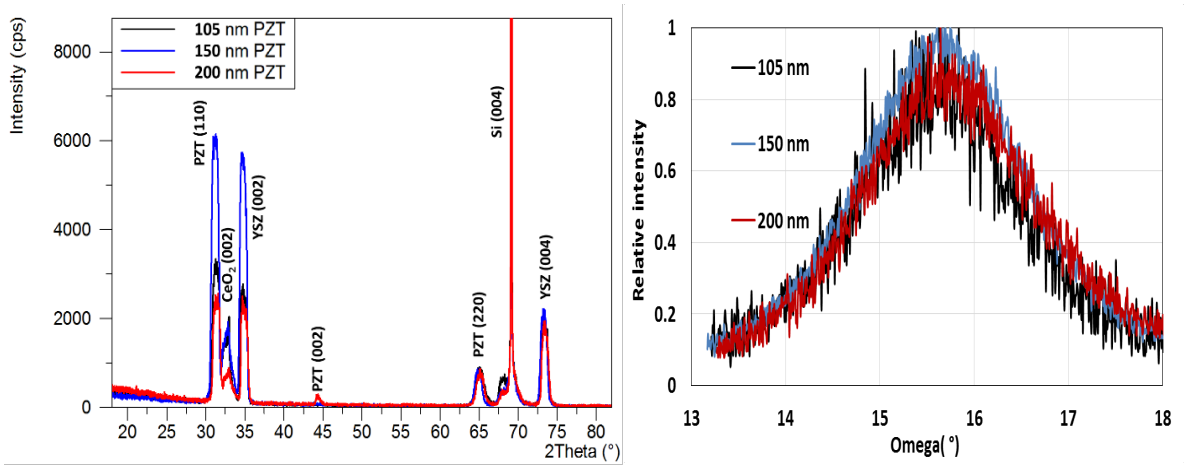

Figure III-11: (Left) XRD diagrams of PZT films on SRO (40 nm)-buffered CeO_2 (10 nm)/YSZ (80 nm)/Si with several thicknesses. (Right) Rocking curves of PZT(220) peak.

As noted for PZT growth on the LSMO/STO double layer, the single-orientation is thus lost above 150 nm thickness, with a transition towards polycrystalline, competitive grain growth driven by the different facet energies and growth rates. This is consistent with a columnar microstructure and almost fully relaxed PZT layer as shown for the LSMO-based

PZT case. In this picture, PZT growth on SRO is very similar, apart from a different orientation constraint at the bottom. Indeed, the surface morphology of (110)-oriented PZT is even rougher than for (001)-oriented PZT, with a higher mosaicity of the (110) grains as shown in Figure III-12.

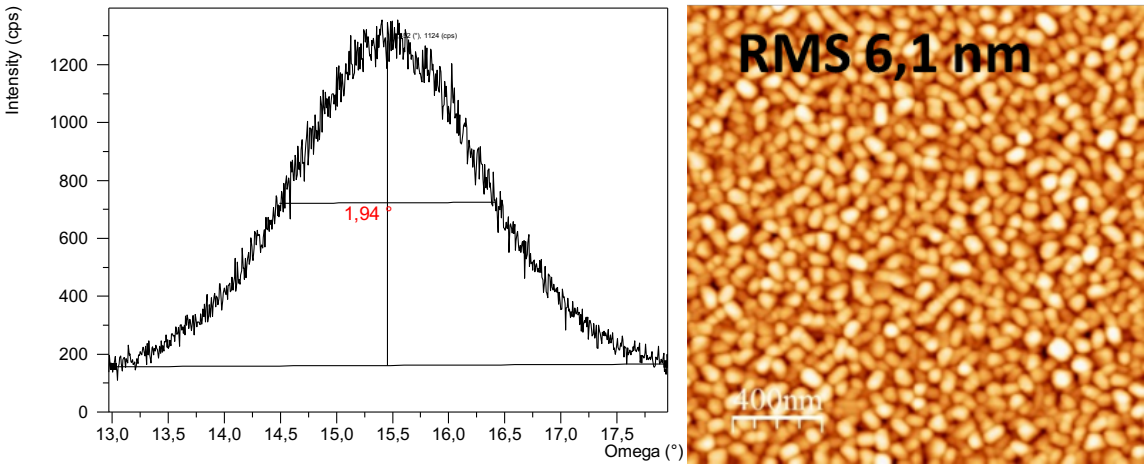

Figure III-12: (Left) Rocking curve for the (220) peak of a 150 nm-thick PZT film on SRO electrode. (Right) Typical AFM image of (110)-oriented PZT, roughness R_{rms} = 6 nm.

III.4 Ferroelectric and dielectric properties of PZT thin films

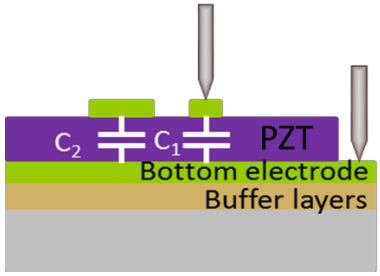

Figure III-13: Parallel-plate capacitor geometry for PZT thin films

In addition to structural parameters, electrical properties of as-deposited PZT thin films play a significant role and have been determined by combined measurements of ferroelectric hysteresis loops (P-V), leakage currents (I-V), and capacitance-voltage (C-V) characteristics. In order to apply an electric field to the PZT layer, a classical parallel-plate capacitor structure

is used. The PZT capacitors are comprised of the 40 nm-thick LSMO or SRO layer working as the bottom electrode and a 200 nm-thick top Platinum (Pt) electrode, as shown in Figure III-13.

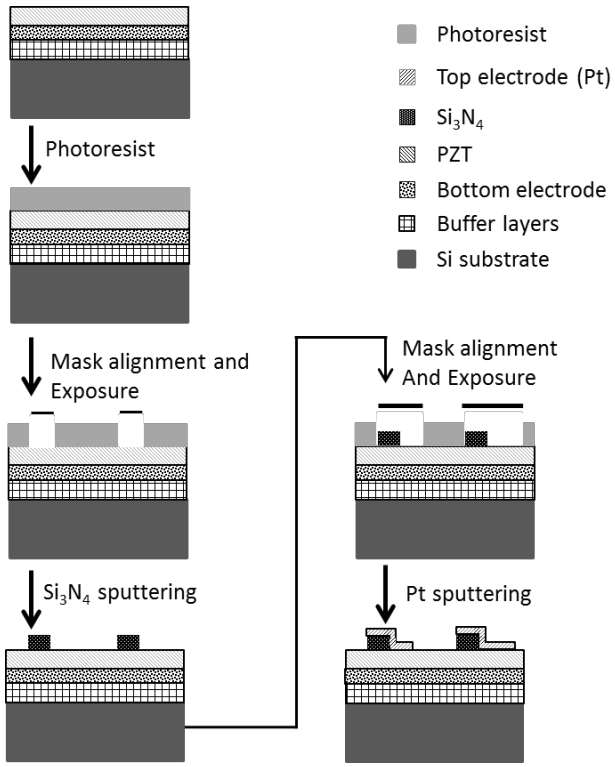

Figure III-14: Process flow for the fabrication of Pt top electrodes

The size of the capacitor is defined by the size of the Pt top electrode, with 3 different areas of 20µm×20µm, 30µm×30µm and 50µm×50µm. In order to be able to contact each capacitor with micro-probes, 200µm×200 µm Pt contact pads were defined with a 200 nm thick Si_3N_4 layer to insulate them from the PZT. Top electrodes were fabricated by sputtering deposition and lithography (lift-off technique), as depicted in Figure III-14.

III.4.1 The effect of measuring conditions on the ferroelectric properties

In this part, the electrical properties of (001)- and (110)-oriented PZT are systematically compared, depending on measurement conditions. The exact layer structures are: 125 nm-thick PZT/LSMO(40 nm)/STO(10 nm)/CeO_2(10 nm)/YSZ(80 nm)/Si for (001) orientation and 105 nm-thick PZT/SRO (40 nm)/CeO_2(10 nm)/YSZ(80 nm)/Si for (110) orientation.

III.4.1.a Electrode area

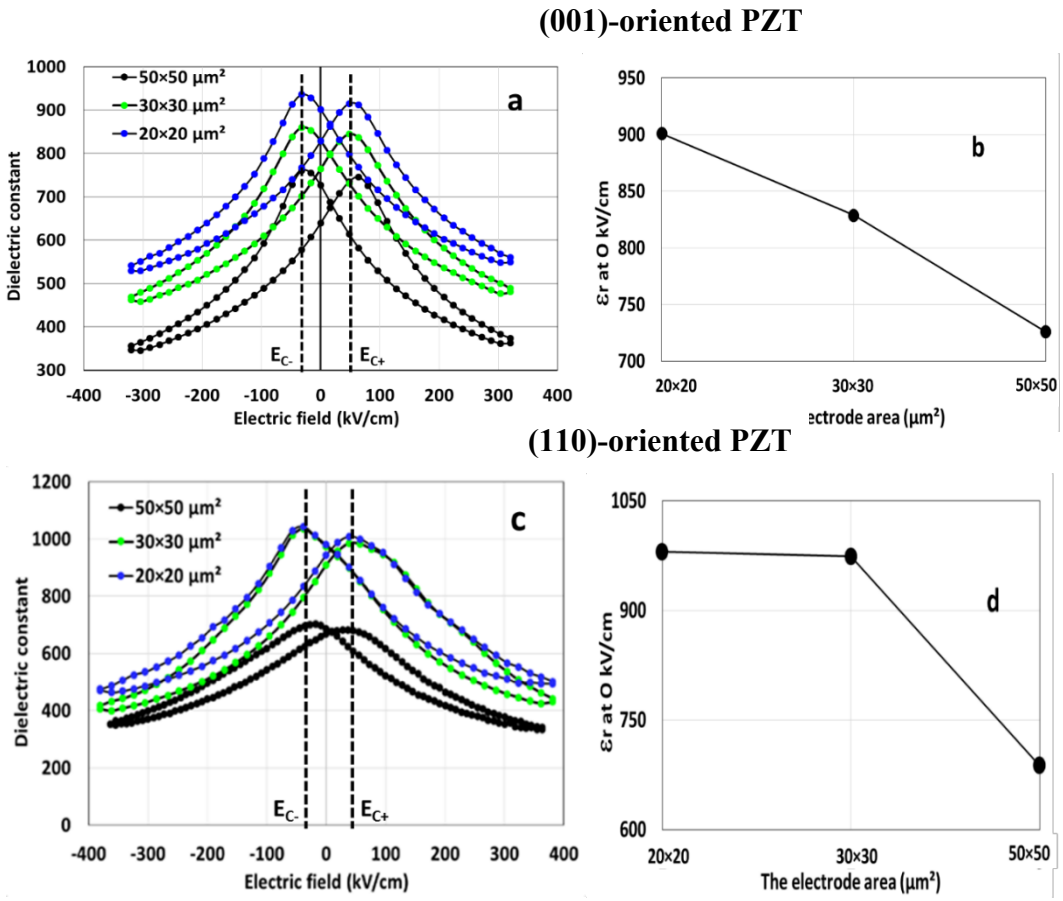

Figure III-15: (a) ε-E curves vs. Electric field (100 kHz AC frequency) and (b) Dielectric constant at 0 kV/cm of (001)-oriented PZT. (c) ε-E curves vs. Electric field (100 kHz AC frequency) and (d) dielectric constant at 0 kV/cm of (110)-oriented PZT.

The dependence of the dielectric constant on top electrode area is shown in Figure III-15 for both PZT orientations, exhibiting the same behavior: (i) A coercive field (E_c) value independent of the size of top electrode; (ii) Curves shifted towards the positive voltage side ($|E_c^+| > |E_c^-|$), with $E_c^+ = 48$ kV/cm, $E_c^- = -32$ kV/cm for (001)-oriented PZT and $E_c^+ = 36$ kV/cm, $E_c^- = -27$ kV/cm for the (110)-oriented PZT; (iii) Increased dielectric constant upon decreasing the electrode area. Asymmetry of the curve may be attributed to the internal electric field induced by asymmetry top and bottom electrode, where the work function of the top electrode Pt higher compared to the bottom electrode SRO.

The dielectric constant is calculated from the capacitance measurements by using the planar capacitor function eq. II-8. This relationship neglects the lateral spill-out of the electric field at the edge of the electrode. For small size of capacitor, it should be taken into account and the Palmer's equation [12] gives an estimation of this effect:

$$C = \frac{\varepsilon_0 \varepsilon_r WL}{d}\left(1 + \frac{d}{\pi W}\left(1 + \ln\left(\frac{2\pi W}{d}\right)\right)\right)\left(1 + \frac{d}{\pi L}\left(1 + \ln\left(\frac{2\pi L}{d}\right)\right)\right) \qquad \textbf{Eq. III-1}$$

Here, W and L are the electrode dimensions, W=L=20, 30 or 50 µm. **Table III-5** shows the dielectric constant (at 0 kV/cm) calculated with and without the "spill-out" correction from Eq. III-1 for different electrode areas. Neglecting the spill-out effect, according to Palmer's function, gives less than 4% error. In other words, this effect can be neglected and Eq. II-8 was used to get the dielectric constant from the capacitance (Figure III-15).

Top electrode area	(001)-oriented PZT			(110)-oriented PZT		
	Raw (F) (Eq. II-8)	Corrected (F) (Eq. III-1)	Difference (%)	Raw (F) (Eq. II-8)	Corrected (F) (Eq. III-1)	Difference (%)
20µm×20µm	900	873	3.2	1243	1210	2.7
30µm×30µm	829	811	2.2	1232	1209	1.9
50µm×50µm	729	719	1.4	836	826	1.2

Table III-5: Dielectric constant from Eq. II-8 vs. Eq. III-1 for different electrode areas

The increased dielectric constant at smaller electrode area (see Figure III-15) can thus not be accounted for at this stage. Further measurements especially at different AC excitation frequencies are needed to elucidate this peculiar behavior.

III.4.1.b Maximum applied electric field

Figure III-16 shows the dielectric constant and remnant polarization (P_r) dependence of PZT thin films on the maximum applied electric field. The dielectric constant (at 100 kHz)

hysteresis curves are independent of the maximum applied electric field for both orientations of PZT. On the ferroelectric side, the P_r value is found to decrease slightly from 16 µC/cm^2 to 10 µC/cm^2 with increasing maximum applied electric field from 240 kV/cm to 400 kV/cm for (001)-oriented PZT. This is at variance with the scenario observed for (110)-oriented PZT, for which the remnant polarization P_r increases from 7 to 12 µC/cm^2 upon increasing the electric field from 240 kV/cm to 315 kV/cm.

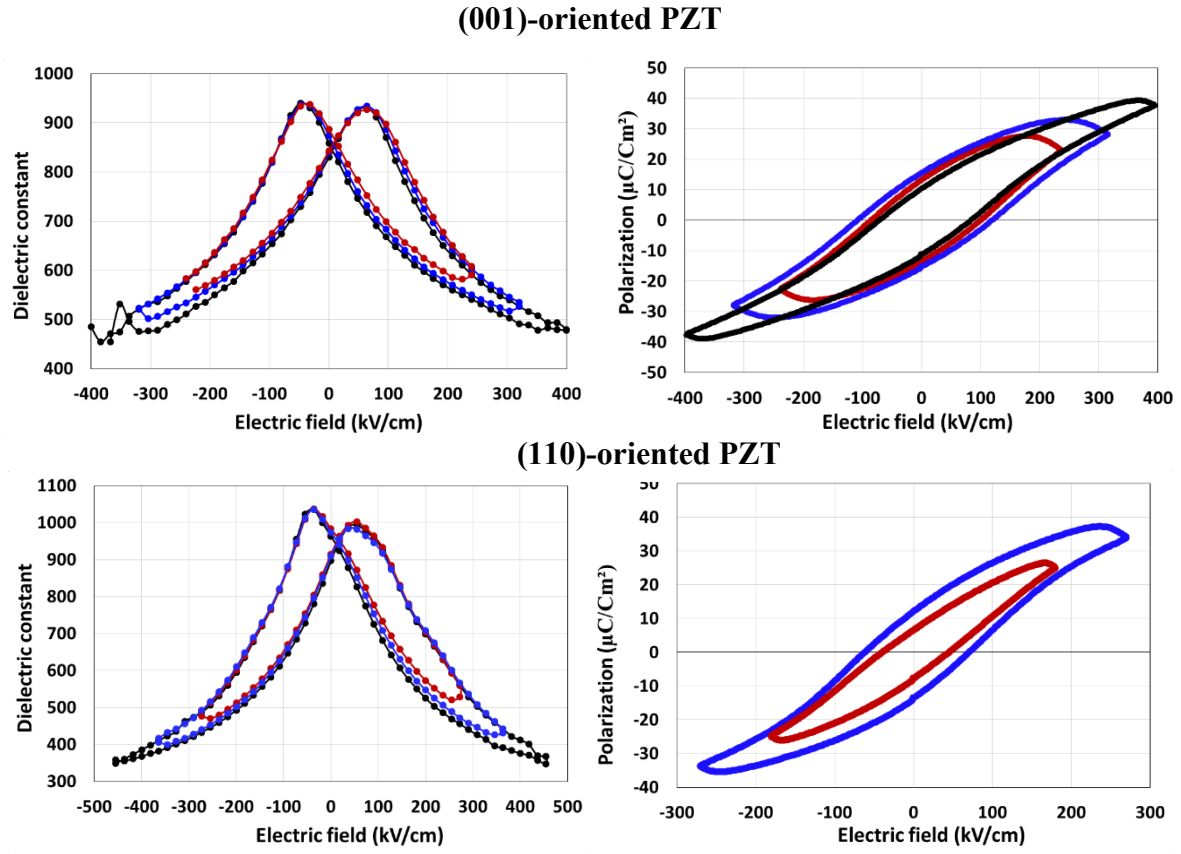

Figure III-16: (a) Dielectric constant (100 kHz) and (b) Polarization hysteresis loops of (001)-oriented PZT capacitors. (c) Dielectric constant (100 kHz) and (d) Polarization hysteresis loops of (110)-oriented PZT capacitors. Top electrode: 20µm× 20µm.

The smaller value of P_r for the (110)-oriented film compared to the (001)-oriented one is expected as the polarization is at 45° from the applied electric field direction. The same goes for the increase of P_r with increasing maximum applied field, but then in the case of (001)-oriented film the opposite effect hints at a diminishing contribution of leakage currents with poling field.

The more asymmetry of the dielectric constant curve for the (110) orientation can come from the different morphology of the interface.

III.4.1.c Excitation frequency

Upon varying the excitation (AC) frequency for capacitance measurement, the frequency dependence of the dielectric constant can be ascertained, at least in the 10 kHz-1 MHz range depending on measuring equipment. For PZT-based applications, the operating frequency is an important parameter related to device design, affecting the dielectric properties of the ferroelectric layer and thus the output signal.

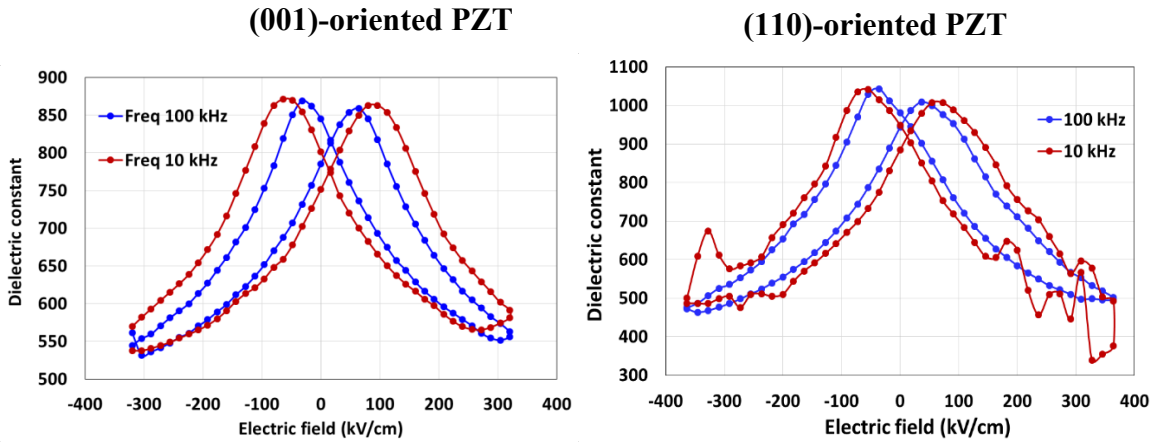

Figure III-17: (Left) Dielectric constant of (001)-oriented PZT as a function of AC frequency. (Right) Dielectric constant of (110)-oriented PZT as a function of AC frequency. Top electrode: 30µm× 30µm.

Figure III-17 shows the frequency dependence of the dielectric constant for both orientations of PZT thin films. A reduction in coercive field with an increase of the frequency is observed for both (001)- and (110)-oriented PZT. It can be explained by the increasing resistance for domain wall motion with increasing frequency [13]. The reduction in coercive field is important for sensor applications, as it can allow for a reduction of the device consumption.

III.4.2 The dependence of dielectric properties on PZT thickness

The thickness dependence of the dielectric constant for the PZT thin films using different bottom electrodes is shown in Figure III-18. The dielectric constant (at 100 kHz) is modified when the PZT thickness varies. First, the shift of the ε-E curves along the electric field axis, that is, the so-called imprint electric field, is thickness-dependent: The imprint field decreases for increasing thickness, as expected.

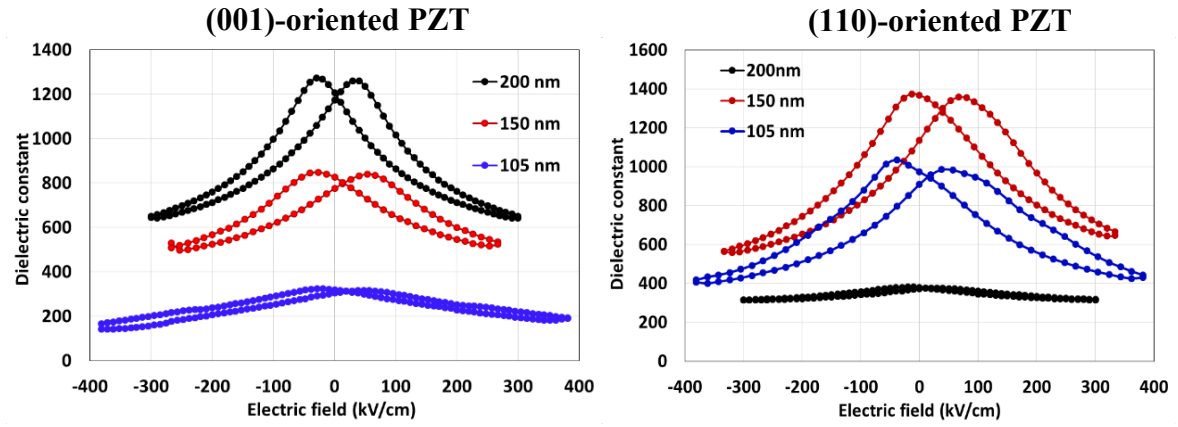

Figure III-18: Dielectric constant of (001)-oriented PZT (left) and (110)-oriented PZT (right) as a function of PZT thickness. Top electrode: 30 µm×30 µm.

The dielectric constant ε_r at 0 kV/cm increases with increasing thickness for the (001)-oriented PZT film, while no clear trend can be extracted for the (110)-oriented PZT film. An increase of the dielectric constant with thickness is generally expected, as going from thin film to bulk sample it increases by a factor ~10. Moreover, for polycrystalline or columnar films, grain size is another parameter that affects the dielectric constant. Grain size increases with thickness, leading to an increase of dielectric constant. This thickness effect is certainly there for both (001)- and (110)-oriented PZT films. Concerning the latter, to explain the observed drop of dielectric constant at 200 nm thickness, many reasons can be invoked [14][15]. In brief the film detailed microstructure and strain state must both be considered making it difficult to get a clear picture.

III.5 PZT for devices

The optimized PZT films integrated on Si substrate for PZT cantilever devices are here presented with a summary of their crystallographic, dielectric, ferroelectric and leakage current properties.

The full layer structures are as follows:

(i) (001)-orientation: PZT(150 nm) / LSMO(40 nm) / STO(10 nm) / CeO_2(10 nm) / YSZ(80 nm) / Si

(ii) (110)-orientation: PZT(150 nm) / SRO(40 nm) / CeO_2(10 nm) / YSZ(80 nm) / Si

XRD $\theta - 2\theta$ diagrams are displayed for both orientations in Figure III-19, together with representative AFM images of the surface topography. The mosaicity from rocking curves (shown previously, FWHM values) are around 1° for (001)-oriented PZT while it is around 2° for (110)-oriented PZT. The same trend is obtained for the surface roughness, being smaller for (001)-oriented (R_{rms}~2 nm) than for (110) -oriented (R_{rms}~6 nm) PZT.

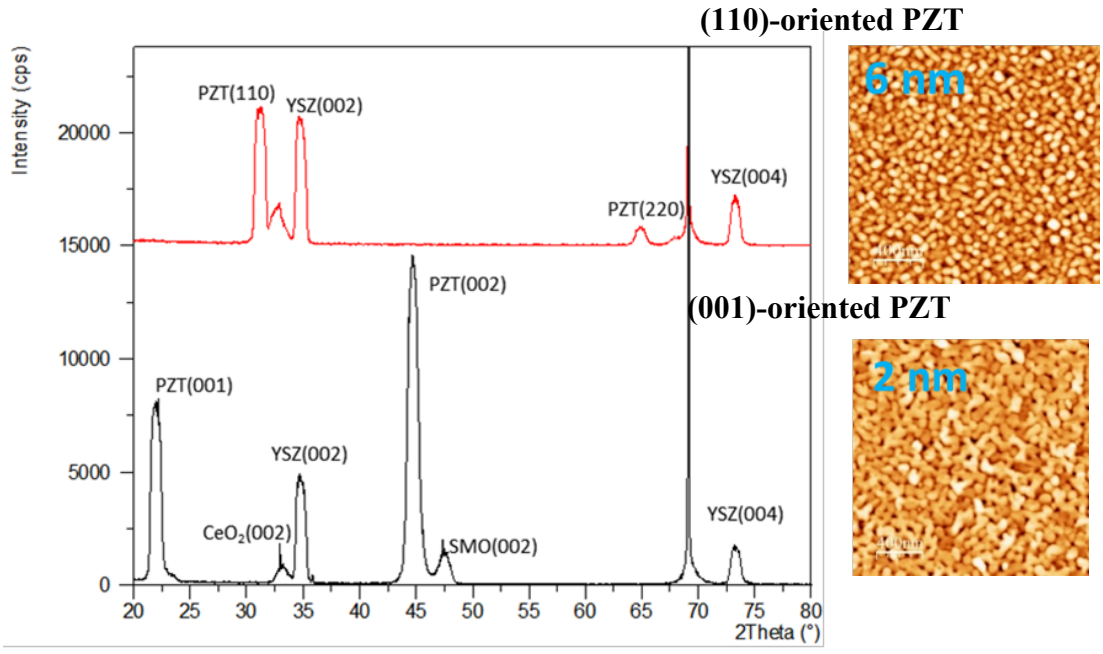

Figure III-19: (a) XRD diagrams of PZT thin films and (b) AFM images (with R_{rms})

Figure III-20 shows the dielectric constant and leakage current for both orientations of PZT. Higher dielectric constant and lower leakage current are obtained for the (110)-oriented PZT film.

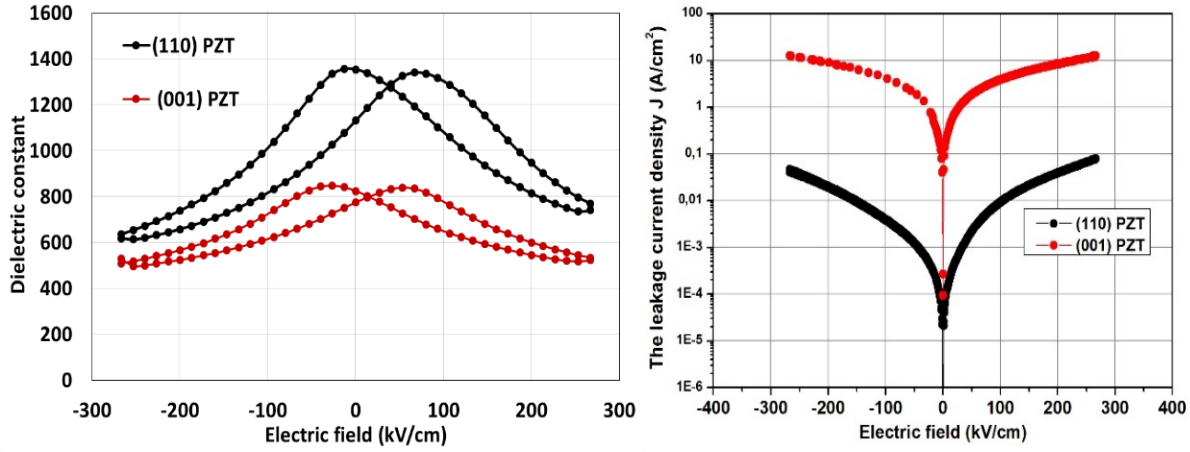

Figure III-20: (Left) Dielectric constant and (Right) leakage current density (J) vs. Electric field for both orientations of PZT films. Top electrode: 30 µm×30 µm.

The fact that the (110)-oriented PZT film is much rougher with smaller grains than the (001)-oriented one (Figure III-19) could play a role in the reduced leakage current density in the former compared to the latter.

Finally, regarding ferroelectric properties, a remnant polarization $P_r \sim 10$ µC/cm^2 is obtained for both orientations, with slight differences depending on orientation and maximum applied voltage in the 240 kV/cm to 400 kV/cm range.

III.6 Magnetostrictive TbFeCo thin films

III.6.1 The growth of magnetostrictive TbFeCo

The study of the growth of TbFeCo thin films is a deep and large study that required lots of time and caution. In this work, fabricating parameters is based on the previous studies by D.T.H. Giang on the same system.

All the magnetostrictive layers in our study have been fabricated using the 6-guns sputtering tool at the laboratory for micro-nanotechnology of Vietnam National University, Hanoi, Vietnam. Thin films were sputtered in RF mode at a base pressure of 3.10^{-7} Torr and Ar gas pressure of 2.2 mTorr. The RF power is 75 W. Distance from the target to the substrate is 5 cm. The deposition rate of TbFeCo is around 1 $Å/s$.

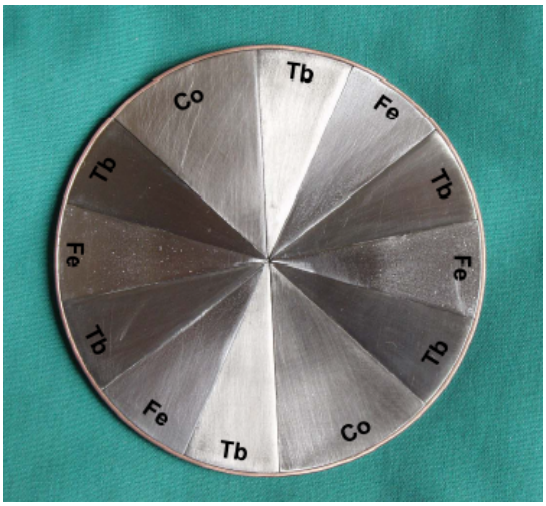

Figure III-21: Photograph of composite TbFeCo target

Thin films described in this thesis are prepared using composite targets consisting of segments bonded to copper backing plates. They were produced based on the concentration calculation:

$$\frac{C_A}{C_B} = \frac{S_A \eta_A}{S_B \eta_B} \qquad \textbf{Eq. III-2}$$

Here, $C_{A,B}$ are the atomic concentrations of A and B elements, respectively; $S_{A,B}$ are total areas of A, B elemental segments of the target; η is the "sputtering yield" which is defined as the number of sputtered atoms per incident ion.

The composite TbFeCo target is a disk of 75 mm diameter and around 1 mm thickness, and comprised of 12 segments as follows: Six Tb segments of area angle $\alpha_{Tb} = 29°$, four Fe segments of $\alpha_{Fe} = 26.5°$, and two Co segments of $\alpha_{Co} = 40°$ as shown in Figure III-21. The composition is calculated from Eq. III-2 with the yields $\eta_{Tb} = 0.82$ atoms/ion, $\eta_{Fe} = 1.10$ atoms/ion, and $\eta_{Co} = 1.22$ atoms/ion [16]:

$$C_{Tb}: C_{Fe}: C_{Co} = (6 \times \alpha_{Tb} \times \eta_{Tb}): (4 \times \alpha_{Fe} \times \eta_{Fe}): (2 \times \alpha_{Co} \times \eta_{Co}) \qquad \textbf{Eq. III-3}$$

$$= 40 : 32.7 : 27.3$$

This gives the composition $Tb(Fe_{0.55}Co_{0.45})_{1.5}$

The magnetostrictive layer was studied after deposition on different substrates. In order to facilitate the measurement of the magnetostrictive properties, $Tb(Fe_{0.55}Co_{0.45})_{1.5}$ films were RF-magnetron sputtered onto the different substrates (100 µm-thick glass, (001)-Si). The thickness of all films is fixed at 1 μm. The hysteresis loops and magnetostrictive properties of the as-deposited samples were determined using vibrating sample magnetometry (VSM) and the bending angle using optical deflection which has been explained in more details in Chapter II.

III.6.2 Magnetic and magnetostrictive properties

III.6.2.a Magnetization

Figure III-22 shows the hysteresis loops of as-deposited TbFeCo films on Si and glass. A magnetic field up to 1 T is applied parallel and perpendicular to the film plane, respectively.

These results show that the easy magnetization direction is out of plane. Such a result has been previously observed in amorphous TbFeCo films [16]. It can be explained due to thermally induced stress during fabrication, the magnetostrictive materials always try to compensate the external or internal stress by appropriate rotation of spins. For a film with positive magnetostriction, tensile stress leads to spin orientation in the film plane, whereas, for a compressive stress the spins orient along the film normal.

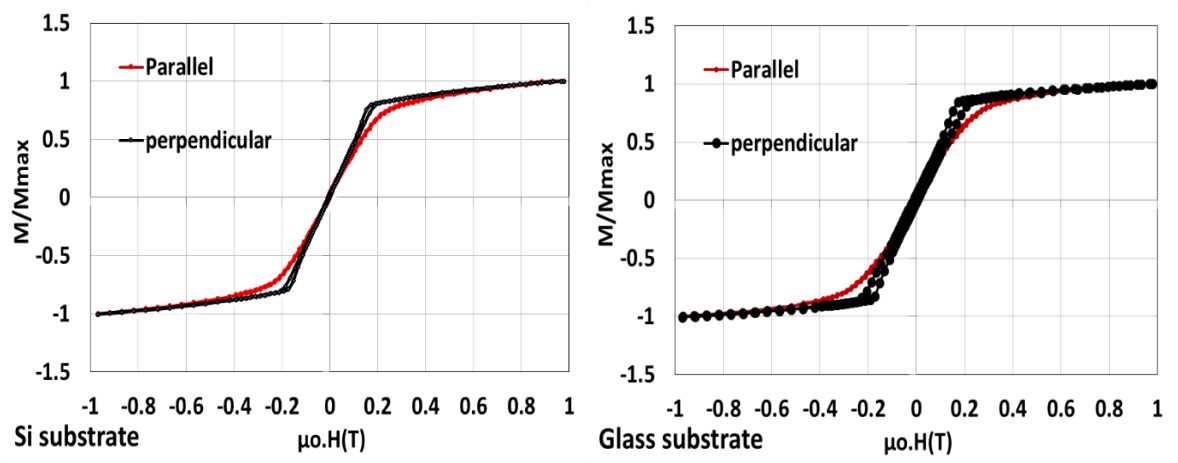

Figure III-22: The perpendicular (black) and parallel (red) normalized magnetization curves plotted for the as-deposited $Tb(Fe_{0.55}Co_{0.45})_{1.5}$ film onto different substrates

For applications, not only a high value of magnetostriction coefficient is required but also the soft magnetic property (low coercive field) needs to be developed. Previous studies on TbFeCo thin films have shown that a heat treatment at 350°C for 1 hour in a vacuum of 10^{-5}Torr [16] can release the stress and enhance in-plane magnetostriction and magnetic softness. Figure III-23 shows magnetization curves for the $Tb(Fe_{0.55}Co_{0.45})_{1.5}$ films after annealing at T = 350°C for 1 hour at 10^{-5} Torr. A change of the magnetic anisotropy from out-of-plane to in-plane is detected. This phenomenon can be explained by the release of stress from the heat treatment that leads to a rotation of the direction of the magnetic moments from the out-of-plane to the in-plane direction. This result is similar to the previously published results using the same material and research methodology [16].

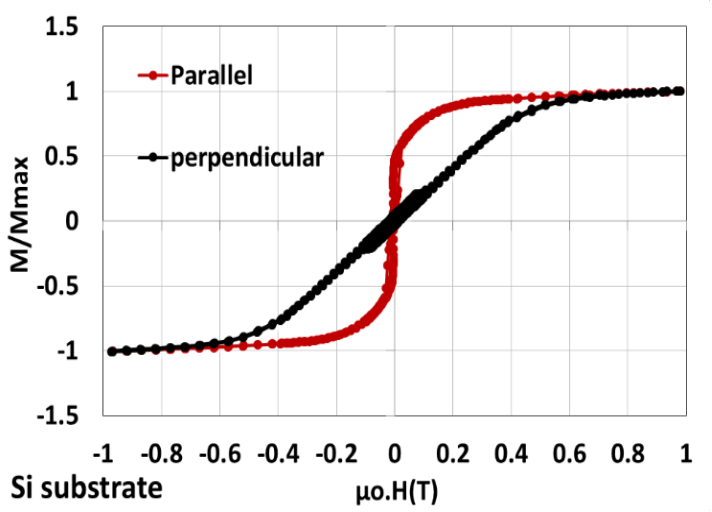

Figure III-23: The perpendicular (blue) and parallel (red) normalized magnetization curves plotted for a $Tb(Fe_{0.55}Co_{0.45})_{1.5}$ film annealed at 350°C for 1 hour at 10^{-5} Torr.

III.6.2.b Magnetostriction

In order to measure the magnetostriction coefficient, the 1 µm TbFeCo film deposited on a glass substrate was cut down to a size of 20×3 mm^2 and stickled on a holder at one end to form a cantilever. Figure III-24 shows the magnetostriction of the sample at room temperature as a function of the investigated magnetic field up to 1 T before and after annealing. The field has been applied in the film plane and along the length of the cantilever. The obtained results show the V-shape and the magnetostriction start to be saturated at magnetic fields higher than 0.7 T for the as-deposited thin film and in the lower-field region (around 0.5T) for the annealed film.

This result indicates that by the heat treatment the soft magnetic character of TbFeCo has been enhanced.

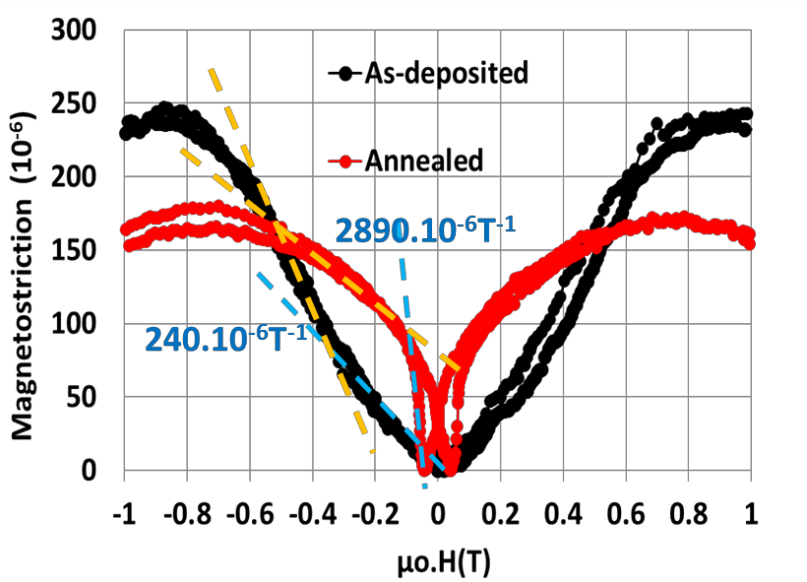

Figure III-24: The magnetostriction coefficient measured in the film plane

Although a remarkable decrease of parallel magnetostriction at high field from 250×10^{-6} to 150×10^{-6} at the highest magnetic field (1 T) was observed, in the small range under 0.5 T of the magnetic field, the annealed thin film reveals a better magnetostriction. Slope of the curve is the magnetostrictive susceptibility. In the different field ranges, both the curves, before and after annealing, exhibit different slopes (see Figure III-24). A slope ratio of 12 is extracted between the annealed and the as-deposited magnetostrictive films (two blue dashed lines) in the range ± 0.07T. This information is useful in considering the possibility of increasing the sensitivity of the sensor.

III.7 Conclusion

Epitaxial PZT thin films were integrated on silicon substrate by PLD using a CeO_2/YSZ double-buffer layer. Further oxide buffers of LSMO/STO or SRO, both having a perovskite structure, have been used to control the crystalline orientation of PZT, either (001)-oriented for LSMO-based PZT, or (110)-oriented for SRO-based PZT. The latter has been chosen to start the fabrication and test of magneto-electric devices, mainly because it exhibited lower leakage current. Regarding the TbCoFe films, their reported magnetostrictive properties are the basis for the expectation of a ME micro-sensor as a resonator based on magneto-electric effect with high sensitivity. As a very first attempt, in the next chapter, the fabrication of the ME micro-sensor and some first results that give support to this statement will be described.

References

[1] M. Laurence, J. Vill, G. Rolland, and F. Laugier, "Double CeO2/YSZ buffer layer for the epitaxial growth of YBa2Cu307_ films on Si (001)substrates," *Phys. C*, vol. 269, pp. 124–130, 1996.

[2] F.Sanchez, R. Aguiar, V. Trtik, C. Guerrero, C. Ferrater, and M. Varela, "Epitaxial growth of SrTiO3 (00h), (0hh), and (hhh) thin films on buffered Si(001)," *J. Mater. Res.*, vol. 5, no. 6, pp. 1422–1425, 1997.

[3] S. J. Wang and C. K. Ong, "Epitaxial Y-stabilized ZrO2 films on silicon: Dynamic growth process and interface structure," *Appl. Phys. Lett.*, vol. 80, no. 14, pp. 2541–2543, 2002.

[4] S. J. Wang, C. K. Ong, L. P. You, and S. Y. Xu, "Epitaxial growth of yittria-stabilized zirconia oxide thin film on natively oxidized silicon wafer without an amorphous layer," *Semicond. Sci. Technol.*, vol. 15, no. 8, pp. 836–839, 2000.

[5] H. Fujisawa, S. Nakashima, K. Kaibara, M. Shimizu, and H. Niu, "Size Effects of Epitaxial and Polycrystalline Pb(Zr, Ti)O 3 Thin Films Grown by Metalorganic Chemical Vapor Deposition," *Jpn. J. Appl. Phys.*, vol. 38, pp. 5392–5396, 1999.

[6] D. L. Bourdais, "Microcapteurs de pression à base de manganites épitaxiées," Universite Paris-Sud, 2015.

[7] Z. Zhao, M. Jamali, N. D'Souza, D. Zhang, S. Bandyopadhyay, J. Atulasimha, and J.-P. Wang, "Giant Voltage Manipulation of MgO-based Magnetic Tunnel Junctions via Localized Anisotropic Strain: Pathway to Ultra-Energy-Efficient Memory Technology," *Appl. Phys. Lett.*, vol. 109, p. 092403, 2016.

[8] Y. Liu, Y. Zhao, P. Li, S. Zhang, D. Li, H. Wu, A. Chen, Y. Xu, X. F. Han, S. Li, D. Lin, and H. Luo, "Electric-Field Control of Magnetism in Co40Fe40B20/(1-x)Pb(Mg 1/3 Nb2/3)O3-xPbTiO3 Multiferroic Heterostructures with Different Ferroelectric Phases," *ACS Appl. Mater. Interfaces*, vol. 8, pp. 3784–3791, 2016.

[9] S. Ziętek, P. Ogrodnik, W. Skowroński, F. Stobiecki, S. Van Dijken, J. Barnaś, and T. Stobiecki, "Electric-field tunable spin diode FMR in patterned PMN-PT/NiFe structures," *Appl. Phys. Lett.*, vol. 109, p. 072406, 2016.

[10] N. Lei, T. Devolder, G. Agnus, P. Aubert, L. Daniel, J.-V. Kim, W. Zhao, T. Trypiniotis, R. P. Cowburn, C. Chappert, D. Ravelosona, and P. Lecoeur, "Strain-controlled magnetic domain wall propagation in hybrid piezoelectric/ferromagnetic structures.," *Nat. Commun.*, vol. 4, p. 1378, 2013.

[11] I. Kanno, H. Kotera, K. Wasa, T. Matsunaga, T. Kamada, and R. Takayama, "Crystallographic characterization of epitaxial Pb(Zr, Ti)O3films with different Zr/Ti ratio grown by radio-frequency-magnetron sputtering," *J. Appl. Phys.*, vol. 93, no. 7, pp. 4091–4096, 2003.

[12] H. B. Palmer, "The Capacitance of a Parallel-Plate Capacitor by the Schwartz-Christoffel Transformation," *Electr. Eng.*, vol. 56, pp. 363–366, 1937.

[13] J. F. Scott, *Ferroelectric Memories*, vol. 3. 2000.

[14] T. Haccart, E. Cattan, and D. Remiens, "Dielectric, ferroelectric and piezoelectric

properties of sputtered PZT thin films on Si substrates: influence of film thickness and orientation," *Semicond. Physics, Quantum Electron. Optoelectron.*, vol. 5, no. 1, pp. 78–88, 2002.

[15] J. Pérez de la Cruz, E. Joanni, P. M. Vilarinho, and A. L. Kholkin, "Thickness effect on the dielectric, ferroelectric, and piezoelectric properties of ferroelectric lead zirconate titanate thin films," *J. Appl. Phys.*, vol. 108, p. 114106, 2010.

[16] D. T. Huong Giang, "Elaboration and study of giant magnetostrictice single layer and multilayer fims based on TbFeCo compound," Uviversite de Rouen and Vietnam national university, Hanoi, 2005.

Chapter IV – The resonant micro-sensor based on PZT micro-cantilevers

This chapter is divided into three parts. Firstly, PZT cantilever integrated on Si as a resonant micro-sensor for sensing magnetic fields based on the ME effect is proposed. Stress is transferred to the PZT layer through the application of a magnetic field to a high ME coefficient material that induces a change of the measured resonance frequency. For these purposes, cantilever, a well-known structure in the field of Micro Electro Mechanical System (MEMS) has been chosen [1], [2]. The cantilever after being released from the Si substrate allows the PZT to generate larger strain and thereby higher power. Due to the reduction of the output signal when minimizing sensor configuration down to the micro-scale, a novel measurement method will be developed, which is expected to further enhance the sensitivity of measurements. The resonant frequency changes induced by strain is caused by DC bias electric field in the PZT micro-cantilever and/or DC magnetic field in the ME micro-sensor, instead of measuring the output electric voltage, response would be an alternative method for the used conventional techniques. Besides that, the influences of other physical parameters such as pressure, DC bias, AC bias were also investigated in this chapter.

Finally, the results of first attempts of a resonator for sensing magnetic signal based on PZT/TbFeCo multi-ferroic thin films are presented. TbFeCo is used as a micro-actuator, while the PZT thin film is used as a micro-sensor. A resonant frequency shift of the device is measured reflecting the magnitude of the external magnetic field.

Outline:

IV.1 PZT cantilever as a resonator for the magnetic sensor application

IV.1.1 Micro-fabrication processes of PZT cantilevers

In several previous studies, PZT-based MEMS devices have been integrated on Silicon-On-Insulator (SOI) wafers which allow the fabrication of complex structures such as membranes thanks to backside etching processes [2]–[4]. In this work, cantilever-based PZT MEMS devices on Si (001) substrates were fabricated. The process requires minimal front-side etching of Si and at the same time allows preserving the ferroelectric properties of PZT after many steps of micro-fabrication processes that correspond to an important challenge for the incorporation of PZT thin films in MEMS. In the literature, several techniques including wet processing [5], Reactive Ion Etching (RIE) [6] and Ion Beam Etching (IBE) have been used to pattern PZT. While wet etching (usually using a mixture of HCl and HF acids) is used for thick PZT films with an etching speed of about 1 $\mu m/min$, which is thus limited in precision, RIE and IBE processes provide the necessary dimensional control for creating MEMS devices from thin-film layers. The RIE process with an etching speed of 20-200 nm/min consists of using a combination of fluorine- and chlorine-containing compounds. While, in the RIE process, physical or chemical etching can be favored by tuning the parameters (pressure and RF-bias power), IBE is a physical etching method with low chemical selectivity, which allows etching complex and inert materials.

The growth of the PZT thin films integrated on Si was presented in chapter 3. In the following, the process flow for the fabrication of the PZT micro-cantilevers will be detailed. A stack of PZT (150nm)/SRO (40nm)/CeO_2 (10 nm)/YSZ (90nm)/Si (after noted as the SRO-based PZT thin film) was prepared for micro-devices. A six-step process (shown in Figure IV-2) was then used to define cantilevers of 40 μm in length and 20 μm in width, with a top electrode having a width of 10 μm. All of the equipment was provided by the C2N laboratory.

The microfabrication process begins with an etching step down to the silicon substrate to structure the desired shape of cantilevers using lithography and Ion Beam Etching (IBE) methods (S2). Due to the different etching rates of oxides and resist (resist etch faster than oxides) by IBE, a thick TI35ES photoresist with high viscosity is used to protect the desired oxide layers area defined by the lithography step during the long etching process. The lithography process, performed under controlled conditions in the cleanroom, starts with the spin-coating step in order to spread the photoresist. The photoresist is spin coated with a

spinning speed of 4000 rotation per minute (RPM) which give rise to a 4 μm in thick photoresist layer. The sample then is soft-baked for 3 minutes at 100 °C using a hot-plate and is then placed under the mask placed in soft – contact mode (MJB4 equipment by Suss MicroTec) to be finally exposed to UV light for 18 seconds. The exposed photoresist is then removed with a developer solution of AZ 400K: H_2O (1: 4) and finally rinsed with pure water. During the IBE process the sample is bombarded with Ar ions which sputter the sample's materials. The angle of incidence of the ion beam is typically adjusted at 45° for all the etching steps to prevent the appearance of redeposited materials on the side of the structures. An electron gun is used to neutralize the charge of accelerated ions to the sample, avoiding any accumulation of surface charges. The experimental parameters used for all steps (Figure IV-2) are given in the following table:

Neutralizer						Ion gun				
Filament		Anode		Extraction		RF	Extraction		Acceleration	
Current	Voltage	Current	Voltage	Current	Voltage	Power	Voltage	Current	Voltage	Current
20A	9.3V	2.5mA	60V	0.2mA	30V	100W	152V	0.5mA	400V	9mA

Table IV-1: The experimental parameters of the IBE etching process

The EndPoint Detection (EPD) method is implemented in the IBE tool and uses a Second Ion Mass Spectrometry (SIMS) technique to follow in real time the etching and to stop it at the desired layer. SIMS allows to monitor the etching by measuring the mass of the etched atoms, thus allowing to identify the layer that is etched. An example is presented in Figure IV-1 where typical signal of PZT (Pb is watched) is observed up to 1000", followed by $SrRuO_3$ (Sr is watched) and $SrTiO_3$ (Sr is watched but intensity is higher because of higher etch rate) and then finally the broad YSZ signal (Zr is watched), Ce atoms being not watched during this etching.

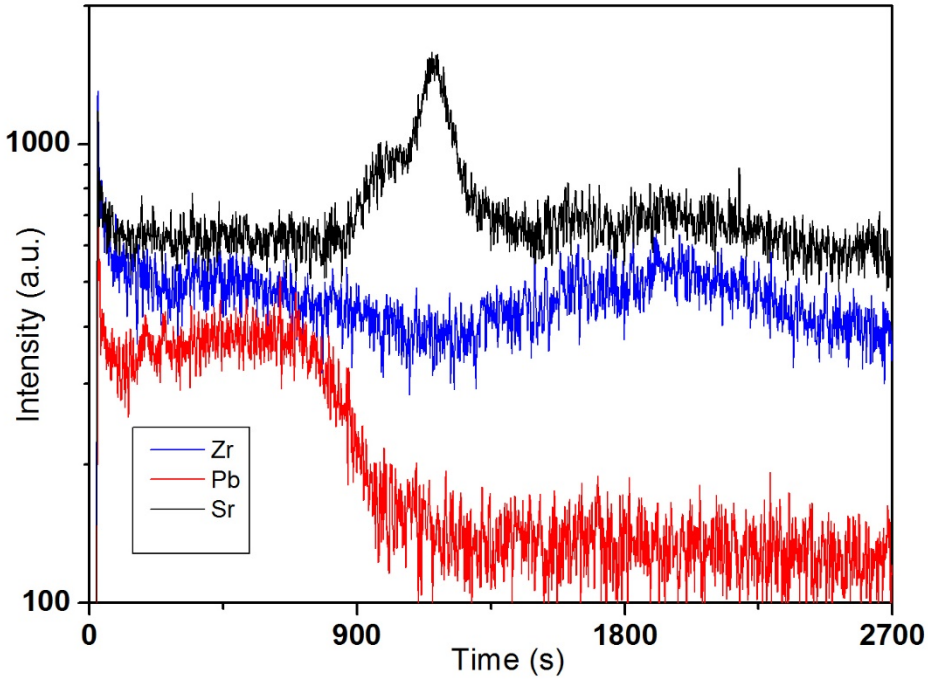

Figure IV-1: Second ion mass spectrometry trace of the SRO-based PZT cantilever

In order to ensure a good electrical contact between the bottom electrode and external wires (placed by wire bonding), the deposition of electrodes has been done as follows (patterning process (S4 and S6) in Figure IV-2):

a) Etching down to the bottom electrode (SRO layer) (S4): This process is similar to that used previously for etching down to the silicon substrate. The different photoresist AZ5214E has been used with spinning speed of 4000 rpm corresponding to 1.4 µm in thickness of the photoresist layer. The sample is soft-baked for 90 seconds at 110 °C using a hot-plate. The sample is then placed under the mask and exposed for 4 seconds to UV. The resist is further baked for 120 seconds at 120°C on a hot plate and illuminated by UV (for 50 seconds) on the whole sample surface. These last two steps are called resist inversion. After the first exposure and baking, the exposed areas of the resist become insoluble in the developer solution. The areas of the resist which were not modified during the first exposure are now made soluble thanks to the second exposure (called flood exposure) and are finally removed in a developer solution of AZ 400K: H_2O (1: 4), then rinsed with pure water. This lithography

process is called negative lithography. The IBE etching process (described previously) is controlled by SIMS to stop at the SRO bottom layer.

b) Deposition of the metal layer (Platinum) (S6): For this process, the same lithography process as for S4 step (negative photolithography) has been used: the positive photoresist (photoresist AZ5214E) (spin-coated at 4000 rpm, baked for 90 seconds at 110 °C, and exposed with a mask for 4 seconds) has been further treated by annealing (for 120 seconds at 120°C) to become negative, and then exposed to UV without a mask (Flood exposure). The photoresist is then removed in a developer solution of AZ 400K: H_2O (1: 4) and rinsed with pure water for 20 seconds. Following this lithography process, the remaining resist acts as a protective mask during the deposition of a 100 nm thick Pt layer by sputtering. After deposition, the resist is removed by acetone (called lift-off step) and the sample is rinsed with isopropanol. At the end, the Pt layer provide a good electrical contact with the SRO bottom electrode.

Prior to the deposition of Pt to make the top contacts, a silicon nitride (Si_3N_4) layer is deposited on the PZT surface (S3). This way, small size of Pt top electrode will be in contact with PZT (limiting the area where electric field will be applied and thus leakage problem), and larger Pt area (deposited on Si_3N_4) will be used for the wire-bonding. Si_3N_4 layer (of 200 nm thickness) is deposited by sputtering after a negative photolithography process (S3).

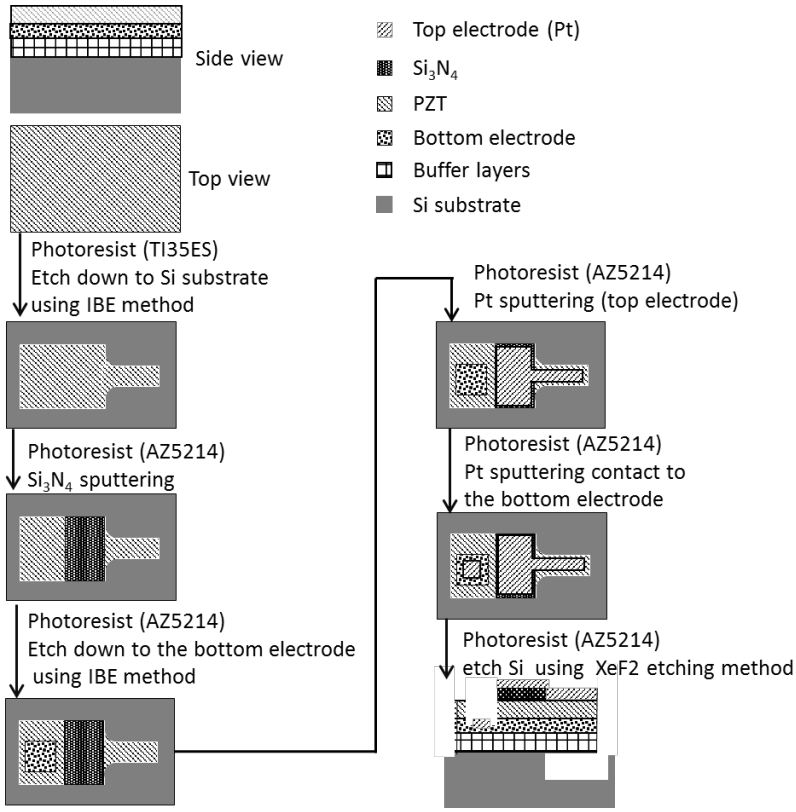

Figure IV-2: Schematic of the micro-fabrication process of PZT cantilever on silicon substrates

A 100nm-thick top electrode (Pt) is then patterned by the fourth mask (negative photolithography) and obtained by a lift-off process after the deposition by sputtering (S5).

Finally, cantilever structures are shaped and released from Si by sacrificial etching of the silicon substrate underlying the cantilever pattern (S7) by XeF_2 etching method. This method is highly selective to silicon with respect to photoresist and silicon dioxide or any functional oxides and takes place according to the following reaction:

$$2XeF_2 + Si \rightarrow 2\,Xe \uparrow + SiF_4 \uparrow$$

The advantages of this method are its fast etching rate together with selectivity. After etching silicon, the photoresist is removed by using oxygen plasma.

Preliminary characterization of PZT micro-cantilevers

An example of a 3D image of such fabricated cantilever is shown in Figure IV-3, and was obtained by optical profilometer presented in chapter 2.

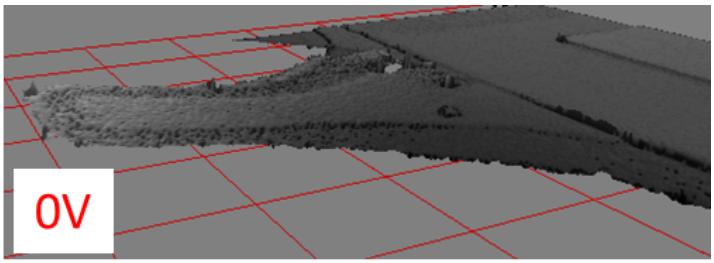

Figure IV-3: A typical 3D image of the cantilever captured by interferometry method

The ferroelectric properties of the PZT cantilevers are the main parameters to evaluate the fabrication process. Therefore, the measurements of the ferroelectric properties (including ferroelectric loop and capacitance) were carried out before and after the micro-process. Ferroelectric characteristics of cantilever were investigated by polarization hysteresis (P-E) loop measured between $\pm 266\ kV/cm$. The capacitance-electric field (C-E) curve was carried out using an AC signal of *30 mV* and 100 kHz frequency with the DC bias sweeping from -266 kV/cm to +266 kV/cm and back to -266 kV/cm. The corresponding dielectric constant ε was calculated from the C-E curve obtained. The polarization switching was observed around $-20\ kV/cm$ and $65\ kV/cm$ after the microfabrication process as shown in Figure IV-4.

The remnant polarization is about $10\mu C.cm^{-2}$, and this value is close to the value measured after the micro-processes. As the ferroelectric properties are not altered by the Si releasing process, we conclude that this step does not induce strong modification of the PZT nor than the stress relief. The difference in dielectric constant on the measurement before and after releasing is due to the measurements taken place on the different region on the sample with the different size of capacitors.

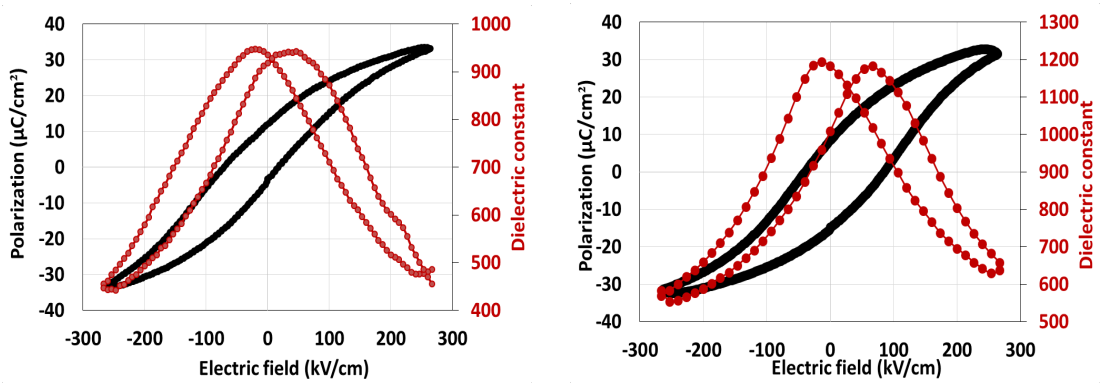

Figure IV-4: Polarization hysteresis (P-E) loop (in black) and dielectric constant (ε - E) curve (in red) for the PZT cantilever before (a) and after (b) the microfabrication process.

The ferroelectric characteristics exhibit a shift to the positive voltage direction after the process. Shifted loops can be explained by dissimilar top and bottom interfaces (electrodes materials, interface charge traps). Here, the shift of the curve observed after cleanroom processes could come from the change of the residual stress after releasing PZT stacks from the Si substrate. The effect of stress on ionic positions and vibrations in ferroelectric materials that lead to a change in the polarization mechanism and the ferroelectric properties has been investigated in previous studies [7].

IV.1.2 Static response

Before going into resonant responses of the PZT cantilever, the static response or the behavior of the PZT cantilever upon a DC excitation is studied. In this case, stress is generated from PZT itself through the piezoelectric effect by the application of a DC electric field. The measurement of the cantilever deflection under the applied electric field is used to determine the piezoelectric constant d_{31} and the stress induced by the PZT layer.

The cantilevers are composed of active (PZT) and inactive layers. When a DC electric field is applied to the PZT layer between the two electrodes, a stress gradient will change the shape of the PZT layer due to the piezoelectric effect. This change is restricted by the inactive layers, leading to the observed deformation of the cantilever. The maximum deflection of the free end of the cantilever as a function of DC field can be obtained by interferometric profilometry method in ambient conditions (temperature and pressure).

In previous reports [3], [4], [8], [9], a Laser Doppler Vibrometer (LVD) technique has been used to measure the displacement of a PZT cantilever. A sinusoidal AC-voltage at low frequency is applied to the structure. The frequency is chosen to be well below the resonance frequency of the cantilever in order to avoid the strong effect of resonance phenomenon on the displacement. These reported measurements were carried out at a high DC bias to ensure unipolar excitation. The main difference of this method with the interferometric profilometry method is that the effect of polarization states of PZT thin film on the displacement under DC bias can be evaluated.

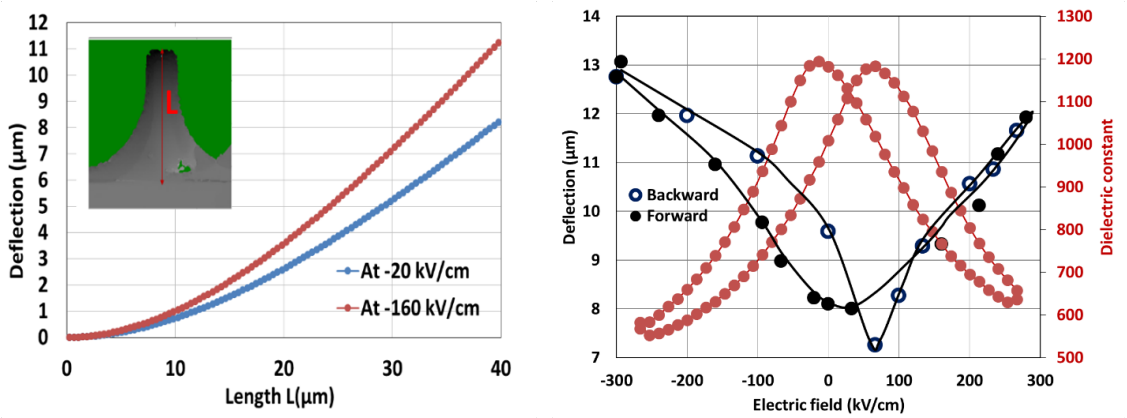

Figure IV-5: The profile of the cantilever at -120kV/cm and -20kV/cm applied (left) and its displacement (in black) as a function of the applied DC electric field (from positive to negative field in filled symbols and from negative to positive field in open symbols) superposed with the dielectric constant curve (right). The cantilever consists of 150 nm PZT layer with SRO bottom electrode with 40 μm in length, 10 μm in width and 100 nm thick Pt top electrode.

Figure IV-5 left shows the response of the SRO-based PZT cantilever upon the DC electric field excitation. An upward bending of the cantilever of around 8µm at the cantilever free end already exists even at zero DC bias voltage that is explained by residual stress gradient in the cantilever even after the releasing step. The presence of residual stresses is unavoidable during the deposition of such a complex stack, because of the initial bending of the cantilever. The residual stress originates from the mismatch in the thermal expansion coefficients of different materials and from the lattice mismatch between each layer during the deposition. A distinct coefficient of thermal expansion between PZT ($6x10^{-6}$ K^{-1} [10]) and the silicon substrate ($4.4x10^{-6}$ K^{-1} [10]) causes the development of a thermal stress during the cooling process from

the deposition temperature to room temperature. The contribution of the mismatch of lattice constants among layers is also significant to the initial bending of the cantilever after releasing from Si. In the case of the SRO-based PZT micro-cantilever, the upward deflection implies the existence of compressive stress at the top or a tensile stress at the bottom of the stack.

Figure IV-5 right is a plot of the position of the free-end of the cantilever when the electric field is swept from -266 kV/cm to 266 kV/cm, then back to -266 kV/cm. It is observed that the deflection curve follows a conventional butterfly shape of the C-E curve with a total variation of 6 μm. At high electric field, the deflection of the cantilever is maximum, while it is minimum around the switching voltage (disordered polarization state of PZT).

The observed maximum deflections higher than the 2 μm displacement measured for a 2 μm thick PZT cantilever at 20V (corresponding to 200 kV/cm applied electric field) using Sol-gel deposition by D. Ambikaet et al. [11]. The main point is that the cantilevers actuated by very thin epitaxial PZT films enable large deflection at low voltages, which could be of great interest in many low voltage applications.

In [12]and [13], piezoelectric coefficient d_{31} are determined from the cantilever vertical deflection using the following formula based on the heterogeneous bimorph model:

$$\delta = \frac{3 d_{31} s_S s_P t_s (t_s + t_p) L^2 V}{s_s^2 t_p^4 + 4 s_s s_p t_s t_p^3 + 6 s_s s_p t_s^2 t_p^2 + 4 s_s s_p t_p t_s^3 + s_p^2 t_s^4} \qquad \textbf{Eq. IV-1}$$

Where δ, s, t, L, V are the deflection [m], the mechanical compliance [m/N^2], the thickness [m], the length [m] and the excitation voltage [V]. Subscripts ‘s’ and ‘p’ denote the substrate or the PZT properties. The mechanical compliance is related to Young’s modulus E by s=1/E.

This equation, however, is only valid when the thickness of the thin film is much thinner than the substrate and when the thicknesses of buffer and electrode layers are small in comparison to the thickness of PZT. This structure can be normally found in cantilevers fabricated using Silicon-On-Insulator (SOI) wafer. In this thesis, Si has been removed after micro-processes and the thickness of each layer can be similar. Figure IV-6 is the schematic of the cantilever structure used in this thesis.

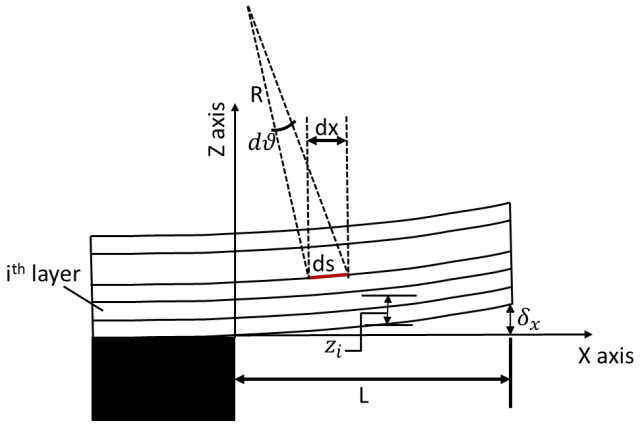

Figure IV-6: Schematic of a cross-sectional view of the PZT cantilever structure in this thesis

In order to take into account the effect of buffer and electrode layers in calculations, Weinberg et al [14] described a multi-morph model. Firstly, the neutral axis for torque inputs is determined:

$$\boldsymbol{Z_M = \frac{\sum_i z_i E_i A_i}{\sum_i E_i A_i}} \qquad \textbf{Eq. IV-2}$$

Where z_i is measured from the arbitrary reference to the center of area *i*. $A_i = w_i t_i$ is cross-section area of layer i. w_i, t_i, E_i are the width, thickness and Young's modulus of layer *i.* The curvature of the cantilever is expressed by

$$\boldsymbol{\frac{1}{R} = \frac{E_p Z_p w_p d_{31} V}{\sum_i E_i A_i (t_i^2/12 + Z_i^2)} + A} \qquad \textbf{Eq. IV-3}$$

The micro-cantilever width is comparable to its length; therefore, Young's modulus and piezoelectric coefficients above can be replaced by $E_i \rightarrow E_i/(1-\upsilon^2)$ and $d_{31} \rightarrow d_{31}/(1+\upsilon)$. A is a constant corresponding to the initial bending of the cantilever.

According to the theory for a cantilever with a uniform load of intensity ρ, the curvature R may be expressed as:

$$\boldsymbol{k = \frac{1}{R} = \frac{d\vartheta}{ds}} \qquad \textbf{Eq. IV-4}$$

The angle ϑ or slope between the x-axis and the tangent to the deflection curve is defined by:

$$\tan\vartheta = \frac{d\delta_{(x)}}{dx} \qquad \text{Eq. IV-5}$$

For a small angle ϑ, $ds \approx dx$ and $cos\vartheta \approx 1$, then $tan\vartheta \approx \vartheta$

$$\vartheta = \frac{d\delta_{(x)}}{dx} \text{ and } k = \frac{1}{R} = \frac{d\vartheta}{dx} = \frac{d^2\delta_{(x)}}{dx^2} \qquad \text{Eq. IV-6}$$

By solving the equation for x=L at the free end of the cantilever using $\delta = L^2/2R$ along with Eq. IV-3, the value of $d_{31} = -53\ pmV^{-1}$ was estimated from the slope of the linear dependence of deflection with the electric field (Figure IV-5) using parameters in **Table IV-2**. This value is smaller than that of similar 1 µm-thick PZT films (-118.9 pmV^{-1}) reported by Dekkers et al. [2]. By the same group, a $d_{31}$of $-97\ pmV^{-1}$ was reported on 750-nm-thick $Pb(Zr_{0.52}Ti_{0.48})O_3$ [15]. This smaller value can be explained by the use of a thinner PZT layer, as reported by Haccart et al [16].

IV.1.3 Dynamical response

For the static-mode operation presented in the previous section, the stress generated under DC electric field induces a change of the deflection which was measured by optical profilometry. This approach allows to study some basic characteristic of the cantilever and to extract some physical parameters such as the piezoelectric coefficient of such microprocessed PZT integrated on silicon and the level of stress generated by the DC bias.

The final objective of this work is to sense magnetic field through ME effect that will be measured by the change of the resonant frequency of the cantilever. A preliminary study of the dynamical response of the PZT cantilevers was performed where the electrical response of such PZT cantilevers as a micro-resonator was chosen to characterize. In this case, a static stress is transferred to the PZT layer through the application of the small AC sine-wave superimposed with a DC voltage that simulate the presence of the ME film under a magnetic field. A shift of the resonant frequency is expected with the applied DC bias that is recorded by impedance measurement.

IV.1.3.a Theory of resonant frequency

The resonant frequency (f_r) of a typical cantilever theoretically expressed in the following equation shows the relationship between approximate value of the resonant frequency and its mechanical properties:

$$f_r = C_n^2 \frac{t_{cant}}{2\pi L^2} \sqrt{\frac{E_{cant}}{12\rho_{cant}}} \qquad \textbf{Eq. IV-7}$$

Where C_n is a constant depending on the vibration mode n ($C_0 = 1.875, C_2 = 4.694, C_3 = 7.855$ for the first, second, and third mode of the resonance frequency, respectively). t_{cant} is the thickness of cantilever, E_{cant} $(= \sum E_i t_i)$ and ρ_{cant} $(= \sum \rho_i t_i)$ are the elastic modulus and density of the cantilever. [8], [17] **Table IV-2** shows material properties and geometry dimensions used in the calculation of PZT based cantilever such as the reference where those values were taken from.

	Young's modulus (Pa)	Poisson's Ratio	Density (kg/m3)	Thickness (μm)	Length (μm)	Width (μm)	Ref
Si	1.30×10^{11}	0.28	2329				[2]
YSZ	2.00×10^{11}	0.3	5900	0.09			[18]
CeO_2	2.00×10^{11}	0.3	7215	0.01			
STO	2.38×10^{11}	0.23	5120	0.01			[19]
SRO	1.61×10^{11}	0.3	6490	0.04			[20]
LSMO	5.62×10^{11}	0.43	6280	0.04			[21]
PZT	0.952×10^{11}	0.35	7500	0.15			[2]
Pt	1.68×10^{11}	0.38	21450	0.1			[2]
SRO-based PZT Cantilever	1.46×10^{11}	0.321	1070	0.38	40	20	

Table IV-2: Material properties and geometry dimensions used in calculation of PZT cantilever

Thanks to the analytical expression of Eq. IV-7, the resonant frequency of the first three modes of the SRO-based PZT cantilever, in the considered geometry, is calculated. Those values are shown in **Table III-3**. The frequency ratios between these modes are 1: 6.22: 17.61.

Mode	Theory (kHz)
1, 0	172
2, 0	1070
3, 0	3030

Table IV-3: Resonant frequencies calculated for the PZT micro-cantilever

The resonance behavior of such piezoelectric materials can be described by an equivalent circuit as reported by Butterworth Van Dyke (BVD), which is widely used in the literature and basic definition of IEEE standard. This circuit consists of two shunted branches, capacitor C_o on one branch, and a resistance R_m, inductance L_m, conductance C_m all in series on another one. The circuit elements R_m, L_m, C_m are known as the motional parameters which are internal losses of the vibration and stiffness, while the element C_o corresponds to the shunt capacitance formed by electrodes and the PZT dielectric or the static capacitance which can be determined as the effective capacitance at frequencies far from resonance. This equivalent circuit is shown in Figure IV-7-left. Figure IV-7-right show a typical response of the impedance and phase response of such a resonator while varying the excitation frequency. While looking at the impedance curve, 2 peaks are observed, whose origin will be immediately clarified.

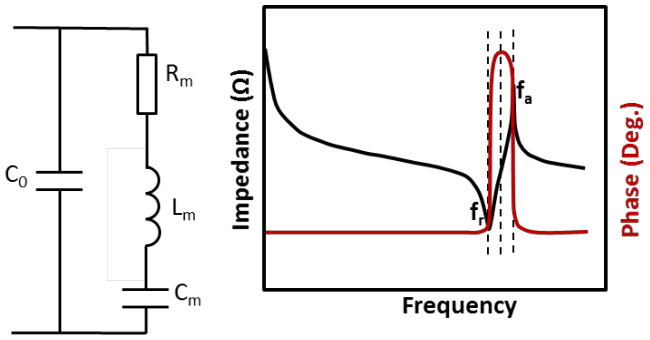

Figure IV-7: The equivalent circuit Butterworth Van Dyke

The total impedance of this circuit is given by:

$$Z_T = \frac{\left(-\frac{j}{\omega C_0}\right)\left[R_m + j\left(\omega L_m - \frac{1}{\omega C_m}\right)\right]}{\left(-\frac{j}{\omega C_0}\right) + \left[R_m + j\left(\omega L_m - \frac{1}{\omega C_m}\right)\right]}$$

$$= \frac{R_m + j\left(\omega L_m - \frac{1}{\omega C_m}\right)}{1 + \mathrm{j}\omega C_0\left[R_m + j\left(\omega L_m - \frac{1}{\omega C_m}\right)\right]}$$

$$= \frac{j\omega R_m C_m + (\omega^2 C_m L_m - 1)}{j\omega[\omega^2 C_m L_m C_0 - (C_m + C_0)] - \omega^2 R_m C_m C_0} \qquad \textbf{Eq. IV-8}$$

From the above function, the frequency where the total impedance is minimum is called the series resonance frequency ω_r or the resonance frequency. At this frequency, qualitatively, inductance and capacitance effect cancel each other, and the impedance is thus minimal. ω_r is given by the following equation:

$$\omega_r = \frac{1}{\sqrt{C_m L_m}} \qquad \textbf{Eq. IV-9}$$

The frequency where the total impedance is maximum is named the parallel resonance frequency ω_a or anti-resonance frequency, and is calculated by:

$$\omega_a = \frac{1}{\sqrt{\frac{C_m C_0}{C_m + C_0} L_m}} = \omega_r \left(\sqrt{\frac{C_m}{C_0} + 1} \right) \quad \textbf{Eq. IV-10}$$

Due to $\frac{C_m}{C_0} \ll 1$, Taylor expansion give us: $\omega_a \approx \omega_r (1 + \frac{C_m}{2C_0})$ **Eq. IV-11**

Determination of constants C_m, C_o, L_m, R can thus be obtained from the experimental measurement by considering all boundary conditions. At the resonant frequency, the equivalent circuit consists of only resistance Rm and capacitance C_o in parallel. The impedance is:

$$Z_{\omega_r}^2 = \frac{R_m^2}{1 + R_m^2 (\omega_r C_0)^2}$$

$$\rightarrow R_m = \frac{Z_{\omega_r}}{\sqrt{1 - Z_{\omega_r}^2 \omega_r{}^2 C_0{}^2}}$$

Capacitance C_m and inductance L_m are deduced from (Eq. IV-9) and (Eq. IV-10) functions according to C_o:

$$C_m = C_0 \left[\left(\frac{\omega_a}{\omega_r} \right)^2 - 1 \right]$$

$$L_m = \frac{1}{C_m \omega_r^2} = \frac{1}{C_0 (\omega_a^2 - \omega_r^2)}$$

At the anti-resonant frequency, the total impedance is:

$$Z_{\omega_a} = \frac{(1 - \omega_a^2 C_m L_m) - j\omega_a R_m C_m}{\omega_a^2 C_m R_m C_0}$$

$$\rightarrow Z_{\omega_a}^2 = \left[\frac{(1 - \omega_a^2 C_m L_m)}{\omega_a^2 C_m R_m C_0} \right]^2 + \left(\frac{1}{\omega_a C_0} \right)^2 = \left[\frac{\sqrt{1 - Z_{\omega_r}^2 \omega_r^2 C_0^2}}{Z_{\omega_r} \omega_a^2 C_0^2} \right]^2 + \left(\frac{1}{\omega_a C_0} \right)^2$$

$$\rightarrow C_0 = \sqrt{\frac{Z_{\omega_r}^2 (\omega_a^2 - \omega_r^2) + \sqrt{Z_{\omega_r}^4 (\omega_a^2 - \omega_r^2)^2 + 4 Z_{\omega_a}^2 Z_{\omega_r}^2 \omega_a^2}}{2 Z_{\omega_a}^2 Z_{\omega_r}^2 \omega_a^4}} \quad \textbf{Eq. IV-12}$$

Evaluation of the electrical behavior of the equivalent circuit is necessary to analyze the losses of such materials. Those values of C_m, C_o, L_m, R_m, can directly be obtained from the

resonance frequency measurement but are also linked to the electrical or mechanical properties of the material, the measurement conditions according to Table IV-4.

$C_0 = \frac{\varepsilon_0.\varepsilon_r.S}{t}$	$R_m = \frac{\pi.\eta.\varepsilon_0.\varepsilon_r}{t.8k_{eff}^2.\rho.S\nu_a}$	$L_m = \frac{\pi^3.\nu_a}{8\omega_r^2.\varepsilon_0.\varepsilon_r k_{eff}^2.S}$	$C_m = \frac{8k_{eff}^2.C_0}{\pi^2}$

Table IV-4: The relationship between the elements Cm, Co, Lm, Rm and the electrical or mechanical properties of the material

ε_0 and ε_r are respectively the vacuum [F/m] and the relative permittivity [no dimension], S the electrodes surface [m^2], t the resonator thickness [m], η the piezoelectric material viscosity [Pa.s], ρ its density [kg/m^3], k_{ef} the effective electromechanical coupling coefficient of the system [no dimension], ν_a the wave speed [m/s] and ω_r resonating pulsation [rad/s]. Resistance, inductance and capacity are expressed in Ohm [Ω], Henry [H] and Farad [F].

The quality factor Q

The quality factor Q reflects the sharpness of the resonant peak and can also be determined through the resonant measurement. A large Q factor leads to a sharp resonant peak, which results in a higher ability in detecting small shifts in the resonant frequencies during an experimental measurement. Actually, a small change in the frequency induces a large change of the measured signal if the resonant peak is sharp. Therefore, a higher Q factor is to be favored aiming any application based on resonant frequency measurement. This factor can be determined according to [22][23]:

$$\boldsymbol{Q = 2\pi \frac{stored\ vibrational\ energy}{energy\ lost\ per\ cycle\ of\ vibration} = \frac{f_p}{f_a - f_r}\ \text{or}\ Q = \frac{f_p}{\Delta f}} \qquad \textbf{Eq. IV-13}$$

Here Δf is the full width at half maximum (FWHM) of the resonant peak determined from the angle phase plot. E_{max} is the maximum energy stored, E_{lost} is the total energy loss.

From the equation Eq. IV-13, the Q-factor depends on the difference between the anti-resonant frequency and the resonant frequency Δf. The higher this difference is, the lower the Q-factor is. The relationship between Q-factor and the elements of the equivalent circuit BVD can be expressed as following:

$$\boldsymbol{Q = \frac{f_p}{f_a - f_r} \approx \frac{1}{2}\left(\frac{\omega_a + \omega_r}{\omega_a - \omega_r}\right)}$$

$$\boldsymbol{\approx \frac{1}{2} + \frac{2C_0}{C_m}} \qquad \textbf{Eq. IV-14}$$

Quality factor can be affected by 2 kinds of sources:

- The material itself such as the presence of defects in volume or at the interfaces, that will lead to a value of the intrinsic quality factor;
- The loss through the binding, the environment of the resonator, the contact quality… taking into account these losses and the one of the material will give rise to the global quality factor.

It can thus be interesting to measure the resonant frequency of a cantilever under different conditions to have access to the material properties itself, in particular measurement under vacuum allows avoiding the damping effect from the air environment.

Effective electromechanical coupling Coefficient (k_{eff})

From the resonant measurements, effective electromechanical coupling coefficient (k_{eff}), which presents the efficiency of transformation from electrical energy to mechanical energy [24], [25] can also be calculated:

$$k_{eff}^2 = \frac{\pi}{2}\frac{f_r}{f_a} tan\left(\frac{\pi}{2}\frac{f_a - f_r}{f_p}\right) \qquad \textbf{Eq. IV-15}$$

This value is known to be one of the highest in PZT with respect to other piezoelectric materials [26].

IV.1.3.b Methods of study

Resonant characteristics: an impedance/phase analyzer

There are a few ways to determine the resonant frequency. The Laser Doppler Vibrometer, or LDV, can be used to measure the resonant responses of piezoelectric actuators, which was shown advantageous in several previous studies [3], [4], [8], [9]. In those reports, a small AC sine-wave superimposed with a DC voltage was applied to the PZT cantilever. No explanation was given concerning the choice of the values of the AC and DC biases. The effect of DC bias on the behavior of the cantilever through the change in polarization direction was not considered.

In references [5], [6], [23], impedance/phase analyzer is used in order to find out the value of the resonant frequency. The impedance analyzer outputs an AC voltage and measures the current necessary to maintain this AC voltage. The current or the impedance generated by the PZT cantilever is measured when the frequency of the AC voltage sweeps.

The same strategy was followed and a Hioki IM 3570 was used which is an impedance analyzer in order to measure the frequency characteristics using the frequency sweep function in analyzer mode. This equipment allows a frequency band within the range of 4 Hz to 5 MHz to be set with five-digit resolution and the maximum value 2.5 V of DC bias. In Figure IV-9 the image of Hioki IM3570 and an actual measurement of $Z\,(impedance) - \theta$ (phase) parameter with respect to the frequency are shown. In this work, this equipment is used to determine the resonance frequency and impedance. This method will also be used for the ME measurements. Care should be taken for such measurements, as heat generation due to the application of DC bias during a long period may shift the resonance frequency [27]. Resonant frequency measurements were done and much higher changes were observed than the ones corresponding to the few tens of ppm of Temperature Coefficient of Frequency reported in the literature (50 ppm reported for quartz).

Typical resonant characteristics of a PZT micro-cantilever: impedance measurement

First, the major resonant modes of the micro-cantilever are determined by recording both $Z\,(impedance) - \theta$ (phase) while sweeping the excitation frequency in a broad range (typically from 20 kHz to 2.5 MHz). In this measurement, small excitation AC bias of 100

mV_{pp} is applied without any DC bias. Taking as an example the SRO-based PZT cantilever from Figure IV-8, the first three modes of resonance could be measured at 154.4 kHz, 846.75 kHz and 2278,6 kHz that can be compared with the calculated values of **Table IV-3**. The frequency ratios between the first three fundamental modes are 1: 5.48: 14.75 as shown in Figure IV-8. The insets of Figure IV-8 illustrate the corresponding modal shapes. Those experimental ratios are in good agreement with the expected ones, thus hinting the first three modes are explored in this range of frequency.

Typical error of the calculation with respect to the experimental are in the range of 12% error for the first mode and this difference can have several explanations such as residual stress that can affect the mechanical properties, or the difference in geometry between the design and the fabrication. As an example, according to the theory, an increase in the length from 40 μm to 42 μm leads to a change in the resonant frequency of 9 kHz from 172 KHz to 163 KHz. Considering the accuracy of the optical lithographic process used in this thesis, this error thus seems totally acceptable.

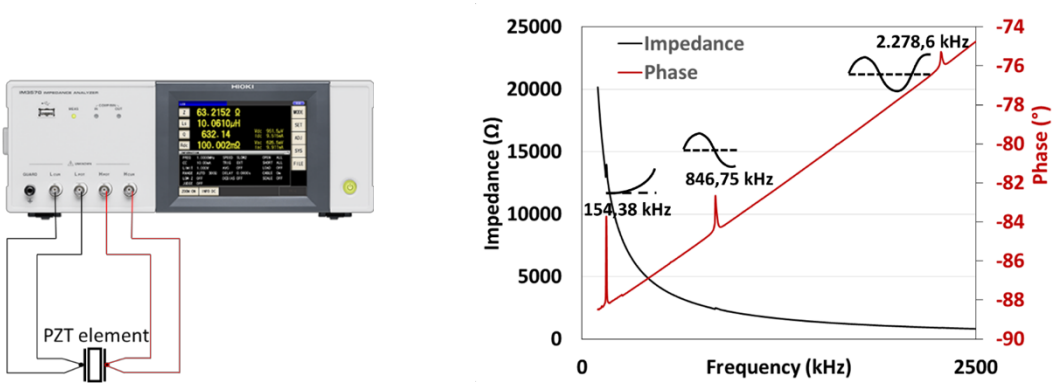

Figure IV-8: The image of Hioki IM3570 and The first three modes of the SRO-based PZT cantilever obtained by Hioki IM3570. In this measurement, an exciting AC bias 100 mV_{pp} imposed on a 0V DC bias has been set.

Figure IV-8 shows that the impedance background of the impedance signal varies a lot with the frequency, not considering the motion part. This impedance vs frequency dependence corresponds to the well-established variation of $Z_{C_0} = {}^{1}/_{j\omega C_0}$ with the frequency.

In general $C_0 \gg C_m$, therefore, the useful signal (the motional signal) has been extracted by subtracting this background. Due to the higher amplitude and higher stability of the output signal, the first mode of vibration of the cantilevers was generally chosen in order to investigate

its mechanical properties. Figure IV-9 shows a zoom in the frequency range where this resonant frequency appears where the shape of the impedance and phase response are in fair agreement with the expected one. However the phase peak seems asymmetric which is explained by the linear response of the PZT with the electric field, this will be further discussed in section IV.1.4.a.

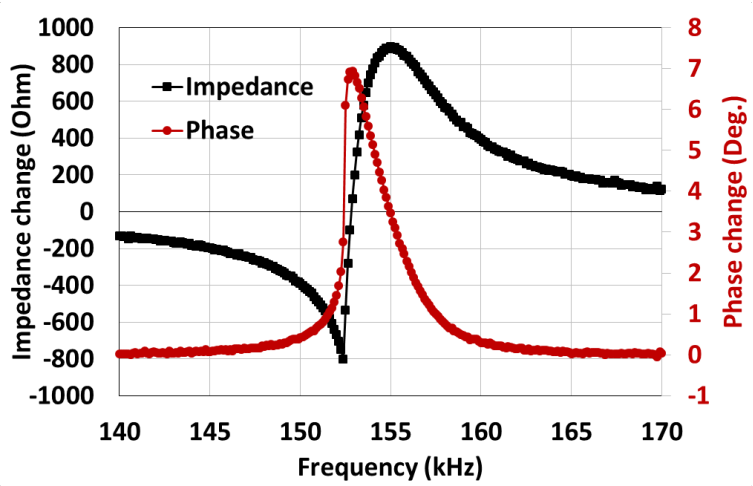

Figure IV-9: The actual measurement of $Z - \theta$ parameter with the frequency around the first resonant mode

From the resonant curve, the values of capacitive elements of the equivalent circuit are determined and listed in **Table IV-5**. The SRO-based PZT cantilever shows a C_0/C_m ratio of 31.7, a value that should be maximized in order to enhance the Q-factor (Eq. IV-14). This value remains obviously far from the state-of-the-art quartz crystal but is comparable to bulk PZT materials. Thus the thin films which are integrated on silicon with the proposed YSZ based buffer exhibit characteristics close to the characteristics of the bulk ones.

Parameter	$C_m(pF)$	$C_0(pF)$	C_0/C_m	Ref
The SRO-based PZT cantilever (this thesis)	1.8	57	31.7	
The PZT with 40 mm of diameter and 3 mm of thickness	90	3000	33.3	[24]
A quartz crystal (Electro Dynamics Crystal Corp., 2004)	$0.1 - 30 \times 10^{-3}$	1-7	230-1000	[28]
PVDF-TrFE	0.998	13	147	[29]

Table IV-5: Parameter ranges for components in the equivalent circuit of the SRO-based PZT cantilever

Parameter k_{eff} 17.5% is also deduced based on values of the resonant measurement. The effective electromechanical coupling factor reported for the thin film of intrinsic 0.06 PMN-0.94PZT (48/52), k_{eff} 52.7%, in which the thin film has the FBAR (Film Bulk Acoustic Resonator) structure consisting of a 300 nm-thick PMN-PZT, a 110-thick SRO/Pt, a 100 nm-thick Al electrodes and the size of the Al electrode is $50 \times 50\ \mu m^2$. [30] The reduced value compared to literature is explained by the residual stress in the cantilever, which limits its motion ability.

Using the d_{31} coefficient of $-53\ pmV^{-1}$ calculated from the section IV.1.2 and Young modulus of PZT of 95.2 GPa, the stress generated inside the PZT layer itself under the application of the DC electric field of 1kV/cm, with k_{eff} 17.5%, is thus estimated around 0.1 MPa corresponding to a stress of 10 MPa when 1V is applied on a 100nm thick PZT layer.

The high dielectric constants and good electromechanical coupling of the PZT cantilever enhance the sensitivity of sensors and energy saving resonators.

From those measurements, the Q factor of the resonant structure was also extracted and a value of 64 is obtained with the chosen geometry. This value is quite low in comparison to the Q factor from bulk-based devices from the literature but in the same order of magnitude than the one from similar dimension PZT based cantilever [8][31]. Reduced dimensions of the microsystems with respect to the one found in the literature explain the reduced quality factor.

[32] The initial stress relief induced bending observed on the cantilever can also explained reduced quality factor [33] that open up for necessary perspective of study to minimize this bending by controlling the initial stress state of the films.

Typical resonant characteristics of a PZT micro-cantilever: lock-in amplifier measurement

A setup has been developed to investigate all effects of measuring conditions on cantilever behavior, that are not accessible using the "blackbox" that is the impedance analyzer. This setup allows to overcome the limitation of 2 V in the accessible range of DC bias the impedance analyzer is limited to. It also allows to have access to a larger amount of parameter such as the amplitude of AC excitation signal, sensitivity and measurement range of the output signal…

The principle of this setup is very similar to the impedance measurement, but a divider circuit is used with a reference resistor R that exhibit a value as close as possible from the one of the cantilever, in our case 4,4 kΩ in order to maximize the output signal. The output voltage and phase angle between the electrodes of the cantilever as a function of frequency is obtained by a lock-in amplifier SR844. The experimental setup and mechanism of the resonant measurements in our setup are presented in Figure IV-10.

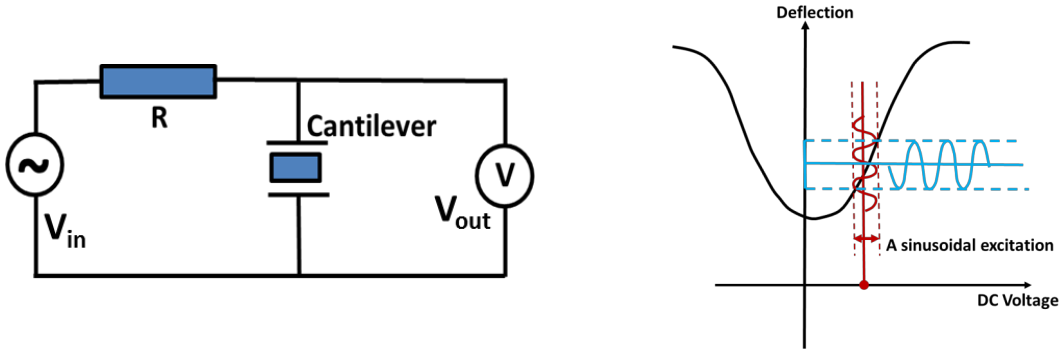

Figure IV-10: Mechanism of the resonant measurement of the PZT cantilever using the electrical excitation and experimental setup.

The resonant measurement is first made in a large range from 20 kHz to 2.5 MHz to determine the first major resonant modes of the micro-cantilever, the result is shown in Figure IV-11 with subtracted background signal. For this measurement, an exciting AC bias 200 mV_{pp} imposed on a 0V DC bias has been set to improve the observation of the resonant frequency of the cantilever around the switching point of PZT where low displacements occur. The first

three modes of the SRO-based PZT cantilever are observed at 154.44 kHz, 870.75 kHz and 2333.85 kHz. The results show that the higher is the frequency, the lower become the amplitude of the output signal and the broader become the peaks and thus the Q-factor is reduced. This unexpected phenomenon is explained by the high level of loss in short resonant cantilever (shorter than 100µm) [34].

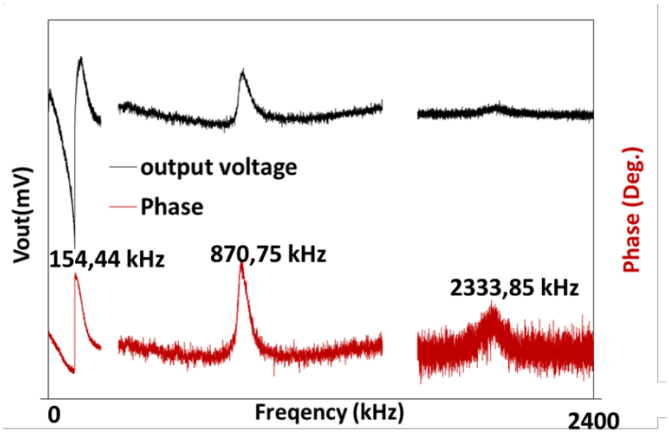

Figure IV-11: The three first modes of the SRO-based PZT cantilever at a 200 mV_{pp} imposed on a 0 V DC bias

The frequency ratio of these first three fundamental modes 1: 5.63: 15,11 shows a good agreement with the expected one (1: 6.26: 17.68) and a small difference in values of resonant frequencies in comparison to those measured with the impedance analyzer. It can be clearly seen that the first mode shows the highest output signal for both measurement methods, thus hinting that the unexpected behaviors are not linked to the measurement setup but the real device characteristic.

Figure IV-12 shows the output voltage and phase signal of the SRO-based PZT cantilever as a function of the exciting frequency sweeping around the first mode. The 80 mV_{pp} (peak-peak) AC voltage imposed on a 0V DC bias was applied. The deflection of the cantilever depending on its polarization state, the 0V DC state is obtained by pre-polarizing the PZT at -4V and then decreasing it back to 0V. The resonant and anti-resonant frequencies are observed clearly from the frequency dependence of the output voltage. Resonant peak (f_p) of 154.44 kHz from the phase is recorded which is about 1.3% in difference compared to the value measured by the impedance analyzer.

The Q-factor and effective electromechanical coupling Coefficient (k_{eff}) of the first mode extracted from the resonant measurement are 81 and 17.3%, respectively, obtained by using the the developed setup. These values are very close to that measured by using the impedance meter, which show a good agreement between the two methods. These results indicate that the developed setup can provide an effective and convenient way to study the resonant behavior of PZT cantilevers in comparison to complex impedance analysis.

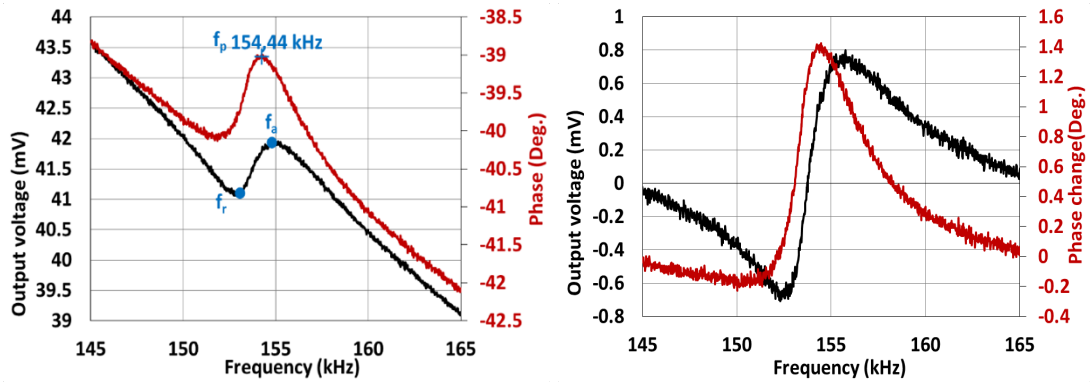

Figure IV-12: The output voltage and phase angle from the SRO-based PZT cantilever before (the left curve) and after (the right curve) subtracting the background signal. In this measurement, an 80 mV_{pp} (peak-peak) AC voltage imposed on a 0V DC bias was applied. The 0V DC bias, in this case, is the point when the DC bias applying to the PZT layer increases to -4V, and then decrease back to 0V.

In order to ease the comparison between the output impedance measurement and the output voltage, the experimental output voltages were transferred to impedance values as following expressed functions based on the setup electrical circuit in Figure IV-10:

$$\frac{V_{out}}{Ze^{i\theta}} = \frac{V_{in}}{R+Ze^{i\theta}}$$ **With $V_{out} = V_0 e^{i\xi}$ and Z is the impedance of the cantilever**

$$\rightarrow Ze^{i\theta} = \frac{RV_0 e^{i\xi}}{V_{in} - V_0 e^{i\xi}}$$ **Eq. IV-16**

$$\rightarrow Z = \frac{RV_0}{\sqrt{V_{in}^2 - 2V_{in}V_0 cos\xi + V_0^2}}$$ **Eq. IV-17**

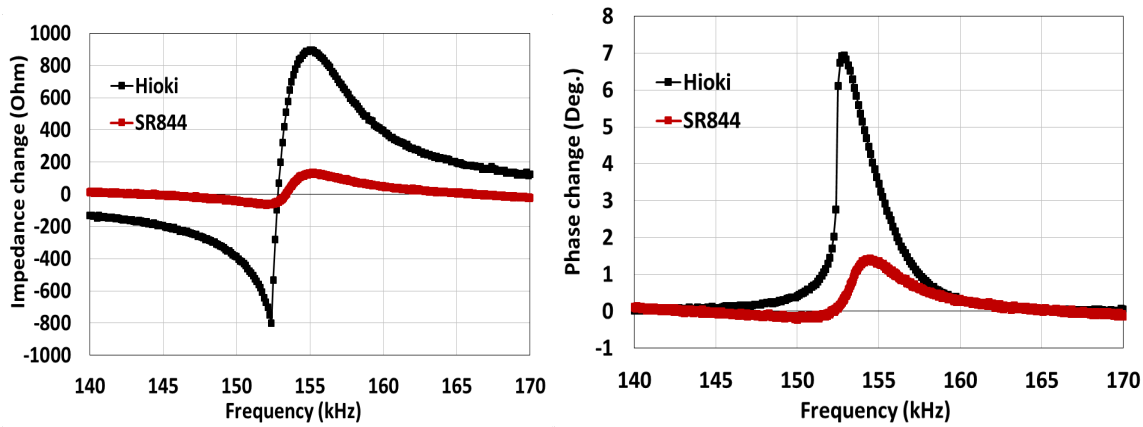

Figure IV-13: The impedance and phase angle transferred from the above experimental data after subtracting the background signal (red) compared to the results obtained by using the impedance analyzer (black)

The impedance and phase angle transferred from above experimental data using equation Eq. IV-17, compared to the results obtained by using the impedance analyzer, were shown in Figure IV-13. A change of around 1.45 mV in the output voltage obtained corresponds to a change of 190 Ω in the impedance, with the same change of 1.4° in the phase angle upon the 80 mV_{pp} bias (0 V DC bias). Similar results, a 225 Ω change of the impedance and the 1.4° change of the phase angle were reported by Dongna Shen et al. [6] in 2008 on a MEMS PZT cantilever deposited by the sol-gel method with the dimension of about 4.800 mm×0.4000 mm×0.001 mm. These results in this study indicate that the PZT micro-cantilever response well to the small driving bias, demonstrate its ability being a promising candidate for the resonator application.

IV.1.4 The resonant frequency behavior

In sensors based on resonators, the device resonant frequency is measured and exhibit the characteristics to shift with the parameter to be sensed depending on the surrounding medium and the intrinsic effects of mechanical structure. In the case of the expected resonant magneto-electric sensor, the magnetic field transfer a stress to the resonant piezoelectric cantilever which resonant frequency shift. Firstly, the effect of the measurement conditions (AC excitation, pressure) on the resonant properties of PZT cantilevers will be presented under different measurement conditions. Then simulation of the stress induced by a magnetostrictive film

using DC polarization of the PZT film will be shown. Finally, the first characterization of the ME sensor based on resonator will be shown.

IV.1.4.a The dependence of the resonant frequency on the AC excitation and the nonlinear phenomenon

PZT exhibit the advantage of the high piezoelectric coefficient in comparison with conventional piezoelectric material such as Quartz or AlN. Piezoelectricity is however more complex in this class of material and the level of stress exhibit a clear nonlinear characteristic with the electric field, corresponding to the well-known butterfly shape around the PZT coercitive field. This behavior will tend to make more difficult the analysis of the resonant properties, as was reported in a number of previous studies ([35]–[37]). This effect is observed when excitation biases of different amplitude are used to excite cantilevers, as can be seen in Figure IV-14. For better comparison, the linear background has been subtracted from the measured curves.

Two features are observed. The first is the reduction of resonant frequency along with the increase of the amplitude of the output response of the device when the AC driving bias varies from 5 -200 mV. The DC bias is fixed at -2 V in order to avoid the region near the coercitive field of the PZT where the stress dependency with bias exhibit a highly complex (see Figure IV-5 right). It is clearly visible that when the driving ac bias is higher than 150 mV, the frequency-voltage characteristic starts showing a non-linear behavior with a sudden jump in the values around the resonant frequency, as does the phase curves. This peculiar phenomenon is not observed at a lower ac bias. The increase of the amplitude of the resonator response is directly linked to the level of excitation stress, thus explaining the measured tendency. However, the change of the resonant frequency with the AC excitation is more complex to handle. It is observed in Figure IV-14 left that this change is quite small until the frequency jump is observed where it becomes much higher from 150mV excitation. Two explanations can explain this feature. First, the change in the ferroelectric domains in the materials and their movement with the electric field that exhibit an abrupt change when resonance appears, thus changing the cantilever static stress and finally its impedance (and the output signal in the measurement conditions). [38] Another possible explanation is the appearance of a non-linear effect of the resonator itself, not linked to the excited material. Some literature can be found on that topic [39], [40].

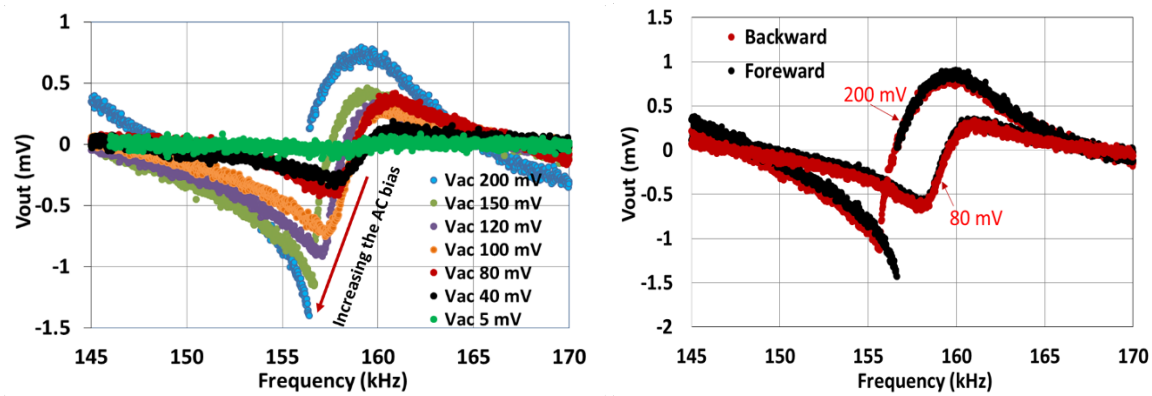

Figure IV-14: (Left) The output response of the PZT device with respect to the frequency with varying ac driving bias 5 – 200 mV when the DC bias is fixed at -2 V . (Right) the hysteretic behavior of the device when the frequency is swept forward (black) and backward (red) direction at the different AC drive 200mV$_{p-p}$ and 80 mV$_{p-p}$. In this case, the DC bias was fixed at -2V

The second phenomenon is that the resonant frequency is changed when the frequency is swept forward (black) and backward (red) direction at the high driving AC bias (200 and 80 mV$_{p-p}$, in this case), the DC bias is, again, fixed at -2V. This phenomenon is shown in Figure IV-14 right. In the forward direction, the switching of states occurs at a higher frequency and at a lower frequency in the backward direction when driving bias is 200 mV but does not appear for a low AC bias of 80 mV). This effect is again attributed to the changes in the ferroelectric domains behavior around the resonant frequency, which is thus affected by the ferroelectric state. This state appears to be different when frequency is swept from high frequency to low, with respect to low frequency to high.

IV.1.4.b The effect of the surrounding medium on the cantilever behavior

The surrounding medium is one of the dominant source of energy losses of the resonant cantilever and in particular air damping is one of the main contribution under atmospheric conditions [22]. Previous studies [41][42] show that the air damping changes not only the dynamical response such as resonant frequency, the amplitude of oscillations but also decrease the Q-factor as this value is directly linked to the energy loss. In order to be able to extract the exact Q-factor related to the device, the material it's made from and its geometry, we thus performed resonant measurements under vacuum and Figure IV-15 illustrates the corresponding experimental setup.

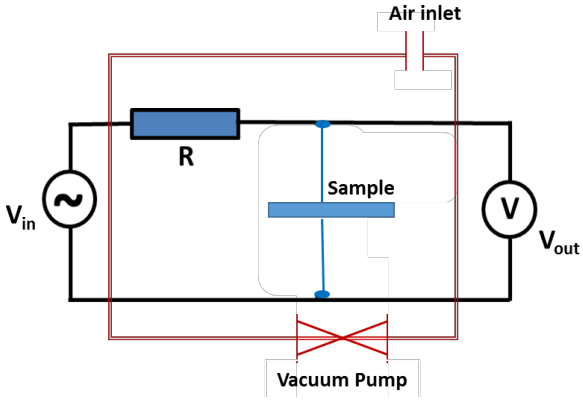

Figure IV-15: Experimental setup for characterizing the cantilever in a vacuum environment.

Figure IV-16 shows the normalized output voltage and the measured Q-factor of the first mode of the cantilever under different pressure conditions. The cantilever is placed in a vacuum chamber and is excited by subjecting an AC signal of 20mV at O V DC bias. This measurement was obtained using the lock' in based measurement setup.

The results show that the resonant peak shifts to higher frequency and the amplitude of the output voltage increases when decreasing the pressure. This phenomenon can be explained due to the reduction of the air damping around the structure leading to the reduction of energy losses. These results were also reported in previous studies [22], [41], [43]. It can also clearly be seen that, at low pressure where the cantilever movement are of higher amplitude, the Q-factor increase thus sharpening the peak. Its value increased from 70 in atmosphere to 200 under a pressure of 1 mbar. In this case, non-linear effect is not the origin of the shape of the response but only the expected response due to lower damping.

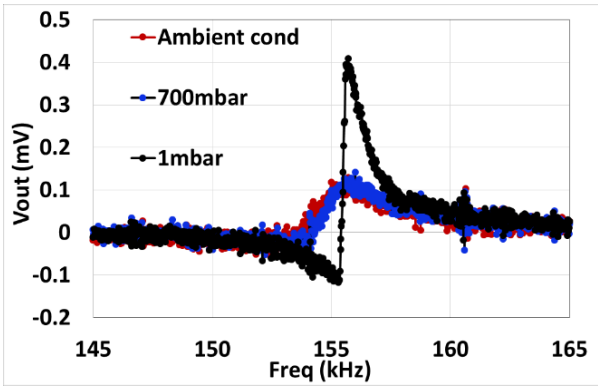

Figure IV-16: Normalized output voltage of the first mode of the cantilever under different pressure conditions. The cantilever is placed in a vacuum chamber and is excited by subjecting an AC signal of 20mV at O V DC bias

With respect to the literature on the topic, these values are comparable to those found with a 2500 µm long PZT cantilever under atmospheric and 0.1 mbar pressure (the Q-factor of 169 and 284 respectively). Beside the loss of energy due to the air damping, another loss source which is directly related to the Q-factor of the resonant mode is internal material loss [42]. The Q factor decreases when decreasing the PZT dimensions was reported by Dongna Shen et al: the reduction of the Q-factor from 400 to 233 was measured for the PZT cantilever $1.2 \times 400 \times 3293\ \mu m^3$and $1 \times 490 \times 1360\ \mu m^3$ (thickness$\times\ width \times length$).

IV.1.4.c The dependence of the resonant frequency on the DC electric field and static stress

The application of electric field on the PZT layer induces stress through the piezoelectric effect. In order to evaluate the performance of PZT cantilevers as a resonator for sensing a shift of the resonant frequency when a continuous stress is applied, oscillation characteristics were measured as a function of frequency when changing the DC bias to the PZT cantilevers.

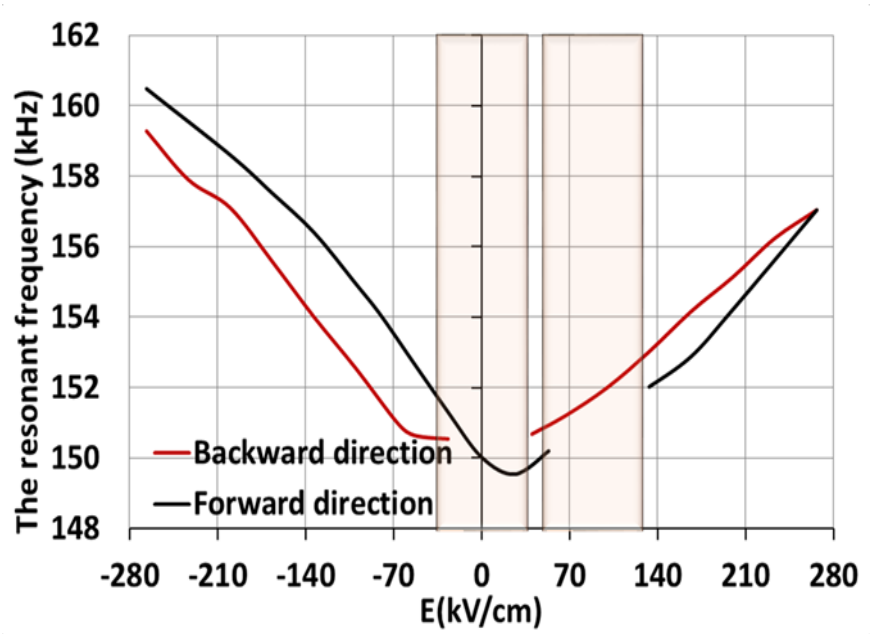

Figure IV-17: The frequency response as a function of the electric field obtained upon the application of a DC bias to the PZT thin film. The shaded regions represent the switching regions of the polarization of the PZT where the multi-polarized states show small vibration of cantilever leading to missing points.

In these measurements, the ac sine-wave of 200 mV_{pp} with a DC bias in the frequency range from 140 to 175 kHz around the first mode of vibration was applied to the top electrode while the bottom electrode was grounded. The DC bias sweeps from -4 to 4 V (corresponding to -266 to 266 kV/cm) and then back to -4 V (or -266 kV/cm). Figure IV-17 shows the resonant frequencies of the cantilever as a function of the applied DC bias that exhibits the shift of the resonant frequency following the butterfly shape. The missing points are due to multi-polarized states of PZT around the switching voltage, which lead to a small deflection of the cantilever.

A clear shift of the resonant frequency can thus be observed when the cantilever is stressed, thus allowing to expect a signal from a sensor where the stress will be generated by a magnetostrictive material. The electrical sensitivity of 32 – 51 Hz (kV/Cm) determined from the plot shows the 32 – 51 Hz frequency shift upon a 1kV/cm change of the DC electric field applied to the PZT thin film. This measurement allows to evaluate the expected sensitivity to stress of the cantilever. Figure IV-18 shows the frequency response as a function of stress which was deduced based on previous conclusions. Using literature or our measurement based characteristics of the PZT, Young modulus of 95.2 GPa and d_{31} of $-53\ pmV^{-1}$, and k_{eff} coefficient of 17.3 %, this would correspond to a shift of 360 –580 Hz for a stress of 1MPa.

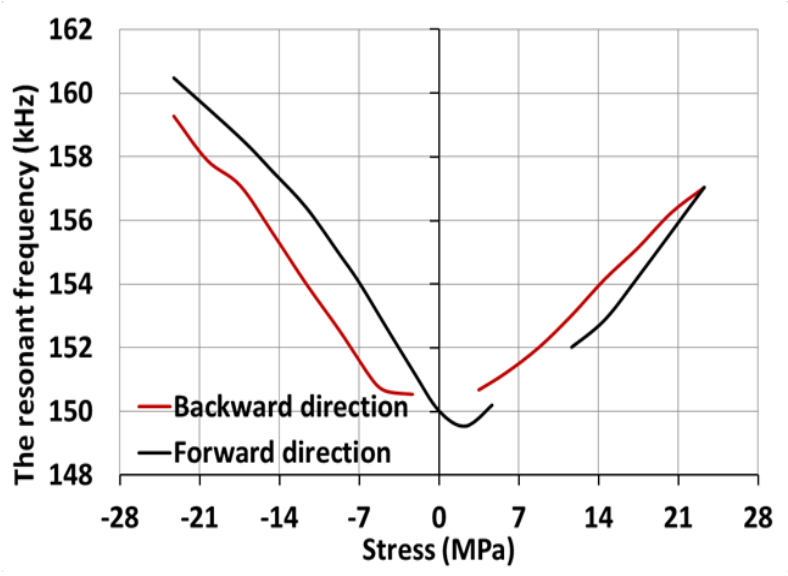

Figure IV-18: The frequency response as a function of stress applied to the PZT thin film

IV.1.5 Resonant measurements by a mechanical excitation method

In all measurements above, the cantilever was excited into vibration by an electrical voltage applied to the PZT thin film. The advantage of this technic is the excitation signal directly transferred to the cantilever. This method will exhibit a big advantage for the piezoelectric materials with a high piezo-mechanical factor. Besides that, mechanical excitation can be used, see Figure IV-19. The entire device was fixed on a PZT piezoelectric transducer. A sinusoidal signal under different frequency is applied to the transducer to make it vibrate. As consequently, the mechanical excitation causes the vibration of the cantilever. Measuring output voltage directly from PZT cantilever using a lock-in amplifier around its resonant frequency gives us the resonant signal. A DC voltage is applied to the circuit of a 4.4 kΩ resistor in series with the cantilever to control the polling direction of the PZT thin film.

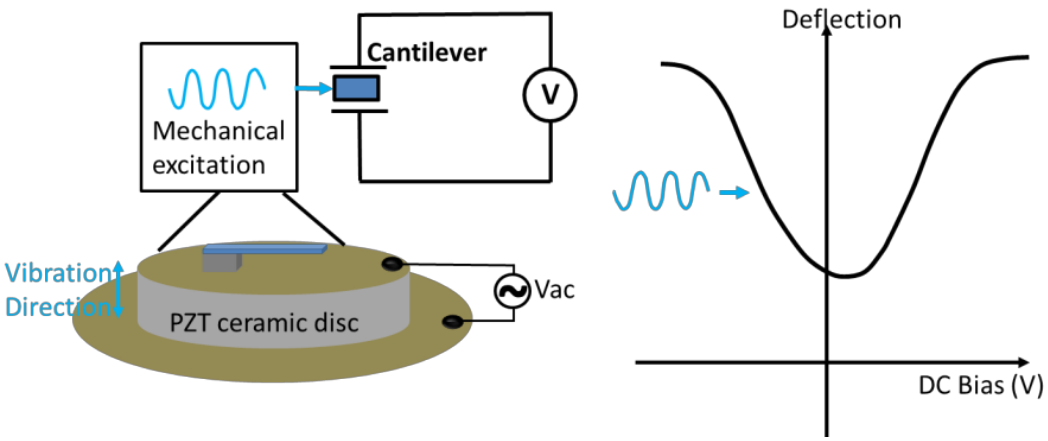

Figure IV-19: Mechanism of the resonance measurement of the PZT cantilever using the mechanical excitation and experimental setup.

The output voltage and phase angle of the SRO-based PZT cantilever as a function of the exciting frequency sweeping around the first mode is shown in Figure IV-20. For better comparison, the linear background has been subtracted from the measured curves. Due to the resonance frequency of the PZT ceramic disc about 3 kHz that is much lower than the sweeping frequency bandwidth, a high AC voltage $4V_{pp}$ was applied to the PZT ceramic transducer. The 0V DC bias (increasing the DC bias applying to the PZT layer to -4V, and then decreases back to 0V) is set. From the frequency spectrum, the shape of the resonant curves is similar to those

obtained by the electrical excitation with the difference of 0.2% of resonant peak (f_p) and a typical Q-factor of 80. However, the amplitude of the output voltage reduces significantly around 100 times in comparison to what was measured by using the electrical excitation. This result is easy to understand because the transducer works at the frequency far from its resonant frequency as mentioned above, therefore only a small excitation signal was generated. In addition, the use of mechanical excitation for measurements in the air environment will inevitably result in energy losses due to the air damping.

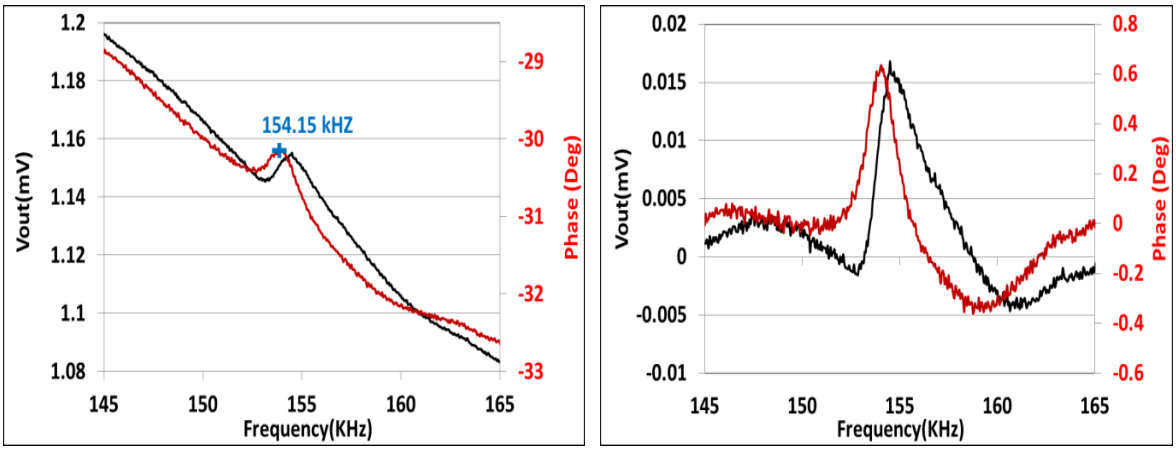

Figure IV-20: The output voltage and phase angle from the SRO-based PZT cantilever before (the left curve) and after (the right curve) subtracting the background signal. In this measurement, a $4V_{pp}$ AC voltage was applied to the PZT ceramic disk. The 0V DC bias is used to control the polling direction of the PZT thin film, which is the point when the DC bias applying to the PZT layer increases to -4V, and then decrease back to 0V.

The resonant measurements around the first mode of the cantilever were measured under different DC bias. In these measurements, the ac sine-wave of $4V_{pp}$ applied to the transducer is fixed and the DC bias sweeps from – 4 to 4 V (– 266 to 266 kV/cm) and then back to – 4 V (or – 266 kV/cm). Figure IV-21 shows the resonant frequencies of the cantilever as a function of the applied DC bias that exhibits the shift of the resonant frequency following the butterfly shape. The missing point corresponds to the switching regions of the polarization of the PZT where the multi-polarized states show small vibration of cantilever. The electrical sensitivity of 28Hz/(kV/cm) extracted from the plot is a bit lower than that determined by using the electric excitation. In this framework, this method has been given as an alternating option for investigating the resonant behavior of the cantilever

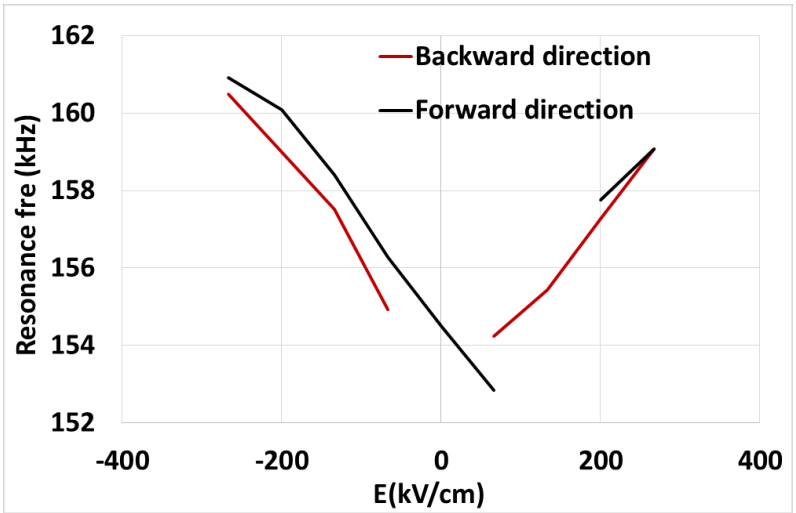

Figure IV-21: The frequency response as a function of the electric field obtained upon the application of a DC bias to the PZT thin film. The missing point corresponds to the switching regions of the polarization of the PZT where the multi-polarized states show small vibration of cantilever.

IV.2 Magnetoelectric sensors

IV.2.1 Fabrication of ME sensors

The ME sensor with cantilever configuration has the same fabrication process as the PZT cantilever which has been described in section I.1. The only difference is the replacement of the top electrode layer (Pt) by the magnetostrictive thin film TbFeCo. The TbFeCo layer works both as a magnetic layer and a top electrode thanks to its good conductivity [41].

A stack of TbFeCo(150nm)/PZT(150nm)/SRO(40nm)/CeO_2(10 nm)/YSZ (80nm)/Si (SRO-based PZT thin films) was prepared for the ME micro-sensor by using the PLD, sputtering methods (see Chapter III) and clean-room technics. The device length is 60 µm for 40 µm width. To avoid deterioration of the ferroelectric and piezoelectric properties of PZT thin-films at high temperature for our first test, the device is not annealed and the magnetostrictive susceptibility of TbFeCo is not maximized (section III.6.2).

The magnetostriction of un-patterned TbFeCo films grown on Si was measured at values of 16 x 10^{-6} and 65 x 10^{-6} at 0.07 T for the as-deposited and annealed film, respectively. Using the Young's modulus of 80 GPa from the literature, stress generated under a field of 0.07 T in

the as-deposited TbFeCo thin film due to the magnetostrictive effect is thus expected to be of the order of 1.3 MPa. Recalling the calculated result for the PZT cantilever under DC bias, a stress of 1 MPa causes a resonant frequency shift between 360 Hz and 580 Hz (depending on the up or down polarization direction – see section IV.1.4.c). It is thus expected to measure, under the external magnetic field of 0.07 T, a resonant frequency shift of the cantilever of about 460 -740 Hz for the as-deposited film.

IV.2.2 ME measurements

The principle of a ME micro-device is straightforward: It relies on the direct detection of the magnetic field-induced frequency shift. The experimental setup for ME measurement is presented in Chapter II. The device is placed between the two poles of an electromagnet to enable application of a DC magnetic field up to 0.6 Tesla. The static stress (σ_{DC}) induced from the magnetostrictive material (TbFeCo) under DC external magnetic field H_{DC} is transferred to the PZT layer. A change of H_{DC} leads to a change of σ_{DC}, to be detected on the resonant frequency of the micro-device. To do so, a AC bias excitation of 0.1 V_{pp} is superimposed on a DC voltage of 2.5 V at a frequency swept around the resonant frequency while monitoring the impedance (impedance analyzer Hioki IM3570).

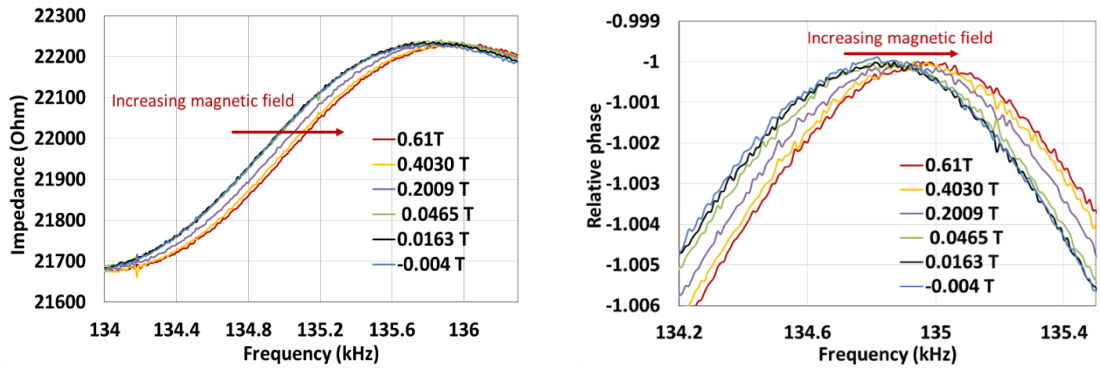

Figure IV-22 : Impedance and relative phase of the ME sensor measured as a function of frequency under different magnetic field. The field is applied in the direction perpendicular to the device surface.

Figure IV-22 shows the impedance and relative phase of the ME sensor obtained at ambient pressure as a function of the excitation frequency around the first mode under different

magnetic fields. In this measurement, the field has been applied in the direction perpendicular to the device surface (⊥s).

A shift of the resonant frequency of the ME device is evidenced, following the magnitude of the applied field. The fp frequency response as a function of the magnetic field in the direction perpendicular to the device surface (⊥s) and in the device plane either parallel (//) or perpendicular (⊥) to the sample length are shown in Figure IV-23. It can be clearly seen that the V- shape of the curves follows the typical shape of the magnetostriction curve of TbFeCo (section III.6.2). In the case of an in-plane applied magnetic field in the direction perpendicular to the sample length, the fp frequency shift under different magnetic fields is small and does not show a clear trend. This can be explained based on the relationship between the magnetization and magnetostriction effect:

$$\frac{\lambda(H)}{\lambda_{max}} = \left(\frac{M(H)}{M_{max}}\right)^2 \qquad \textbf{Eq. IV-18}$$

Due to the shape anisotropy, the easy magnetization axis tends to orientate along the length of the structure. This is in line with the measured fp frequency response in the device plane, greater for the direction parallel to the sample length than for the perpendicular one. These results also show the successful effort to enhance the in-plane magnetic anisotropy by using the magnets during the sputtering process of the magnetostrictive material TbFeCo. The curve reaches the saturated state at a lower field applied in-plane in comparison to the case when the field is perpendicular to the device surface. However, the sensitivity is not increased as in-plane and out-of-plane curves exhibit (roughly) the same slope. The magnetic anisotropy has thus not been well aligned in the in-plane direction. Another reason can come from the shape of the device: A bended shape would reduce the control over the direction of the applied magnetic field with respect to the TbFeCo layer.

The frequency shift Δ_{sh} is a signature of the magnetic field change which can be expressed as the equation $\Delta_{sh} = k.H_{DC}$. Here k is the conversion factor that characterizes the sensor sensitivity. The higher the k factor is, the higher the frequency shift with respect to the magnetic field is. For this first attempt, k = 250 Hz.T^{-1} is obtained, as a frequency shift of 17 Hz has been observed at the DC magnetic field of 0.07 T, lower than the expected ~460 Hz.

Two explanations can be found. First, assuming a state of the art magnetostrictive coefficient of 16 to 65 ppm (at 0.07 T) of the TbFeCo layer, it means that the transfer efficiency of the stress from the magnetostrictive layer to the PZT layer is around 4%. This could be due to the roughness of the SRO-based PZT thin film surface (around 6 nm) that limit the efficiency of the strain transfer. This phenomenon is expected to be reduced for the LSMO-based PZT device with better roughness (around 2 nm). Then, another possible explanation is the quality of the magnetostrictive material itself that can probably be improved (target quality, depositions conditions…) in order to maximize the magnetic field induced stress.

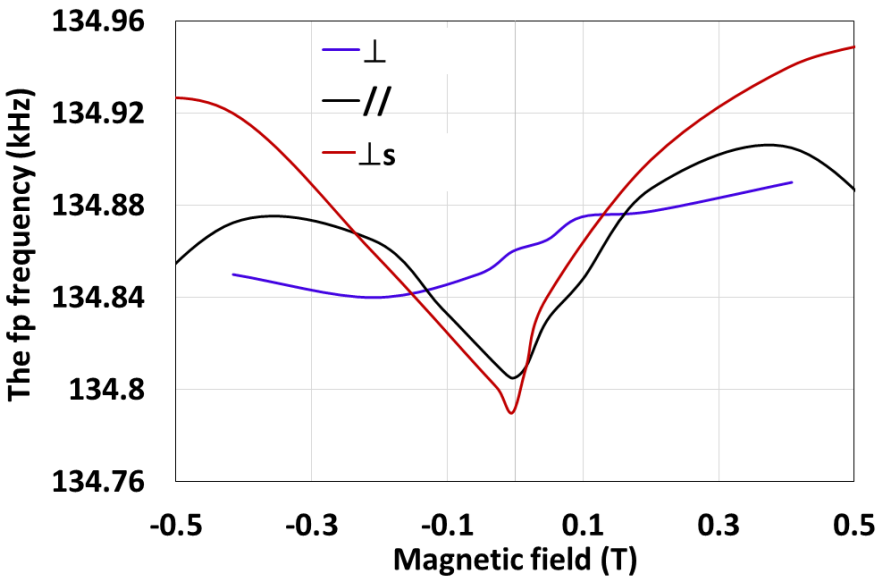

Figure IV-23: The fp frequency response as a function of the magnetic field in the direction perpendicular to the device surface (⊥*s*) and in the device plane p arallel (//) and perpendicular (⊥) to the sample length.

By characterizing the ME micro-sensor in a vacuum environment, the loss due to air damping are eliminated and the resulting sensor response can be explored. From this point, the results that will be shown were obtained under a vacuum of 0.5 mbar. An AC excitation bias of 0.01 V_{pp} superimposed with a DC voltage of 2.5 V, and an applied magnetic field in the out-of-plane direction (⊥s) were used. Figure IV-24 shows the result in terms of impedance and phase of the ME sensor. An increased response of the ME sensor is observed, with a greater resonant frequency shift in comparison with the atmospheric pressure case. This behavior is

the same as observed for the PZT cantilever alone upon decreasing the AC bias. The resonant frequency increases when increasing the external magnetic field whatever the sign of the field is (see Figure IV-26).

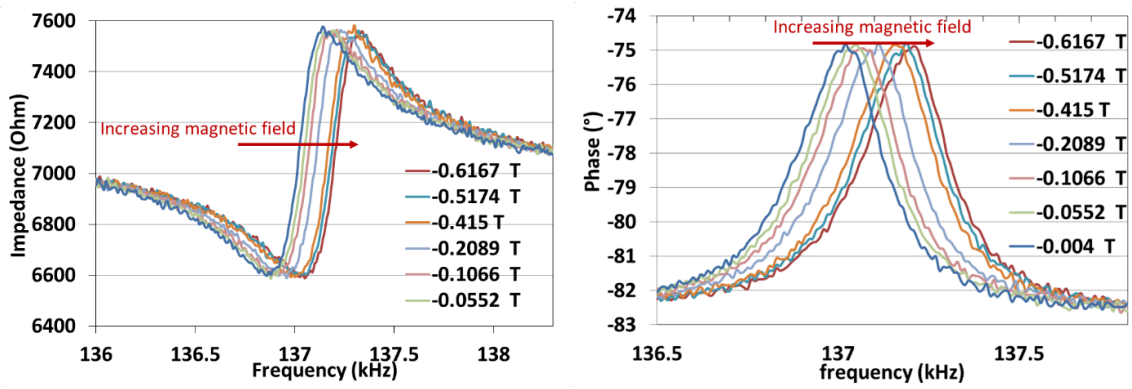

Figure IV-24: Impedance and phase of the ME sensor obtained as a function of the excitation frequency under different magnetic fields. This measurement was performed under vacuum at 0.5 mbar, with a field applied in the direction perpendicular to the device surface (⊥*s*).

Due to the reduction of air damping the resonant peaks are sharper, corresponding to an increased Q-factor of 490 calculated from the phase response (Figure IV-25).

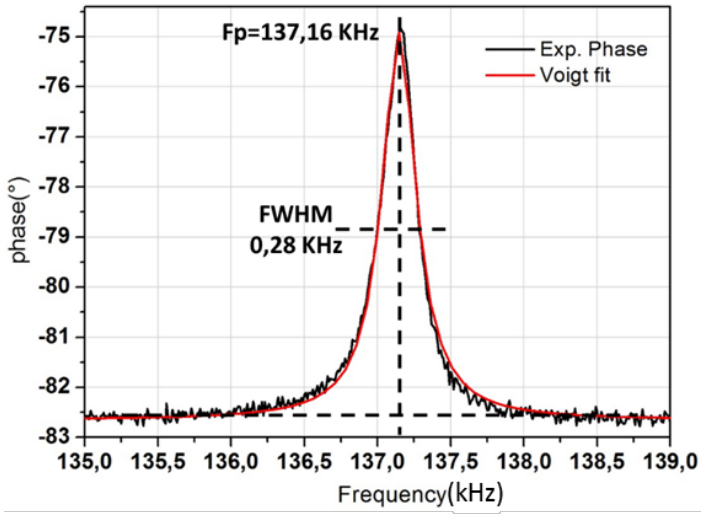

Figure IV-25 : Fitted curve (red) and phase curve (black) as a function of the excitation frequency around the first mode under an applied magnetic field of -0.415 T

Figure IV-26 shows the frequency shift of the resonant (fr) and anti-resonant (fa) peaks together with the phase peak (fp) as a function of the applied magnetic field in the direction perpendicular to the device surface ($\perp s$). The three curves exhibit a V-shape with the same relative shift of the frequency (same slope) as a function of the field.

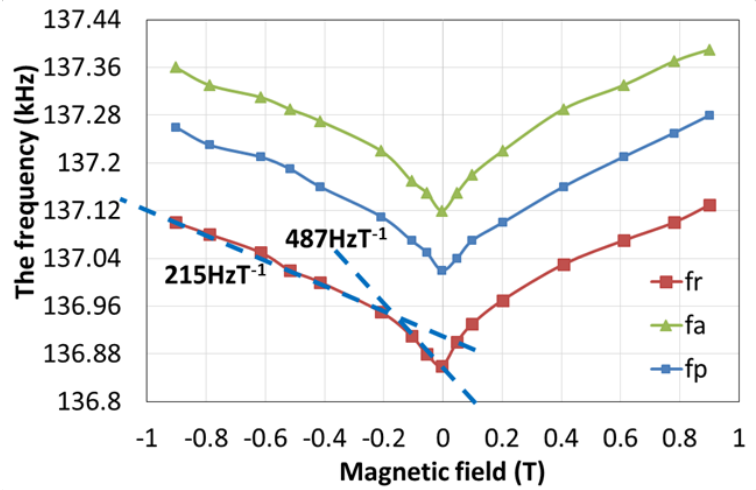

Figure IV-26: Frequency response of resonant (fr), anti-resonant (fa) and phase (fp) peaks as a function of the applied magnetic field in the direction perpendicular to the device surface ($\perp s$)

All three curves also show two clear slopes, depending on magnetic field intensity, that correspond to the magnetostrictions curve of the TbFeCo layer. From these slopes, sensitivities of 487 $Hz.T^{-1}$ at low field (< 0.2 T) and 215 $Hz.T^{-1}$ at high field (> 0.2 T) are obtained.

IV.3 Conclusions

Cantilevers based on epitaxial PZT thin films integrated on Si were fabricated and analyzed as resonant micro-sensors for sensing magnetic field based on the ME effect. For this purpose, a stack of PZT (150nm)/SRO (40nm)/CeO_2 (10 nm)/YSZ (80nm)/Si was prepared by the PLD method and clean-room processes, with either a Pt or TbFeCo layer on top of PZT acting as electrode and magnetostrictive material in the case of TbFeCo. The upward deflection of the cantilever after fabrication is due to the presence of residual stress.

The piezoelectric coefficient d_{31} was determined through static response of such PZT cantilever under a DC electric field.

The resonant response of such cantilever under the application of an AC excitation imposed on a DC bias indicates a 12% difference in the resonant frequency between the measured and calculated values. This result confirms the reliability of the calculations, which is important in predicting and optimizing the design for future studies. The dynamic studies also gave the k_{eff} coefficient of the cantilever. The cantilever exhibits a non-linear behavior for high AC excitation amplitudes. Regarding the Q-factor, it depends on the polarization direction of the PZT layer and can be increased markedly by measuring in vacuum (1 mbar) due to the reduction of air damping.

Resonant ME micro-sensors based on the magnetostrictive effect have been fabricated with a sensitivity of 250 $Hz.T^{-1}$ for out-of-plane magnetic fields above 0.2 T. The Q-factor and the sensitivity were significantly improved in vacuum (0.5 mbar), but still lower than calculated values. A high bending of the cantilever can be the reason which reduces the control on the direction of the applied magnetic field with respect to the TbFeCo layer, therefore reducing the stress transferred to the PZT layer. The residual stress generated during deposition, which causes the bending of the cantilever, can be reduced by choosing the same materials for the top and bottom electrodes on each side of the PZT layer.

Moreover, the roughness of the interface between the PZT layer and the magnetostrictive layer plays an important role; the lower the roughness the more stress can be transferred to PZT. This issue is expected to be reduced for the (001) – PZT device with smaller roughness (around 2 nm).

References

[1] J. Kusterer, A. Lüker, P. Herfurth, Y. Men, W. Ebert, P. Kirby, M. O. Keefe, and E. Kohn, "Piezo-actuated nanodiamond cantilever technology for high-speed applications," vol. 17, pp. 1429–1433, 2008.

[2] M. Dekkers, H. Boschker, M. van Zalk, M. Nguyen, H. Nazeer, E. Houwman, and G. Rijnders, "The significance of the piezoelectric coefficient d 31,eff determined from cantilever structures," *J. Micromechanics Microengineering*, vol. 23, p. 025008, 2013.

[3] C. T. Q. Nguyen, M. D. Nguyen, M. Dekkers, E. Houwman, H. N. Vu, and G. Rijnders, "Process dependence of the piezoelectric response of membrane actuators based on Pb(Zr0.45Ti0.55)O3 thin film," vol. 556, pp. 509–514, 2014.

[4] M. D. Nguyen, H. Nazeer, M. Dekkers, and D. H. A. Blank, "Optimized electrode coverage of membrane actuators based on epitaxial PZT thin films," vol. 22, p. 085013, 2013.

[5] S. Zurn, M. Hsieh, G. Smith, D. Markus, M. Zang, G. Hughes, Y. Nam, M. Arik, and D. Polla, "Fabrication and structural characterization of a resonant frequency PZT microcantilever," *Smart Mater. Struct.*, vol. 10, pp. 252–263, 2001.

[6] D. Shen, J. Park, J. Ajitsaria, S. Choe, H. C. W. Iii, and D. Kim, "The design , fabrication and evaluation of a MEMS PZT cantilever with an integrated Si proof mass for vibration energy harvesting," vol. 18, p. 055017, 2008.

[7] W. Chang, C. M. Gilmore, W.-J. Kim, J. M. Pond, S. W. Kirchoefer, S. B. Qadri, D. B. Chirsey, and J. S. Horwitz, "Influence of strain on microwave dielectric properties of (Ba,Sr)TiO3 thin films," *J. Appl. Phys.*, vol. 87, no. 6, pp. 3044–3049, 2000.

[8] M. D. Nguyen, "Characterization of epitaxial Pb(Zr,Ti)O3 thin films deposited by pulsed laser deposition on silicon cantilevers," *J. Micromech.Microeng*, vol. 20, p. 085022, 2010.

[9] J. Kiser, P. Finkel, J. Gao, C. Dolabdjian, J. Li, J. Kiser, P. Finkel, J. Gao, C. Dolabdjian, and J. Li, "Stress reconfigurable tunable magnetoelectric resonators as magnetic sensors Stress reconfigurable tunable magnetoelectric resonators as magnetic sensors," *Appl. Phys. Lett.*, vol. 102, p. 042909, 2013.

[10] K. K. Urihara, M. K. Ondo, K. S. Ato, and M. I. Shii, "Electrooptic Properties of Epitaxial Lead Zirconate Titanate Films on Silicon Substrates Electrooptic Properties of Epitaxial Lead Zirconate Titanate Films on Silicon Substrates," *Japan Soc. Appl. Phys. Electrooptic*, vol. 46, no. 10 B, pp. 6929–6932, 2007.

[11] D. Ambika, V. Kumar, H. Imai, and I. Kanno, "Sol-gel deposition and piezoelectric properties of {110}-oriented Pb(Zr0.52Ti0.48)O3 thin films," *Appl. Phys. Lett.*, vol. 96, p. 031909, 2010.

[12] Q. Li, M. Lovell, J. Mei, and W. Clark, "A Study of Displacement Distribution in a Piezoelectric Heterogeneous Bimorph," *J. Mech. Des.*, vol. 126, p. 757, 2004.

[13] J. G. Smits, W. Choi, and S. Member, "The Constituent Equations of Piezoelectric Heterogeneous Bimorphs," *IEEE Trans. Ultrason. Ferroelectr. Freq. Control*, vol. 38, no. 3, pp. 256–270, 1991.

[14] M. S. Weinberg, “Working Equations for Piezoelectric Actuators and Sensors,” *J. MICROELECTROMECHANICAL Syst.*, vol. 8, no. 4, pp. 529–533, 1999.

[15] M. D. Nguyen, M. Dekkers, E. P. Houwman, H. T. Vu, H. N. Vu, and G. Rijnders, “Pulsed laser deposition driving MEMS-based piezoelectric cantilevers,” *Mater. Lett.*, vol. 164, pp. 413–416, 2016.

[16] T. Haccart, E. Cattan, and D. Remiens, “Dielectric, ferroelectric and piezoelectric properties of sputtered PZT thin films on Si substrates: influence of film thickness and orientation,” *Semicond. Physics, Quantum Electron. Optoelectron.*, vol. 5, no. 1, pp. 78–88, 2002.

[17] H. Nazeer, “Determination of the Young ’ s modulus of pulsed laser deposited epitaxial PZT thin,” vol. 074008.

[18] C. Switzeland, “Material Characteristics.,” *Ceramaret Switzeland.*

[19] P. Paufler, B. Bergk, M. Reibold, A. Belger, N. Pätzke, and D. C. Meyer, “Why is SrTiO3 much stronger at nanometer than at centimeter scale?,” *Solid State Sci.*, vol. 8, pp. 782–792, 2006.

[20] H. Colder, B. Domengès, C. Jorel, P. Marie, M. Boisserie, S. Guillon, L. Nicu, A. Galdi, L. Méchin, H. Colder, and B. Domenge, “Structural characterisation of BaTiO3 thin films deposited on SrRuO3 / YSZ buffered silicon substrates and silicon microcantilevers Structural characterisation of BaTiO 3 thin films deposited on SrRuO 3 / YSZ buffered silicon substrates and silicon microc,” vol. 053506, no. 2014, pp. 0–9, 2015.

[21] Q. J. Huang, Y. Cheng, X. J. Liu, X. D. Xu, and S. Y. Zhang, “Study of the elastic constants in a La0.6Sr0.4MnO3 film by means of laser-generated ultrasonic wave method,” *Ultrasonics*, vol. 44, pp. 1223–1227, 2006.

[22] D. Isarakorn, A. Sambri, P. Janphuang, D. Briand, and S. Gariglio, “Epitaxial piezoelectric MEMS on silicon,” vol. 055008.

[23] Q. Wang, Q. Zhang, B. Xu, R. Liu, L. E. Cross, Q. Wang, Q. Zhang, B. Xu, R. Liu, and L. E. Cross, “Nonlinear piezoelectric behavior of ceramic bending mode actuators under strong electric fields Nonlinear piezoelectric behavior of ceramic bending mode actuators under strong electric fields,” vol. 3352, no. May 2013, 1999.

[24] W. Sriratana, R. Murayama, and L. Tanachaikhan, “Synthesis and Analysis of PZT Using Impedance Method of Reactance Estimation,” vol. 2013, no. March, pp. 62–70, 2013.

[25] Q. Chen and Q. M. Wang, “The effective electromechanical coupling coefficient of piezoelectric thin-film resonators,” *Appl. Phys. Lett.*, vol. 86, no. 2, pp. 1–4, 2005.

[26] P. Revision, “Publication and proposed revision of ansi/ieee standard 176-1987 ‘ansi/ieee standard on piezoelectricity,’” *IEEE Trans. Ultrason. Ferroelectr. Freq. Control*, vol. 43, no. 5, pp. 717–771, 1996.

[27] D. S. Stevens, H. F. Tiersten, and B. K. Sinha, “Temperature dependence of the resonant frequency of electroded contoured AT-cut quartz crystal resonators,” *J. Appl. Phys.*, vol. 54, no. 4, pp. 1704–1716, 1983.

[28] R. M. C. Mestrom, “Microelectromechanical Oscillators – a literature survey,” no. October, 2007.

[29] S. Sherrit, H. D. Wiederick, B. K. Mukherjee, and M. Sayer, “An accurate equivalent circuit for the unloaded piezoelectric vibrator in the thickness mode,” *J. Phys. D. Appl. Phys.*, vol. 30, no. 16, pp. 2354–2363, 1997.

[30] N. Yamauchi, T. Shirai, T. Yoshihara, Y. Hayasaki, T. Ueda, T. Matsushima, K. Wasa, I. Kanno, and H. Kotera, “High coupling piezoelectric thin films of Pb (Zr,Ti) O3-based ternary perovskite compounds for GHz-range film bulk acoustic resonators,” *Appl. Phys. Lett.*, vol. 94, no. 17, 2009.

[31] R. Curves, “Numerical Characterization of Piezoceramics Using Resonance Curves,” pp. 1–30, 2016.

[32] Z. Hao, A. Erbil, and F. Ayazi, “An analytical model for support loss in micromachined beam resonators with in-plane flexural vibrations,” *Sensors Actuators, A Phys.*, vol. 109, pp. 156–164, 2003.

[33] S. Ozdemir, S. Akhtar, O. Gunal, M. Khater, R. Saritas, E. Abdel-Rahman, and M. Yavuz, “Measuring the Quality Factor in MEMS Devices,” *Micromachines*, vol. 6, pp. 1935–1945, 2015.

[34] J. Yang, T. Ono, and M. Esashi, “Energy Dissipation in Submicrometer Thick Single-Crystal Silicon Cantilevers,” vol. 11, no. 6, pp. 775–783, 2002.

[35] Y. Liu, R. Ozaki, and T. Morita, “Investigation of nonlinearity in piezoelectric transducers,” *Sensors Actuators, A Phys.*, vol. 227, pp. 31–38, 2015.

[36] Y. Liu and T. Morita, “Simplified determination of nonlinear coefficients in piezoelectric transducers,” *Jpn. J. Appl. Phys.*, vol. 54, no. 10, 2015.

[37] Y. Liu and T. Morita, “Nonlinear coefficients in lead-free CuO –(K , Na) NbO3 transducers,” *Jpn. J. Appl. Phys.*, vol. 54.07HC01, 2015.

[38] J.D Andrew, “Characterizing effective d31 values for PZT from the nonlinear oscillations of clamped-clamped micro-resonators,” *J. Mech. Eng.*, vol. 59, no. 1, pp. 50–55, 2013.

[39] O. Boser, “Statistical theory of hysteresis in ferroelectric materials,” *J. Appl. Phys.*, vol. 62, no. 4, pp. 1344–1348, 1987.

[40] C. Borderon, R. Renoud, M. Ragheb, and H. W. Gundel, “Description of the low field nonlinear dielectric properties of ferroelectric and multiferroic materials,” *Appl. Phys. Lett.*, vol. 98, no. 11, p. 112903, 2011.

[41] F. R. Blom, “Dependence of the quality factor of micromachined silicon beam resonators on pressure and geometry,” *J. Vac. Sci. Technol. B Microelectron. Nanom. Struct.*, vol. 10, no. 1, p. 19, 1992.

[42] R. Sandberg, K. Mølhave, A. Boisen, and W. Svendsen, “Effect of gold coating on the Q-factor of a resonant cantilever,” *J. Micromechanics Microengineering*, vol. 15, no. 12, pp. 2249–2253, 2005.

[43] D. Isarakorn, “Epitaxial Piezoelectric MEMS on Silicon,” vol. 4939, p. 140, 2011.

[44] N. Duc, Ed., *Aspects of Magneto-electrostrictive Materials and Application*, vol. 2. Vietnam National University Press, Hanoi, 2014.

Conclusion and perspectives

Magnetoelectric (ME)-based sensors have been demonstrated as a promising alternative for the detection of weak magnetic signals with high sensitivity of few tens of nanotesla. To date, most applications focus on the use of bulk piezoelectric materials on which magnetostrictive layers are integrated by thin film deposition techniques leading to millimeter-sized devices. The downscaling of such devices into MEMS systems, bringing smaller size and lower power consumption, involves addressing different scientific issues ranging from the integration of active materials on silicon to the strong decrease in amplitude of generated signals related to the size reduction of the sensor. The objectives of this Ph.D. thesis were to develop and fabricate high quality ME materials on silicon using thin-film deposition techniques, and to examine the potential of resonant ME micro-sensors for magnetic field measurements by studying the frequency-shift dependence to applied external DC magnetic field.

For that purpose, the first part of this work focuses on the growth and characterization of the structural and ferroelectric properties of $Pb(Zr_{0.52}Ti_{0.48})O_3$ (PZT) thin films deposited *in situ* by pulsed laser deposition technique on silicon platform. To ensure the epitaxial growth of perovskite materials, the selected oxide template is formed of the bilayer: yttria-stabilized zirconia (YSZ) deposited on silicon with a CeO_2 layer to promote the crystalline quality of the perovskite. The use of different epitaxial bottom electrodes ($La_{0.66}Sr_{0.33}MnO_3$ or $SrRuO_3$) provided some flexibility by tuning the epitaxial orientation of the PZT thin films between the (110) and the (001) growth orientations. The dependence of PZT electrical properties on crystallographic orientation has been analyzed, leading to a higher dielectric constant and lower leakage current for the (110)-oriented epitaxial PZT thin films. Simultaneous studies of TbFeCo material deposited by sputtering technique indicate an improvement of the magnetostrictive response when high temperature post-deposition heat treatment under vacuum is performed. The magnetostrictive susceptibility in the low field range is higher for the annealed film compared to that of the as-deposited film.

Subsequently, PZT-based cantilevers as resonant micro-sensors have been fabricated and studied in order to advance the understanding of the static and dynamic responses of PZT

cantilevers. A complete study was performed to evaluate the PZT cantilever behavior, including exploration of the resonant response of such cantilevers under the application of an AC excitation superimposed on a DC bias. The frequency response shows the shift of the resonant frequency under a change in stress caused by the DC bias applied to the PZT layer of the micro-cantilever. Concerning the quality factor of the cantilever, it does not only depend on the polarization direction of the PZT layer and the surrounding media, but also on the initial stress state. The non-linear response with a high AC excitation has also been qualitatively studied, but the exact origin and comprehensive explanation of this phenomenon requires more detailed investigations. Finally, the integration of the magnetostrictive material TbFeCo onto PZT micro-devices to form the ME device has been completed. As the first attempt, the ME micro-sensor working as a resonator has been demonstrated as able to sense a static magnetic field. The ME micro-sensor shows a resonant frequency shift of about 250 Hz under an external magnetic field of 1T, which is still lower and smaller than predicted. Main limitation is found on the quality of the TbFeCo integrated layer with reduced magnetostriction response with respect to the full film reference samples.

Hence, some solutions should be considered to improve further the performance of the ME micro-sensor, particularly the quality factor of the cantilever but also the sensitivity (resonant frequency shift) to magnetic field. For that purpose, change in the geometry of the cantilever is to be considered, following the literature in the field and multi-physics simulations. Not only simple cantilever geometries but also more complex designs should be considered, with a particular attention to the binding points of the freestanding area to the substrate. In order to minimize the residual stress in the cantilever that is detrimental for device performance, a thorough study of the stress state of the epitaxial films of the stack should be performed. Adjustment of the film thicknesses and optimized choice of materials in the ME stack such as for the bottom electrode are expected to enhance the device sensitivity. Finally, the improvement of the growth quality of the TbFeCo on the cantilever is a key issue that is expected to push the sensitivity of these sensors to the nanotesla range.

French summary

Caractérisation et modélisation d'un micro-capteur magnétoélectrique

---

Introduction

Les capteurs magnéto-électriques (ME) représentent une alternative prometteuse pour la détection de faibles signaux magnétiques avec une sensibilité élevée. À ce jour, la plupart des développements au niveau international se sont principalement concentrées sur l'utilisation de substrats piézoélectriques massifs sur lesquels des couches minces magnétostrictives sont déposées, conduisant au mieux à des dispositifs de taille millimétrique. L'intégration de tels dispositifs dans les systèmes électromécaniques de dimensions micrométriques (MEMS), permettant ainsi d'atteindre des dimensions réduites et une consommation d'énergie plus faible, implique de trouver des solutions à plusieurs problématiques scientifiques allant des aspects relatifs à l'intégration des matériaux actifs sur silicium jusqu'à la maitrise de la réduction de l'amplitude des signaux inhérente à la réduction de la taille du capteur.

Ce travail de thèse a été centré sur l'intégration de films minces piézoélectriques de haute qualité cristalline sur substrat de silicium. Pour sonder le potentiel de tels films minces pour les dispositifs magnéto-électriques, les propriétés électromécaniques du composé $PbZrTiO_3$ intégré par épitaxie sur silicium ont été réalisés et mis en forme sous forme de microcantilevers. La capacité du levier à être utilisé comme résonateur a ensuite été étudiée. Pour ce faire, des premières caractérisations d'oscillateurs ont permis d'extraire les fréquences de résonance et les facteurs de qualité associés. Enfin, le décalage de fréquence de résonance avec contrainte induite par le biais d'une tension continue appliquée au matériau piézoélectrique a été étudiée. Finalement l'ajout d'une couche magnétostrictive de TbFeCo sur les cantilevers de PZT a permis la détection de champ magnétiques par effet ME. Le décalage de fréquence de résonance induit par l'application d'un champ magnétique externe a ainsi pu être caractérisé.

Chapitre 1 – Micro-capteurs basés sur l'effet magnétoélectrique

Le premier chapitre du manuscrit présente, sur la base de la littérature, un état de l'art des différents types de capteurs de champ magnétique. Ce comparatif permet de se focaliser sur les systèmes magnéto-électriques et leurs performances pour ce type de détection. Afin de maximiser la sensibilité finale du capteur, une première analyse a consisté à identifier les matériaux les mieux adaptés quant à leurs propriétés et la capacité de les intégrer sous la forme de films minces dans le dispositif visé. Le choix s'est porté sur l'utilisation du composé $Pb(Zr_xTi_{1-x})O_3$ (ou PZT), de structure perovskite ABO_3, comme matériau piézoélectrique qui dans sa composition morphotropique (x=0,52) présente un facteur de couplage électromécanique particulièrement élevé avec un coefficient d_{33} de l'ordre de 500 pm/V. De manière analogue, les matériaux magnétostrictifs ont été analysés en lien avec leurs caractéristiques en mettant l'accent sur les grandeurs principales que sont les coefficients magnetostrictifs ainsi que la susceptibilité magnétostrictive. Le choix s'est ici porté sur l'alliage de TbFeCo qui présente des caractéristiques adaptées et présente l'avantage d'être maitrisé en films minces. L'analyse des différentes réalisations de capteurs magnéto-électriques de la littérature mettant en œuvre ces matériaux est ensuite présentée. La dernière partie du chapitre est consacrée à l'état de l'art de l'intégration de ces différents matériaux sur silicium. Le silicium est un substrat nécessaire dans cette approche car il permet l'utilisation de procédés conventionnels en salle blanche pour la réalisation du microsystème final. Cependant la qualité cristalline des films actifs, piézoélectriques et ferromagnétiques, est directement liée aux couches d'adaptation qui favorisent la croissance cristalline sur silicium. Les différentes approches de la littérature permettant l'intégration de ces matériaux sur silicium sont finalement présentées.

Chapitre 2 – Techniques expérimentales

Ce chapitre est dédié à la description de toutes les techniques expérimentales utilisées dans ce travail. La première partie décrit les techniques de croissance qui permettent d'intégrer des couches minces épitaxiées de PZT sur du silicium par ablation laser pulsé (PLD) ainsi que des

couches minces magnétostrives à base d'alliage TbFeCo en utilisant la méthode de pulvérisation cathodique. Les outils de caractérisation qui permettent d'extraire les propriétés structurales des films minces déposés par diffraction des rayons X (DRX) et la morphologie de surface par microscopie à force atomique (AFM) sont décrits dans le contexte de ce travail. La description générale de ces techniques est donnée ainsi que la manière de choisir les paramètres clés pour extraire les caractéristiques typiques des différents types de films étudiés. La dernière section se concentre sur la manière d'extraire les propriétés fonctionnelles du matériau au moyen de caractérisations électriques ou mécaniques, respectivement pour les matériaux piézoélectriques et magnétostrictifs développés dans ce travail. Une description détaillée de chaque technique est donnée ainsi que leurs avantages et leurs inconvénients, basée sur la littérature.

Chapitre 3 – Films minces piézoélectriques et magnétostrictifs sur silicium

Dans un micro-capteur magnéto-électrique, le film mince piézoélectrique joue un rôle crucial pour convertir la contrainte mécanique induite par la couche magnétostrictive lorsque soumise à un champ magnétique en un signal électrique. Par conséquent, l'intégration de couches minces épitaxiales de PZT de haute qualité sur substrats de silicium a été considérée comme la première étape principale pour la fabrication de micro-dispositifs. Ce chapitre présente les couches minces de PZT obtenues sur Si (001) dans ce travail, avec l'utilisation de couches d'adaptation d'oxydes. Ces films ont été déposés par ablation laser pulsé (PLD). A cet effet, la zircone stabilisée à l'yttrium (YSZ) associé avec des films de CeO_2 et $SrTiO_3$ a été utilisée pour promouvoir la croissance du film actif piézoélectrique. L'utilisation de différentes électrodes inferieures épitaxiées, $SrRuO_3$ ou $La_{0.66}Sr_{0.33}MnO_3$, a permis de maitriser l'orientation de croissance des films de PZT entre les directions (110) et (001). La dépendance des propriétés électriques de PZT sur l'orientation cristallographique a été analysée, conduisant à une constante diélectrique plus élevée et à un courant de fuite plus faible pour les couches minces épitaxiales de PZT orientées (110) en accord avec les différents résultats de la littérature. Enfin, les conditions de croissance et les propriétés magnétiques des films de

TbFeCo sont présentées en dernière partie de ce chapitre. L'étude des propriétés magnétiques du matériau TbFeCo déposé par pulvérisation cathodique a conduit à une amélioration de la réponse magnétostrictive lorsqu'un traitement thermique post-dépôt sous 250°C est réalisé sous vide.

Chapitre 4 – Micro-capteurs résonant basé sur des micro-leviers de PZT

Ce dernier chapitre est centré sur la finalité de ce travail avec le développement d'un micro capteur magnétoélectrique. Pour cela il a été nécessaire modifier la stratégie de mesure du capteur par rapport aux capteurs millimétriques de la littérature exploitant l'effet magnéto-électrique en raison de la réduction en taille du système qui réduit drastiquement le signal à mesurer. L'approche a consisté à exploiter la résonance mécanique des cantilevers réalisés qui lorsque soumis à un champ magnétique est modifiée par modification de la rigidité du système. Pour ce faire, une structure de type poutre suspendue, bien connue dans le domaine des microsystèmes a été choisie. La configuration où le dispositif a été libéré du substrat de Si permet au PZT de s'affranchir de sa limite élastique et ainsi générer une plus grande contrainte et ainsi une puissance plus élevée. La figure 1 illustre le schéma de principe et présente une vue obtenue par microscopie électronique à balayage d'un dispositif.

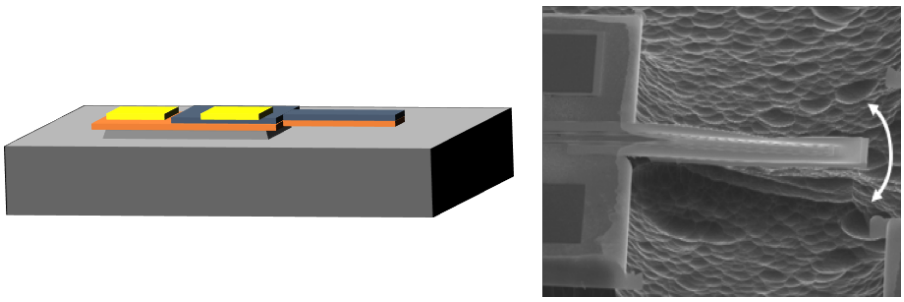

Fig. 1 : Schéma de principe d'un micro-levier résonant et image par microscopie électronique à balayage d'un tel capteur

Les caractéristiques des poutres de PZT ont été étudiées sous plusieurs aspects. Tout d'abord, la déformation de la poutre lors de l'application d'un champs électrique continu a permis d'extraire le coefficient piézo-électrique du PZT. Ensuite, les propriétés de résonance de ces structures ont été obtenues par plusieurs approches dont les résultats ont été comparés aux modèles analytiques de la littérature. Les conditions de mesure permettant d'obtenir une réponse optimale ont ainsi pu être évaluées permettant notamment de maximiser le facteur de qualité qui dépend non seulement de la direction de polarisation de la couche de PZT et des milieux environnants, mais aussi de l'état de contrainte initial du système. La réponse non-linéaire obtenue avec une forte excitation alternative a également été étudiée qualitativement, mais l'origine exacte et l'explication complète de ce phénomène nécessite des investigations complémentaires. Pour évaluer la capacité à exploiter cette structure comme capteur magnétoélectrique, le changement de la fréquence de résonance de tels poutres suspendues a été quantifié en appliquant une contrainte continue par l'intermédiaire d'un champ électrique sur le film piézo-électrique.

Dans une seconde partie, les premiers résultats de réalisation et de mesure d'un résonateur pour détecter un signal magnétique à base de couches minces multi-ferroïques PZT / TbFeCo sont présentés. Un décalage de fréquence de résonance du dispositif est mesuré en reflétant l'amplitude du champ magnétique externe. Quantitativement une sensibilité de l'ordre de 1 Hz/mT est mesurée, valeur inférieure à celle attendues (Figure 2). La limitation principale identifiée est liée à la qualité de la couche intégrée TbFeCo avec une réponse magnétostrictive réduite par rapport aux échantillons de référence.

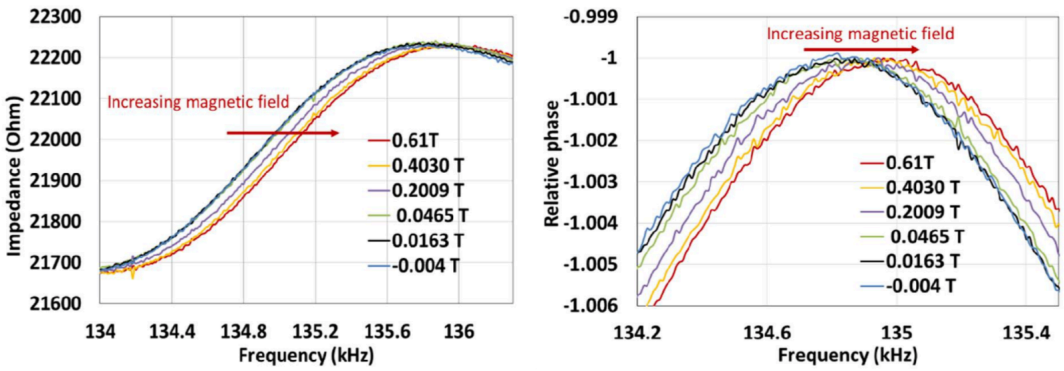

Fig. 2 : Réponse fréquentielle de l'impédance et de la phase du micro-levier en fonction du champs magnétique externe imposé

Conclusion

Cette thèse a consisté à développer et fabriquer des matériaux ME de haute qualité sur silicium en utilisant des techniques de dépôt de couches minces et à étudier le potentiel des micro-capteurs ME résonants pour les mesures de champ magnétique.

Avec cet objectif, la première partie de ce travail s'est concentré sur la croissance et la caractérisation des propriétés structurales et ferroélectriques de couches minces de PZT déposées de manière in situ par PLD sur substrat de silicium. Pour assurer la croissance épitaxiale des matériaux pérovskites, une couche tampon base de zircone stabilisée à l'yttrium (YSZ) associé à un film de CeO_2 est utilisé pour favoriser la qualité cristalline de la pérovskite fonctionnelle. Le choix du matériau de l'électrode inférieure, $SrRuO_3$ ou $La_{0.66}Sr_{0.33}MnO_3$, permet de contrôler l'orientation cristalline de la couche de PZT. Les propriétés résultantes de ces films, y compris les caractérisations structurales, ferroélectriques et diélectriques, sont déterminées en fonction de l'orientation cristalline des films minces de PZT. La susceptibilité magnétostrictive dans la plage de champ faible est plus élevée pour le film recuit comparé à celui du film tel que déposé.

Par la suite, des leviers suspendus à base de PZT ont été exploité comme micro-capteurs résonants afin de faire progresser la compréhension de leurs réponses statiques et dynamiques. En particulier, la réponse résonnante de tels leviers sous l'application d'une excitation alternative superposée à une polarisation continue a montré que le changement de contrainte de la couche PZT modifie sa fréquence de résonance. L'intégration du matériau magnétostrictif TbFeCo sur les micro-dispositifs PZT pour former le dispositif ME a été achevée. Comme première tentative, le micro-capteur ME fonctionnant comme un résonateur a été démontré comme capable de détecter un champ magnétique statique.

Pour améliorer le capteur, certaines solutions devraient être envisagées en particulier l'amélioration du facteur de qualité du cantilever mais aussi la sensibilité (décalage de fréquence de résonance) au champ magnétique. Pour ce faire, il faut considérer de modifier de la géométrie du levier suspendu, en suivant la littérature en y associant de la simulations multi-physiques. Des conceptions plus complexes doivent être envisagées, en accordant une attention particulière aux points de liaison de la zone libre au substrat. Afin de minimiser la contrainte

résiduelle dans le levier, qui est préjudiciable à la performance du dispositif, une étude approfondie de l'état de contrainte des films doit être effectuée. L'ajustement des épaisseurs de films et le choix optimisé des matériaux dans le l'empilement ME, par exemple l'électrode inférieure, devraient améliorer la sensibilité du dispositif. Enfin, l'amélioration de la qualité de croissance du TbFeCo sur le cantilever est un problème clé qui devrait pousser la sensibilité de ces capteurs bien au-dessous de la plage du nanotesla.

université PARIS-SACLAY
ÉCOLE DOCTORALE
Physique et ingénierie : électrons, photons, sciences du vivant (EOBE)

Titre : Caractérisation et modélisation d'un micro-capteur magnétoélectrique

Mots clés : Effet magnétoélectrique, matériaux piézoélectriques, matériaux magnétostrictifs, capteurs magnétiques

Résumé : Les capteurs magnéto-électriques (ME) sont une alternative prometteuse pour mesurer de faibles signaux magnétiques. Précédemment le choix était généralement de déposer des couches minces magnétostrictives sur un matériau piézoélectrique massif conduisant à des systèmes macroscopiques de taille millimétrique. L'intégration de ces systèmes dans des MEMS (micro-electro-mechanical systems) requiert à la fois de résoudre les problèmes d'intégration de matériaux actifs sur silicium et de mesurer des petits signaux étant donné l'importante réduction de la réponse du système lorsqu'il est miniaturisé.

Dans cette optique, le premier objectif de ce travail de thèse a été d'intégrer un matériau piézoélectrique sur un substrat de silicium tout en conservant une excellente qualité cristalline. Le $Pb(Zr_{0,52}Ti_{0,48})O_3$ (PZT) a été retenu pour ses excellentes propriétés piézoélectriques. L'intégration de la couche mince se fait sur silicium qui est le substrat de prédilection pour la fabrication de microsystèmes avec les procédés microélectroniques standards. La qualité cristalline des matériaux actifs est directement corrélée aux couches d'adaptation utilisées pour obtenir une bonne qualité cristalline sur silicium. Pour cela l'intégration d'une tricouche composée de zircone stabilisée à l'yttrium (YSZ), d'oxyde de cérium (CeO_2) et de $SrTiO_3$ permet ensuite la croissance des pérovskites d'intérêt pour le dispositif. Le choix de l'électrode conductrice inférieure ($SrRuO_3$ ou $La_{0.66}Sr_{033}MnO_3$ dans le cas présent) permet de contrôler l'orientation de la maille de PZT.

Une première étude des propriétés piézoélectriques de la couche mince de PZT sous la forme d'une poutre libre pour son intégration dans un système magnétoélectrique a été réalisée. La mesure de la déformation de la poutre induite par application d'une tension électrique permet d'extraire un coefficient d_{31} de $-53pmV^{-1}$, valeur inférieure au matériau massif mais à l'état de l'art dans ce type de dispositif. Dans une seconde étape, l'utilisation de la poutre comme résonateur a été étudiée. L'étude dynamique du système a permis d'obtenir la fréquence de résonance et le facteur de qualité. Le déplacement de la fréquence caractéristique du système en fonction d'une contrainte induite par une tension DC a été investigué. Enfin l'ajout d'une couche de matériau magnétostrictif (TbFeCo) sur la poutre a finalisé la structure du capteur. Le capteur ainsi obtenu a été caractérisé et une sensibilité de l'ordre de la dizaine de micro Tesla est obtenue.

Université Paris-Saclay
Espace Technologique / Immeuble Discovery
Route de l'Orme aux Merisiers RD 128 / 91190 Saint-Aubin, France

université PARIS-SACLAY
ÉCOLE DOCTORALE
Physique et ingénierie : électrons, photons, sciences du vivant (EOBE)

Title: Characterization and modeling of magnetoelectric micro-sensors

Keywords: Magneto-electric effect, piezoelectric materials, magnetostrictive materials, magnetic sensors

Abstract: Magneto-electric (ME) sensors have been demonstrated as a promising alternative for the detection of weak magnetic signals with high sensitivity. To date, most applications focused on the use of bulk piezoelectric materials on which magnetostrictive thin films are deposited leading to millimeter-sized devices. The integration of such devices into micro-electro-mechanical systems (MEMS), bringing smaller size and lower power consumption, involves addressing several scientific issues ranging from the integration of active materials on silicon to the strong reduction in amplitude of generated signals related to the size reduction of the sensor.

In this context, the first goal of this thesis work was to integrate high crystalline quality piezoelectric thin films on silicon. $Pb(Zr_xTi_{1-x})O_3$ (PZT) with a morphotropic composition (x=0.52) having high electromechanical coupling factor was chosen. Silicon is a necessary template as it allows for the use of conventional clean room processes for the realization of the microsystem. The crystalline quality of the active films is directly linked to the buffer layers that promote the crystalline growth on silicon. For this purpose, Yttria-stabilized Zirconia (YSZ) was used in combination with CeO_2 and $SrTiO_3$ to allow further growth of epitaxial perovskites. The choice of the bottom electrode material ($SrRuO_3$ or $La_{0.66}Sr_{0.33}MnO_3$ in this work) further tunes the crystalline orientation of the PZT layer.

To probe the potential of such PZT thin films for ME devices, the first step was to characterize the electromechanical properties of this material in a free-standing cantilever structure. Under an applied electric field, the measured displacement of the epitaxial PZT-based cantilevers is characterized by a coefficient $d_{31} = -53pmV^{-1}$, a reduced value with respect to the bulk material but that can be enhanced by further optimizing the film growth. The second step consists in ascertaining the ability of the cantilever to be used as resonator. For that purpose, first characterizations of oscillators have been performed to extract the resonant frequencies and the associated quality factors. Then, the resonant frequency shift with DC bias-induced stress was measured. Finally, a magnetostrictive layer of TbFeCo was added on the PZT cantilevers to sense magnetic field based on the ME effect. The resulting resonant frequency shift with external applied magnetic field was characterized with a typical sensitivity of 10's of µT.

Université Paris-Saclay
Espace Technologique / Immeuble Discovery
Route de l'Orme aux Merisiers RD 128 / 91190 Saint-Aubin, France